JAERI-M
82-167

A STUDY ON DIRECT INTEGRATION METHOD FOR SOLVING NEUTRON TRANSPORT EQUATION IN THREE-DIMENSIONAL GEOMETRY

November 1982

Nobuo SASAMOTO

日本原子力研究所
Japan Atomic Energy Research Institute

JAERI-Mレポートは，日本原子力研究所が不定期に公刊している研究報告書です。

入手の問合わせは，日本原子力研究所技術情報部情報資料課（〒319-11茨城県那珂郡東海村）あて，お申しこしください。なお，このほかに財団法人原子力弘済会資料センター（〒319-11茨城県那珂郡東海村日本原子力研究所内）で複写による実費頒布をおこなっております。

JAERI-M reports are issued irregularly.

Inquiries about availability of the reports should be addressed to Information Section, Division of Technical Information, Japan Atomic Energy Research Institute, Tokai-mura, Naka-gun, Ibaraki-ken 319-11, Japan.

編集兼発行　日本原子力研究所
印　　　刷　いばらき印刷㈱

JAERI - M 82-167

A Study on Direct Integration Method for Solving Neutron Transport Equation in Three-Dimensional Geometry

Nobuo SASAMOTO

Division of Reactor Engineering, Tokai Research Establishment, JAERI

(Received October 27, 1982)

A numerical method is presented for calculating neutron transport problems in three-dimensional (x,y,z) geometry based on a method of direct integration of the transport equation. Several new techniques are introduced to the method to make it well adopted to practical neutron transport calculations in three-dimensional geometry. Use of a functional approximation for spatial distribution of source term with a combination of linear and exponential functions enables one to perform calculations with coarse spatial mesh intervals keeping the results accurate. In addition, a technique for evaluating the scattering source based on an estimated spectral shape in each material region allows use of coarse energy mesh intervals without reducing calculational accuracy as compared with the calculation using fine meshes. Theoretical error analysis is made on the direct integration method showing that a quadratic function approximation for the source spatial distribution in each spatial mesh interval improves the mathematical error in direct integration of the source term over the spatial variable as compared with the linear - or exponential - function approximation used in the original method.

Based on the present method, a neutron transport code in three-dimensional (x,y,z) geometry PALLAS-XYZ is developed. In addition, an auxiliary code is made for accurate reaction rate calculation using third order natural spline function. Further, a multi-group neutron cross section library is generated for neutron transport codes based on a direct integration method, including nuclear data for 27 nuclides and 4 mixtures which are important in shielding calculations.

In order to verify the validity of the present method, several PALLAS-XYZ calculations are presented and compared with shielding benchmark experiments, with Monte Carlo, and with two- and three-dimensional S_n calculations. The PALLAS-XYZ calculation without any three-dimensional leakage correction agrees well (with a maximum error of 30 %) with the PCA benchmark experiment. The PALLAS-XYZ calculation is also compared with the neutron streaming experiment through annular duct and with the three-dimensional S_n calculation, showing that both calculations somewhat underestimate the experiment on the neutron attenuation within the duct. The PALLAS-XYZ code is applied to a neutron transport calculation for a typical 1000 MWe-class PWR core. This predicts the boundary flux outside the core, with which a two-dimensional (R,θ) transport calculation is then made for its core barrel and pressure vessel.

Keywords ; Transport Theory, Neutron, Direct Integration Method, PALLAS-XYZ, Three-Dimension, (x,y,z) Geometry, Error Analysis, PALLAS Library, PCA Experiment, Shielding, Streaming, PWR, Pressure Vessel

3次元幾何形状に対する中性子輸送方程式の直接積分解法に関する研究

日本原子力研究所東海研究所原子炉工学部
笹本宣雄

（1982年10月27日受理）

3次元（x,y,z）形状に対する中性子輸送方程式の直接積分法にもとづく数値解法に関する一連の研究を行った。現実的な3次元中性子輸送計算に適用可能な解析手法を確立するために新しい計算手法を開発した。線源項の空間分布を1次関数と指数関数の組合せで関数近似する手法の導入により，計算精度を損わずに粗空間メッシュの計算が可能となった。さらに1次元輸送計算により求めた領域毎のスペクトルの勾配を利用して3次元散乱線源計算を行う手法を開発した。本手法の導入により粗いエネルギーメッシュを用いた計算で，細かいエネルギーメッシュ計算並の精度が保証されることを示した。次に，直接積分法の理論誤差解析を行い線源空間分布の近似関数として2次関数を用いると，従来の1次関数，指数関数近似よりも理論誤差が改善されることを明らかにした。

本解法にもとづき3次元（x,y,z）形状中性子輸送計算コードPALLAS－XYZを開発し，あわせて補助コードとして，3次の自然スプライン関数を用いた高精度の反応率計算コードを作成した。また，直接積分法輸送コード専用の多群中性子断面積ライブラリを遮蔽計算上重要な27核種，4混合物質について作成した。

本解析手法の妥当性を検証するため，PALLAS－XYZを用いて2種類の遮蔽ベンチマーク実験の解析を行い，実験値，モンテカルロ計算値，1,2次元Sn計算値と比較した。PCA実験に対するPALLAS－XYZの計算値は体系からの漏洩中性子束の補正なしに最大誤差30％の精度で実験値を再現した。さらにPALLAS－XYZによる円環ダクトストリーミング問題の計算値を実験値及び3次元Sn計算値と比較し，両計算値とも実験値にくらべてダクト軸に沿った反応率の減衰率が幾分大きいことがわかった。次にPALLAS－XYZを1000 MWe級PWR炉心に対する中性子輸送計算に適用した。PALLAS－XYZの計算値から作成した炉心外側における境界中性子束を用いて，炉心バレル，圧力容器での2次元（R,θ）中性子輸送計算を実施した。

CONTENTS

目　次

LIST OF FIGURES

LIST OF TABLES

Introduction

Radiation shielding calculation is most distinctly characterized by the radiation transport through a complicated three-dimensional geometry with highly anisotropic scattering. Improvement of the accuracy of shielding design calculation inevitably requires modeling of practical shielding configurations in complicated geometry. The Monte Carlo method has been considered to be the only applicable technique for detailed three-dimensional analyses of such complicated shields and many Monte Carlo codes have been developed for application to practical shielding problems, such as a 05R[1)] by Irving et al., a MORSE[2)] by Straker et al., and so on. Among others, the MORSE code is the most widely and successfully applied to a variety of radiation transport problems because in order to save computer running time, it uses energy group-averaged cross sections common to the discrete ordinates transport calculations, instead of point cross section data in 05R calculation. In spite of high expectations for application of the Monte Carlo method to practical shielding calculations, it still involves several difficulties such as a limited number of detector points where radiation fluxes or responses are determined in addition to large statistical uncertainties because of limited computer running time. This method particularly reveals its weakest point in deep penetration problems. To solve these difficulties, a lot of studies have been made leading to development of a variety of importance sampling methods summarized in Ref.3, a Monte Carlo coupling technique[4)] and so on. In spite of all the vigorous research efforts, the fundamental problems of the Monte Carlo method remain unresolved. Therefore, rapid progress in computer performance and further efforts in reduction of both computer running time and the standard deviation are largely sought after in future.

Carlson[5)] developed a discrete-ordinate method in 1955 which became known as the S_n method and which has been successfully applied to a variety of transport problems. In 1965, Engle developed ANISN[6)] which made the S_n method more suitable for shielding calculations. For more direct and pratical application to shielding design calculations, the two-dimensional S_n codes DOT[7)] by Mynatt et al., and TWOTRAN[8)] by Lathrop were developed.

The discrete ordinates transport codes have been used with a great deal of success in obtaining detailed radiation distributions in a variety of two-dimensional geometries with far less computer running time than that used in Monte Carlo calculations[9)]. The two-dimensional (r,z) geometry code is particularly regarded as the most useful for reactor shielding design calculations, because three-dimensional configuration of a typical reactor core can be well approximated with (r,z) geometry. The (r,z) code, however, cannot be directly applied to problems having axially asymmetric geometries, such as radiation streaming problems through multi-legged ducts which are often encountered in shielding design calculations. To overcome this difficulty, we usually adopt either of the following two alternatives: one is a discrete ordinates coupling calculation using coordinate transformed boundary fluxes, and the other is a calculation with DOT-DOMINO-MORSE code system[10)]. Both methods, however, require a complex coordinate transformation procedure which adds further numerical errors to shielding calculations.

Given the background just described above, in recent years, there has been a growing interest in establishing a reliable method for three-dimensional shielding calculations based on the transport equation. Much effort has been paid, therefore, to extending two-dimensional discrete ordinates S_n codes to three-dimensional (x,y,z) geometry, yielding the design of the ENSEMBLE code[11)]. This code has been developed for radiation shielding calculation on the basis of the fundamental framework used in the THREETRAN[12]. For this purpose, special features[8,13,14] have been implemented in ENSEMBLE which make it well adopted to shielding problems. Its application to practical shielding calculations is, however, limited to rather small geometrical configurations because it requires much computer running time. Further, ENSEMBLE involves some fundamental drawbacks of the S_n method still unresolved, such as the appearance of negative fluxes and a problem of unconverged or diverged solution in the iteration-convergence procedure.

In investigating the causes of such problems inherent in the S_n method, Takeuchi developed in 1971 an alternative transport calculation method[15] based on his previous studies[16-19]. Takeuchi's method solved the steady-state integral transport equation numerically by integrating the equation directly along the neutron flight path in the direction of neutron motion, with a discrete ordinates representations of the angular variable in general geometry. Several neutron shielding calculation codes have been developed based on this method: the PALLAS-PL, SP[20] and the PALLAS-2DCY[21] codes, respectively, in one-dimensional plane and spherical geometries and in two-dimensional (r,z) geometry. The accuracy of neutron transport calculations with these codes was verified by comparing them with experiments made in comparatively simple geometrical configuration, such as the energy spectra in graphite, polyethylene, and water[22-25] and those in a laminated iron-water shield[26]. The first application of this method to a practical reactor shielding calculation was made[27] using the PALLAS-2DCY code for investigating the cause of radiation leakage from the reactor shield of the nuclear ship MUTSU in 1974.

Subsequently, several improvements such as introduction of asymmetric angular quadrature set and source distribution approximation by exponential function were made in the method for ensuring its calculational accuracy for neutron streaming through ducts[28)] and for deep penetration problems[29)]. In addition, the present method has been developed to provide capability of gamma-ray transport calculations in shield and also in the atmosphere from a point isotropic sources[30)].

As is well known, one of the weakest points in the discrete ordinates method is the occurrence of the ray effect in calculating spatial distributions of radiation flux due to localized sources. To mitigate the ray effect, improvement has been made on the calculational scheme to evaluate separately the unscattered and scattered fluxes and, in addition, to calculate the unscattered flux analytically on the basis of the point kernel integration for a variety of source configurations such as point, line, disk and cylindrical sources[31)]. This technique has been implemented on a two-dimensional (r,z) PALLAS-2DCY-FC transport code[32)].

The characteristic features of the direct integration method presented here are[33)]:

1. The present method does not apply Legendre expansion approximation for treatment of anisotropic scattering. Instead, it uses the differential scattering cross section itself (e.g., the Klein-Nishina formula for Compton scattering) for accurate treatment of its anisotropy.
2. It calculates analytically the flux term at a spatial mesh point $\bar{r}_i$ of interest from a previous mesh point $\bar{r}_{i-1}$ by integrating over the spatial variable in the direction of radiation movement at each discrete ordinate direction, which requires no supplementary equation such as the diamond difference equation in the S_n method.
3. It calculates the source term also by integrating in the same manner as described in item 2 on the basis of the approximation that the

source spatial distribution can be represented by a linear or an exponential function which always results in positive and physically meaningful angular flux.

4. It does not apply the inner iteration method for obtaining the group flux except for the thermal neutron group, but it does apply energy mesh calculation at each energy mesh, requiring fine energy meshes to avoid the inner iteration.

The method of Takeuchi just described can be classified as a method of characteristics[34,35] whre solutions are obtained by analytical integration along the practical trajectories (or "characteristics"), using the integral form of the transport equation. Various methods of characteristics have been investigated by many authors. Among them, the following are considered to be representative: the method of Takeuchi[33], that of Wagner, et al.[36], that of Askew[37], the streaming ray method of Filippone[38], and the linear characteristic method of Larsen, et al[39]. The methods of solution differentiate thermselves in the way that characteristics used for calculation are selected and the way the source term is approximated[34].

Wagner's method was developed for solving general (x,y,z)-geometry transport problems having a uniform spatial mesh, in which only certain directions determined by the spatial mesh are chosen as characteristic rays. It assumes a constant source along the characteristics. This method, designed for a cuboidal cell, was expanded by Askew, aiming at to apply it to a variety of one-and two-dimensional geometries. Thus, Askew's method is also based on the assumption of a constant source. On the other hand, Filippone's general-purpose (x,y)-geometry streaming-ray method was established by combining the method of characteristics and the finite difference approximation utilized in the S_n method. This method assumes a uniform spatial mesh and specially prepared quadrature sets and it also assumes a constant source along the characteristics. Next, the general-purpose (x,y)-geometry linear characteristic method is also a hybrid method similar to Filippone's method, assuming a linear source approximation throughout the cell and linearly varying boundary conditions along the incoming cell boundaries.

Whereas flexibility is severely limited in Wagner's method, given that the uniformly chosen spatial mesh determines the allowed directions for the characteristics, Takeuchi's method allows the choice of any direction of characteristic rays, independently of the spatial mesh and without any restriction on the spatial mesh assignement. Askew and Filippone relax somewhat these restrictions, although they do prefer a regular placement of the characteristics (e.g., equal spacing, a fixed number per cell etc.) In addition, it is seen that only Takeuchi's method is readily extendable to other geometries and mesh assignments. Application of other methods, except for Filippone's, is limited to specific geometries, such as the (x,y,z) geometry for Wagner's, the one- and two-dimensional curvilinear geometries for Askew's and the (x,y) geometry for Larsen's.

As for the source representation along the characteristics, whereas Wagner, Askew and Filippone employ a constant source approximation which is pointed out to limit the calculational accuracy34), and Larsen has improved accuracy by using a linear source approximation, a linear or an exponential representation chosen by option is implemented in Takeuchi's method. Furthermore, any polynomial functions of higher order are applicable in Takeuchi's method because sources at all mesh points are determined before making transport calculations.

As is well known, the cell balance equation is the basic ingredient in the methods of characteristics. The methods of Wagner and of Askew, as well as the linear characteristic method, satisfy a balance equation.

The methods of Takeuchi and of Filippone, however, are not guaranteed to satisfy it.

In addition, Takeuchi's method includes some distinguished features which are not employed in other methods. This method deals with within-group scattering calculation without using an inner iteration method, and it calculates the scattering source instead of using truncated Legendre expansion approximation.

Although it is pointed out that the methods of characteristics incorporated in existing general purpose calculation codes still involve many difficulties, the PALLAS codes have been developed on the basis of Takeuchi's method for a variety of one-, two- and three-dimensional geometries and successfully applied to many practical shielding problems.

The aim of the present study is to establish a method for solving the neutron transport equation in three-dimensional (x,y,z) geometry on the basis of the direct integration method whose fundamental theory is presented in Ref.33. For this purpose, several calculational techniques are newly introduced40) to the original method33).

The original method fundamentally requres fine energy meshes due to the absence of application of the conventional iteration-convergence technique for solving the equation, which is impractical for three-dimensional transport calculations because of too much computer running time. To overcome this difficulty, we introduce a spectral shape technique for estimation of the neutron energy spectrum between coarse energy mesh intervals in each subdivided material region40). With this technique, regionwise weight functions to be used in three-dimensional scattering calculation are determined based on the corresponding spectra from one-dimensional PALLAS calculation with negligibly small computer running time as compared with that needed for the three-dimensional calculation.

Introduction of this technique enables us to carry out three-dimensional transport calculation in the coarser energy meshes with a negligibly small increase of computer running time.

Another factor in order to reduce computer running time is to adopt coarse spatial meshes keeping the calculational accuracy. For this purpose, we introduce an exponential method[29)] in the three-dimensional calculation method. In the direct integration method, the flux is calculated by integrating analytically the integral transport equation over spatial mesh interval between any adjacent meshes assuming that source spatial distribution between the two meashes can be approximated by an appropriate function. While the source distribution was originally approximated by a linear function[22)], we presented a new method[29)] to approximate the source distribution by an exponential function. This method was found to result in a remarkable improvement in calculations with small numerical errors, irrespective of the spatial mesh size. In other words, use of the method enables one to carry out three-dimensional transport calculations with rather coarse spatial mesh intervals keeping their results accurate.

As presented in the fundamental theory of the direct integration method[33)], the original method calculates analytically the flux term at a spatial mesh point $\bar{r}_i$ of interest from a previous spatial point $\bar{r}_{i-1}$ by integrating over the spatial variable, while it calculates the source term by integrating in the same manner as in the flux term calculation assuming that the spatial distribution can be represented by a linear or an exponential function. This spatial approximation of the source term produces some errors in the evaluation of the flux, hence, the theoretical analysis of the error in the direct integration method was made for the first time on the basis of the theory by Lee and Vaidyanathan[41)]. As a result, it was found that the original method has a leading error of

Δ^3 (Δ denotes a spatial mesh interval), which is the same order as that of the diamond difference scheme in the S_n method[41]. In order to improve the mathematical error, we introduce in the present study a scheme with the source distribution approximated by a quadratic function, which is found to have a leading error of the order of Δ^4.

The direct integration method requries the estimation of both flux and source at a spatial point $\bar{r}_{i-1}$ to calculate the flux at a spatial mesh point $\bar{r}_i$ of interest, since the spatial point $\bar{r}_{i-1}$ does not always coincide with the specified spatial mesh points. For this purpose, a linear interpolation scheme is applied in the original method taking account of a one-dimensional spatial variation of the flux and source, while in three-dimensional (x,y,z) geometry, both flux and source at a spatial point $\bar{r}_{i-1}$ should be estimated using an interpolation scheme taking into account their two-dimensional spatial variations. To this end, we introduce a new technique[40] for estimating more accurately both flux and source at a spatial point $\bar{r}_{i-1}$ using Lagrange's interpolation formula by bilinear or biquadratic form[42]. A three-dimensional neutron transport code PALLAS-XYZ has been developed based on the present method.

Validity of the present method was verified by calculating two neutron transport problems (Problem I and Problem II) taken from the experiments. In addition to the comparison of the PALLAS-XYZ calculations with the experiments, they were compared with those using two-dimensional discrete ordinates S_n codes and Monte Carlo Code (Problem I) and with that using the three-dimensional S_n code ENSEMBLE (Problem II). Furthre, the present method was applied to a practical shielding problem (Problem III) for a typical 1000 MWe class PWR power reactor.

Problem I is a pool critical assembly (PCA) benchmark experiments[43,44] made at the Oak Ridge National Laboratory (ORNL). In order to assess state-of-the-art neutronics methodology relative to reactor surveillance, the United States Nuclear Regulatory Commission (USNRC) conducted a computational Blind Test based on measurements performed in the PCA-PV Wall Benchmark Facility44).

Since the whole experimental configuration can be accurately expressed by three-dimensional (x,y,z) geometry, the PCA experiment is appropriate for verification of three-dimensional neutron transport calculation. Therefore, we participated in the computational Blind Test by the three-dimensional calculation with PALLAS-XYZ. As pointed out in Ref.44, most Blind Test calculations from various countries are made with discrete ordinates two-dimensional (x,y) coordinate transport codes with some corrections for the axial leakage. The exceptions are the calculations with one-dimensional ANISN6), the two-dimensional PALLAS-2DCY-FC32) in (r,z) geometry, the three-dimensional PALLAS-XYZ code in (x,y,z) geometry, and the Monte Carlo code MORSE2) and McBend45). The calculated neutron fluence greater than 0.1 and 1.0 MeV, and various reaction rates of fast neutron threshold reactions are compared with experiments. The PALLAS-XYZ calculation free from geometrical modeling error was valued to be fair because of its good agreement with the experiment without any corrections for three-dimensional leakage44).

Problem II is the only shielding problem available for our comparison that has been solved with the three-dimensional S_n code ENSEMBLE11). This problem is an experiment28) of neutron streaming through an annular duct, performed at a swimming pool-type reactor JRR-4 at the Japan Atomic Energy Research Institute (JAERI). Since the duct axis intersects at right angles the horizontal axis of the reactor core, and the height of the duct axis does not coincide with that of the core midplane, spatial distribution of neutron flux within the duct shows apparent asymmetry with respect to the duct axis. Therefore, three-dimensional transport analysis is the only method available that can solve this problem.

Problem III is to estimate detailed neutron fluence in reactor pressure vessel of a typical 1000 MWe class PWR power reactor with a vessel inner radius of 220.28 cm^46). Because of the rectangular geometry of a reactor core and the cylindrical shell configuration of a core barrel and pressure vessel in most power reactors, it is most accurately represented by a combination of (x,y,z) and (r,θ), or preferably (r,θ,z) geometries. Considering the fact that the neutron fluecne at a corner of the core standing closest to the pressure vessel provides the largest contribution to the neutron field at the pressure vessel, three-dimensional transport calculation is essential for the analysis of integral dosimetry measurements and for predicting irradiation damage exposure parameters in the pressure vessel and in the support structures of operating LWR nuclear power plants. Therefore, for determining the neutron field in the pressure vessel of a PWR reactor accurately, neutron transport calculations were made within a core to provide the boundary flux distributions around the core, with which neutron transport calculation was performed for a core barrel and a pressure vessel using a two-dimensional (r,θ) transport code PALLAS-2DRT.

This thesis consists of two main parts; Part-I describes the direct integration method for solving integral transport equation in three-dimensional (x,y,z) geometry and Part-II deals with shielding benchmark calculations and analyses of real problems with the three-dimensional PALLAS-XYZ code. Part-I is further divided into four chapters.
In Chapter 1, an outline is given of the fundamental theory of the direct integration method for solving the steady-state integral transport equation in general geometry developed by Takeuchi^33). In Chapter 2, a solution

is derived by the author$^{40)}$ of integral transport equation in three-dimensional (x,y,z) geometry based on the fundamental theory in general geometry. Chapter 2 also presents some numerical methods newly introduced in the original method for establishing a practical three-dimensional transport calculation method: exponential method, spectral shape estimation technique and two-dimensional spatial variation estimation of flux and source terms. In addition, a theoretical error analysis is made to the direct integration method. Chapter 3 is devoted to describing the three-dimensional PALLAS-XYZ code on the basis of the numerical method presented in Chapter 2. In addition, a description is given an auxiliary code for reaction rate calculation using the natural spline function. Chapter 4 describes a multi-group neutron cross section library applicable not only to PALLAS-XYZ, but to other PALLAS codes in various geometries.

Part II consists of three chapters, dealing with PALLAS-XYZ calculations of real problems. Chapter 5 gives the PALLAS-XYZ calculations for the international PCA Blind Test conducted by the USNRC$^{44)}$. They are compared not only with the experiment but also with other calculations using the discrete ordinates S_n codes and Monte Carlo codes. In Chapter 6, calculational results with the PALLAS-XYZ are presented for a neutron duct streaming problem$^{40)}$. They are compared with both the experiments and the calculation with the three-dimensional S_n code ENSEMBLE$^{11)}$. Chapter 7 presents the neutron fluence calculation in the pressure vessel of a typical 1000 MWe class PWR power plant, using PALLAS-XYZ combined with PALLAS-2DRT. In Chapter 8, summary and conclusions throughout the present study are presented.

Part-I Direct Integration Method for Solving Neutron Transport Equation in Three-Dimensional (x,y,z) Geometry

1. Fundamental Theory of the Direct Integration Method[33)]

The steady-state integral transport equation is written with the following conventional notation[33)]

$$\Phi(\bar{r},\bar{\Omega},E) = \Phi(\bar{r}-R\bar{\Omega},\bar{\Omega},E)\exp[-\int_0^R \Sigma_t(\bar{r}-R'\bar{\Omega},E)dR']$$

$$+\int_0^R dR'\ s(\bar{r}-R'\bar{\Omega},\bar{\Omega},E)\exp[-\int_0^{R'} \Sigma_t(\bar{r}-R''\bar{\Omega},\bar{\Omega},E)dR'']$$

$$+\int_0^R dR'\int_0^{4\pi} d\bar{\Omega}'\int_E^{\infty} dE'\ \Sigma_s(\bar{r}-R'\bar{\Omega}\ ;\ E'\rightarrow E,\ \bar{\Omega}'\rightarrow\bar{\Omega})$$

$$\times\ \Phi(\bar{r}-R'\bar{\Omega},\bar{\Omega}',E')\exp[-\int_0^{R'} \Sigma_t(\bar{r}-R''\bar{\Omega},\bar{\Omega},E)dR''] \quad , \qquad (1.1)$$

for the spatial vector system illustrated in Fig.1.1.

Rewriting Eq.(1.1), we obtain the following equation in accordance with the notation of the energy flux instead of the neutron flux:

$$I(\bar{r},\bar{\Omega},E) = G(\bar{r},\bar{\Omega},E) + \Lambda I(\bar{r},\bar{\Omega},E) \quad , \qquad (1.2)$$

where the integral operator

$$\Lambda I(\bar{r},\bar{\Omega},E) = \int_0^R dR'\ \sum_i \{\int d\bar{\Omega}'\int dE'\ \Sigma_s{}^i(\bar{r}''\ ;\ E'\rightarrow E,\ \bar{\Omega}'\rightarrow\bar{\Omega})$$

$$\times\ I(\bar{r}'',\bar{\Omega}',E')(E/E')\exp[-\tau(\bar{r},\bar{r}'',E)]\} \quad , \qquad (1.3)$$

where suffix i denotes nuclides included in the material region of interest, while

$$G(\bar{r},\bar{\Omega},E) = I(\bar{r}',\bar{\Omega},E)\exp[-\tau(\bar{r},\bar{r}',E)] + \int_0^R dR' \; S(\bar{r}'',\bar{\Omega},E)\exp[-\tau(\bar{r},\bar{r}'',E)] \quad , \tag{1.4}$$

with

$$\bar{r}'' = \bar{r} - \bar{R}'\bar{\Omega} \quad , \qquad I = E\Phi \quad , \qquad S = Es \quad ,$$

and

$$\tau(\bar{r},\bar{r}',E) = \int_0^{|\bar{r}-\bar{r}'|} \Sigma_t(\bar{r} - R'\bar{\Omega},\bar{\Omega},E)\,dR' \quad , \tag{1.5}$$

where $\tau(\bar{r},\bar{r}',E)$ is the optical length between positions $\bar{r}'$ and $\bar{r}$ for radiation energy E. Let $Q(\bar{r},\bar{\Omega},E)$ be the scattering source term as

$$Q(\bar{r},\bar{\Omega},E) = \sum_i \int d\Omega' \int dE' \cdot \Sigma_s{}^i(\bar{r}\,;E'\rightarrow E,\ \bar{\Omega}'\rightarrow\bar{\Omega})\,I(\bar{r},\bar{\Omega}',E')(E/E') \quad . \tag{1.6}$$

Henceforth, the suffix i for nuclide is neglected for simplicity.
The source term $Q(\bar{r},\bar{\Omega},E)$ consists of an elastic scattering source $Q_{e\ell}(\bar{r},\bar{\Omega},E)$ and an inelastic scattering one $Q_{in}(\bar{r},\bar{\Omega},E)$. The differential scattering cross section is represented by$^{33)}$

$$\Sigma_s(\bar{r}\,;E'\rightarrow E,\ \bar{\Omega}'\rightarrow\bar{\Omega})$$

$$= \Sigma_{e\ell}(\bar{r},E')f_{e\ell}(E',\mu)\delta(\cos\theta - \alpha) \cdot \frac{(A+1)^2}{2AE'} \quad , \tag{1.7}$$

for elastic scattering; and

$$= \Sigma_{in}(\bar{r},E') \cdot \frac{f_{in}(E'\rightarrow E)}{4\pi} \quad , \tag{1.8}$$

for inelastic scattering.

In the above expressions, $\Sigma_{e\ell}(\bar{r},E)$ and $\Sigma_{in}(\bar{r},E)$ are, respectively, the total elastic and inelastic scattering cross sections. Value A is the mass number of the nuclide, and μ and α are the cosines of the polar angle of elastic scattering in the center-of-mass system and in the laboratory system, respectively. The azimuthal angle of elastic scattering is denoted by ψ. Furthermore, $f_{e\ell}(E,\mu)$ is the elastic scattering distribution function and $f_{in}(E'\rightarrow E)$ is the inelastic scattering energy distribution.

Let $Q_{e\ell}(\bar{r},\bar{\Omega},E')$ be the elastic scattering source term; then Eq.(1.6) is rewritten as[33)]

$$Q_{e\ell}(\bar{r},\bar{\Omega},E') = \int d\mu \int d\psi \cdot \Sigma_{e\ell}(\bar{r},E') f_{e\ell}(E',\mu) I(\bar{r},\bar{\Omega}',E') \quad . \qquad (1.9)$$

Numerical integration over μ is made using a Gaussian quadrature[15)] in which $f_{e\ell}(E',\mu)$ is approximated by discrete values $f^m(E')$ at its quadrature mesh points $\mu_m(m=1,2,\text{-----},M)$, while for the integration over the azimuthal angle ψ, the following numerical integration is applied. Prior to carrying out the integration, the neutron moving direction $\bar{\Omega}$ is represented by discrete ordinates meshes $\bar{\Omega}_{pq} \equiv \bar{\Omega}(\omega_p,\phi_{pq})$, in which ω_p and ϕ_{pq} are, respectively, the cosine of p'th value of the polar angle and the q'th azimuthal angle at the p'th polar angular level of the neutron flight direction as depicted in Fig.1.2. The azimuthal scattering angle ψ is also approximated by discrete meshes ψ_n in accordance with the neutron directional cosines ω_n before scattering. The weights w_n for $\psi_n(n=1,2,\text{-----},P)$ in the numerical integration over ψ can be determined from Eq.(1.10) corresponding to Fig.1.3 as[33)]

$$w_n = \left| \cos^{-1}\frac{\omega_n^+ - \omega_p\alpha_m}{[(1-\omega_p^2)(1-\alpha_m^2)]^{1/2}} - \cos^{-1}\frac{\omega_n^- - \omega_p\alpha_m}{[(1-\omega_p^2)(1-\alpha_m^2)]^{1/2}} \right| , \qquad (1.10)$$

where ω_n^+ and ω_n^- are, respectively, the values of the upper and lower bounds of the ω_n range. Further, α_m in the above expression is calculated from[33)]

$$\alpha_m = \frac{A\mu_m + 1}{(A^2 + 2A\mu_m + 1)^{1/2}} \quad . \tag{1.11}$$

Consequently, Eq.(1.9) is numerically evaluated for $\bar{\Omega} = \bar{\Omega}_{pq}$ as[33)]

$$Q_{e\ell}(\bar{r},\bar{\Omega}_{pq},E) = \sum_m \sum_n W_m w_n \Sigma_{e\ell}(\bar{r},E_{(m)}) f^m(E_{(m)}) I(\bar{r},\bar{\Omega}'_n,E_{(m)}) \quad , \tag{1.12}$$

where W_m are the weights for μ_m in Gaussian quadrature.

In order to determine the neutron flight direction before collision $\bar{\Omega}'_n(\omega_n,\phi')$, the azimuthal angle ϕ' is defined by the formula of scattering corresponding to Fig.1.3 as[33)]

$$\phi'_\pm = \phi_{pq} \pm \cos^{-1}\left\{ \frac{\alpha_m - \omega_p \omega_n}{[(1-\omega_p^2)(1-\omega_n^2)]^{1/2}} \right\} \quad . \tag{1.13}$$

As illustrated in Fig.1.3, the discrete ordinates directions $\bar{\Omega}'_n$ may be represented as $\bar{\Omega}_{ns}(\omega_n,\phi'_-)$ and $\bar{\Omega}_{nt}(\omega_n,\phi'_+)$, respectively. Another unknown variable $E_{(m)}$ in Eq.(1.12) is determined for $E = E_j$ and $\mu = \mu_m$ using the relationship between energy and scattering angle in the center-of-mass system:

$$E_{(m)} = E(\mu_m) = \frac{(A+1)^2}{A^2 + 2A\mu_m + 1} \cdot E_j \quad . \tag{1.14}$$

For practical calculation, however, when $E_{(m)}$ is within g'th energy interval, $E_{(m)}$ is replaced by E_g. Therefore, $\Sigma_{e\ell}(E_g)$, $f^m(E_g)$ and $I(E_g)$ are taken for the values of $\Sigma_{e\ell}(E)$, $f^m(E)$ and $I(E)$ at the energy $E_{(m)}$. Then Eq.(1.9) is rewritten as

$$Q_{e\ell} = \sum_{g=1}^{j} \sum_{m\epsilon g} F_{e\ell}(\bar{r},E_{(m)},E_j) \sum_n w_n[I(\bar{r},\bar{\Omega}_{ns},E_g) + I(\bar{r},\bar{\Omega}_{nt},E_g)] \quad , \qquad (1.15)$$

where both $\bar{\Omega}_{ns}$ and $\bar{\Omega}_{nt}$ are the moving directions of neutrons before scattering as depicted in Fig.1.3,

$$F_{e\ell}(\bar{r},E_{(m)},E_j) = \Sigma_{e\ell}(\bar{r},E_g)W_m f^m(E_g) \quad . \qquad (1.16)$$

The assumption adopted in the above calculation indicates that the neutron energy flux $I(E_g)$ is constant (i.e., the 1/E spectrum) within the g'th energy mesh interval.

On the other hand, the inelastic scattering source is calculated by Eq.(1.17) on the assumption of isotropic scattering in the laboratory system

$$Q_{in}(\bar{r},\bar{\Omega}_{pq},E_j) = \sum_{g=1}^{j} F_{in}(\bar{r},E_g,E_j)I_0(\bar{r},E_g) \quad , \qquad (1.17)$$

where

$$F_{in}(\bar{r},E_g,E_j) = \Sigma_{in}(\bar{r},E_g) \cdot \frac{f_{in}(E_g,E_j)}{4\pi} \left(\frac{E_j}{E_g}\right) \Delta E_g \quad , \qquad (1.18)$$

with the energy mesh width ΔE_g, and

$$I_0(\bar{r},E_g) = \int_{4\pi} d\bar{\Omega}\ I(\bar{r},\bar{\Omega},E_g) \quad . \qquad (1.19)$$

Thus, the neutron scattering source Q is numerically evaluated from the expression

$$Q(\bar{r},\bar{\Omega}_{pq},E_j) = \sum_{g=1}^{j} \left\{ \sum_{m\epsilon g} F_{e\ell}(\bar{r},E_{(m)},E_g) \cdot \sum_n w_n[I(\bar{r},\bar{\Omega}_{ns},E_g) + I(\bar{r},\bar{\Omega}_{nt},E_g)] + F_{in}(\bar{r},E_g,E_j)I_0(\bar{r},E_g) \right\} \quad . \qquad (1.20)$$

For the internal-mesh scattering calculation, conventional iteration-convergence technique is not utilized. Instead, the concept of removal theory is adopted on the assumption that those neutrons elastically scattered within a small scattering angle can be considered as being unscattered. As a result, the internal-mesh source due to elastic scattering is calculated from[33)]

$$Q_{e\ell,j} = 2\pi\,\Sigma_{e\ell}(\bar{r},E_j)W_1 f^1(E_j)\,I(\bar{r},\bar{\Omega}_{pq},E_j) \quad , \tag{1.21}$$

and the one due to inelastic scattering is obtained by Eq.(1.17) with $g = j$. Thus, we obtain the scattering source except for the internal-mesh source by Eq.(1.22) as,

$$Q' = \sum_{g=1}^{j-1}\left\{\sum_{m\in g} F_{e\ell}(\bar{r},E_{(m)},E_g)\sum_n w_n\left[I(\bar{r},\bar{\Omega}_{ns},E_g) + I(\bar{r},\bar{\Omega}_{nt},E_g)\right] + F_{in}(\bar{r},E_g,E_j)\,I_0(\bar{r},E_g)\right\} \quad . \tag{1.22}$$

Subtracting $Q_{e\ell,j}$ from both sides of the basic steady-state Boltzmann transport equation, we obtain[33)]

$$\bar{\Omega}\,\bar{\nabla}I + \Sigma_t{}'(\bar{r},E_j)I = S + Q' \quad , \tag{1.23}$$

where

$$\Sigma_t{}'(\bar{r},E_j) = \Sigma_t(\bar{r},E_j) - 2\pi\,\Sigma_{e\ell}(\bar{r},E_j)W_1 f^1(E_j) \quad . \tag{1.24}$$

Consequently, the evaluation of the internal-mesh scattering source is done only by replacing Σ_t by $\Sigma_t{}'$ and Q by Q'.

The evaluation of $G(\bar{r},\bar{\Omega},E)$ in Eq.(1.2) is done on the basis of the following two assumptions with respect to the spatial variable:

1. The spatial interval $(\bar{r}',\bar{r})$ is so chosen that the revised total cross section $\Sigma_t'(\bar{r}-R'\bar{\Omega},E)$ can be assumed to be constant over that interval.
2. The external source $S(\bar{r}-R'\bar{\Omega},\bar{\Omega},E)$ can be approximated by a linear function in the interval $(\bar{r}',\bar{r})$. Then, the radiation flight path R is defined specifically as $R=|\bar{r}-\bar{r}'|$.

Then, $G(\bar{r},\bar{\Omega},E)$ is evaluated as

$$G(\bar{r},\bar{\Omega},E) = I(\bar{r}',\bar{\Omega},E)\exp(-cR) + S(\bar{r},\bar{\Omega},E)B_1(\bar{r},\bar{r}',E) + S(\bar{r}',\bar{\Omega},E)B_2(\bar{r},\bar{r}',E) \quad , \qquad (1.25)$$

where

$$B_1(\bar{r},\bar{r}',E) = [cR + \exp(-cR) - 1] / c^2R \quad , \qquad (1.26)$$

$$B_2(\bar{r},\bar{r}',E) = [1 - (1+cR)\exp(-cR)] / c^2R \quad , \qquad (1.27)$$

and

$$c = \Sigma_t'(\bar{r}-R'\bar{\Omega},E) \quad .$$

The integral calculation for $\Lambda I(\bar{r},\bar{\Omega},E)$ may be performed in a way entirely analogous to the procedure described above as,

$$\Lambda I(\bar{r},\bar{\Omega},E) = Q'(\bar{r},\bar{\Omega},E)B_1(\bar{r},\bar{r}',E) + Q'(\bar{r}',\bar{\Omega},E)B_2(\bar{r},\bar{r}',E) \quad . \qquad (1.28)$$

When a new function $H(\bar{r},\bar{\Omega},E)$ is defined as

$$H(\bar{r},\bar{\Omega},E) = S(\bar{r},\bar{\Omega},E) + Q'(\bar{r},\bar{\Omega},E) \quad , \qquad (1.29)$$

we obtain the equation

$$I(\bar{r},\bar{\Omega},E) = I(\bar{r}',\bar{\Omega},E)\exp(-cR) + H(\bar{r},\bar{\Omega},E)\cdot B_1(\bar{r},\bar{r}',E) + H(\bar{r}',\bar{\Omega},E)\cdot B_2(\bar{r},\bar{r}',E) \quad . \qquad (1.30)$$

For a large spatial interval $(\bar{r}',\bar{r})$ in which the linear source distribution approximation is not valid, the alternative approximation is provided$^{29)}$, a description of which is given in §2.2.

$$I(\bar{r},\bar{\Omega},E) = I(\bar{r}',\bar{\Omega},E)\exp(-cR) + H(\bar{r},\bar{\Omega},E)\cdot B_3(\bar{r},\bar{r}',E)\{\exp[B_4(\bar{r},\bar{r}',E)] - 1\} \quad , \tag{1.31}$$

where

$$B_3(\bar{r},\bar{r}',E) = R / B_4(\bar{r},\bar{r}',E) \quad , \tag{1.32}$$

and

$$B_4(\bar{r},\bar{r}',E) = \ell n[H(\bar{r}',\bar{\Omega},E) / H(\bar{r},\bar{\Omega},E)] - cR \quad . \tag{1.33}$$

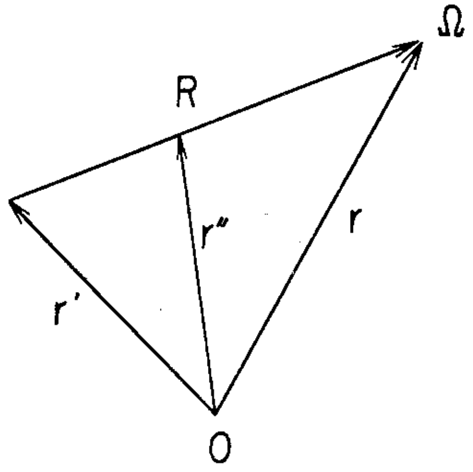

Fig.1.1 Vector system adopted.

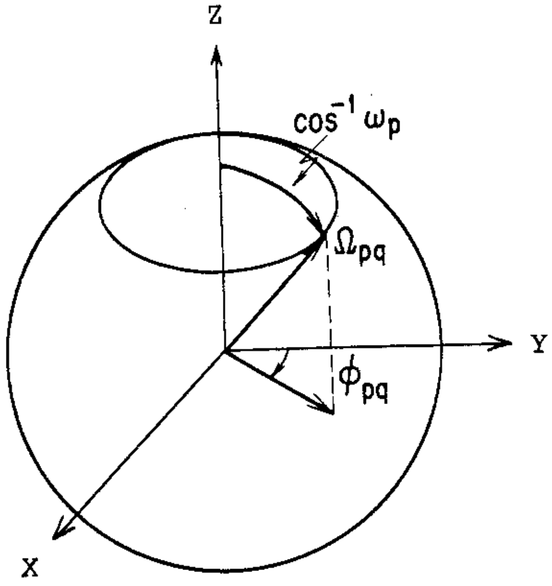

Fig.1.2 Discrete ordinates representation of radiation flight direction.

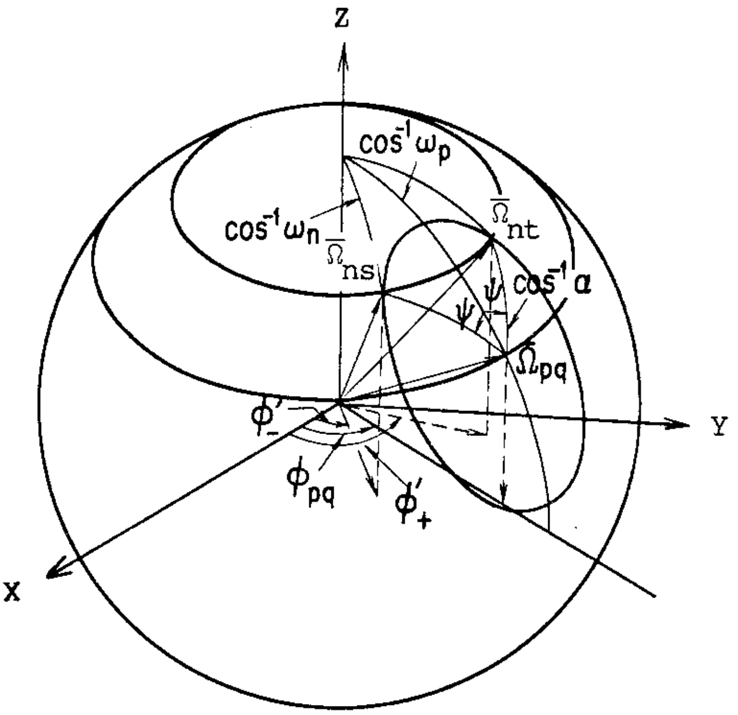

Fig.1.3 Variation of azimuthal angle of the radiation path in, before, and after scattering.

2. Calculational Method in Three-Dimensional Geometry[40)]

2.1 Fundamental Algorithm of the Method

2.1.1 Expression in Three-Dimensional (x,y,z) Geometry

The fundamental algorithm of the direct integration method[33)] is that the steady-state integral transport equation is solved by direct integration of its equation over the spatial variable in the direction of radiation flight at each discrete ordinates direction. To perform the integration over the spatial variable, the space is so partitioned into spatial meshes that the total cross section can be constant within any spatial mesh interval $(\bar{r}_{i-1},\bar{r}_i)$. The flux term is analytically integrated based on the above condition, while the source consisting of the external and scattering sources is also directly integrated over the spatial variable, based on the assumption that the source distribution can be approximated by a linear or an exponential function within the spatial interval $(\bar{r}_{i-1},\bar{r}_i)$. Upon application of the linear approximation, the angular flux at a spatial mesh point $\bar{r}_i$, expressed as (x_ℓ,y_m,z_n) in (x,y,z) geometry, is calculated from Eq.(1.30) given in terms of (x,y,z) geometry as

$$\begin{aligned} I(x_\ell,y_m,z_n,\bar{\Omega}_{pq},E_j) = {} & I(x',y',z',\bar{\Omega}_{pq},E_j)\exp(-cR) \\ & + H(x_\ell,y_m,z_n,\bar{\Omega}_{pq},E_j) \\ & \times B_1[(x_\ell,y_m,z_n),\ (x',y',z'),\ E_j] \\ & + H(x',y',z',\bar{\Omega}_{pq},E_j) \\ & \quad B_2[(x_\ell,y_m,z_n),\ (x',y',z'),\ E_j] \quad , \end{aligned} \qquad (2.1)$$

where spatial point $\bar{r}_{i-1}$ is expressed as (x',y',z'). Here, we obtain

$$B_1[(x_\ell,y_m,z_n),\ (x',y',z'),\ E_j] = [cR + \exp(-cR) - 1] / c^2R \quad , \qquad (2.2)$$

and

$$B_2[(x_\ell,y_m,z_n),\ (x',y',z'),\ E_j] = [1-(1+cR)\exp(-cR)]\,/\,c^2R \quad , \qquad (2.3)$$

where

$c = \Sigma_t{}'(x,y,z,E_j)$, revised total cross section at energy mesh point E_j defined by Eq.(1.24),

$R = |\bar{r}_i(x_\ell,y_m,z_n) - \bar{r}_{i-1}(x',y',z')| \quad ,$

which is to be determined from Eq.(2.22)

$$H(x,y,z,\bar{\Omega}_{pq},E_j) = S(x,y,z,\bar{\Omega}_{pq},E_j) + Q'(x,y,z,\bar{\Omega}_{pq},E_j)$$

$S(x,y,z,\bar{\Omega}_{pq},E_j)$ = external angular source term at $\bar{r}(x,y,z)$ having the neutron energy E_j, emitted in the discrete direction $\bar{\Omega}_{pq}$ shown in Fig.3.3 in Chapter 3

$Q'(x,y,z,\bar{\Omega}_{pq},E_j)$ = scattering source term excluding internal-mesh scattering source, given in Eq.(2.4) in accordance with Eq.(1.22).

However, the angular fluxes

$$I(\bar{r},\bar{\Omega}_{ns},E_g) \text{ and } I(\bar{r},\bar{\Omega}_{nt},E_g)$$

in Eq.(1.22) are respectively replaced with $I(\bar{r},\bar{\Omega}_{ns},E_{(m)})$ and $I(\bar{r},\bar{\Omega}_{nt},E_{(m)})$, in the present method. The reason for their replacement is that the present method treats the angular fluxes before scattering exactly with respect to the energy $E_{(m)}$ defined from the scattering angle $\cos^{-1}\mu = \cos^{-1}\mu_m$, whereas in the original method$^{33)}$ these fluxes are determined based on the assumption of 1/E spectrum within any energy mesh intervals. We obtain

$$Q'(x,y,z,\bar{\Omega}_{pq},E_j) = \sum_{g=1}^{j-1} \{ \sum_{m\in g} F_{e\ell}(x,y,z,E_{(m)},E_g)$$

$$\times \sum_n w_n [I(x,y,z,\bar{\Omega}_{ns},E_{(m)}) + I(x,y,z,\bar{\Omega}_{nt},E_{(m)})]$$

$$+ F_{in}(x,y,z,E_g,E_j) \times I_0(x,y,z,E_g)\} \quad , \qquad (2.4)$$

where

$$F_{e\ell}(x,y,z,E_{(m)},E_g) = \Sigma_{e\ell}(x,y,z,E_g) W_m f^m(E_g) \quad , \qquad (2.5)$$

from Eq.(1.16), and

$$F_{in}(x,y,z,E_g,E_j) = \Sigma_{in}(x,y,z,E_g) \cdot \frac{f_{in}(E_g,E_j)}{4\pi} \cdot (\frac{E_j}{E_g}) \Delta E_g \quad , \qquad (2.6)$$

from Eq.(1.18). Furthermore,

$$I_0(x,y,z,E_g) = \int_{4\pi} d\bar{\Omega}\, I(x,y,z,\bar{\Omega},E_g) \quad , \qquad (2.7)$$

$$E_{(m)} \equiv E(\mu_m) = (A+1)^2 E_j \,/\, (A^2 + 2A\mu_m + 1) \quad , \qquad (2.8)$$

from Eq.(1.14). Here

A = mass number of a target nuclide

μ_m = cosine of a scattering angle in the center-of-mass system (The subscript m designates a mesh point in Gaussian quadrature.)

W_m = weight of Gaussian quadrature at $\mu = \mu_m$

$f^m(E_g)$ = angular distribution function at $\mu = \mu_m$

$\bar{\Omega}_{ns}, \bar{\Omega}_{nt}$ = moving directions of neutrons before scattering (see Fig.1.3)

$\Sigma_{e\ell}(x,y,z,E_g)$ = macroscopic elastic scattering cross section

$\Sigma_{in}(x,y,z,E_g)$ = macroscopic inelastic scattering cross section

$f_{in}(E_g,E_j)$ = inelastic slowing down probability function obtained on the basis of an isotropic scattering assumption

ΔE_g = energy width for g'th mesh.

Upon application of the exponential function to the spatial mesh intervals forming rather large mean-free-paths$^{29)}$, the angular flux at $\bar{r}_i(x_\ell,y_m,z_n)$ is given by Eq.(2.9) referring to Eq.(1.31):

$$I(x_\ell,y_m,z_n,\bar{\Omega}_{pq},E_j) = I(x',y',z',\bar{\Omega}_{pq},E_j)\exp(-cR) + H(x_\ell,y_m,z_n,\bar{\Omega}_{pq},E_j) \times B_3[(x_\ell,y_m,z_n),\ (x',y',z'),\ E_j] \times (\exp\{B_4[(x_\ell,y_m,z_n),\ (x',y',z'),\ E_j]\}-1), \quad (2.9)$$

where

$$B_3[(x_\ell,y_m,z_n),\ (x',y',z'),\ E_j] = R\,/\,B_4[(x_\ell,y_m,z_n),\ (x',y',z'),\ E_j] \quad , \qquad (2.10)$$

and

$$B_4[(x_\ell,y_m,z_n),\ (x',y',z'),\ E_j] = \ell n\left[\frac{H(x',y',z',\bar{\Omega}_{pq},E_j)}{H(x_\ell,y_m,z_n,\bar{\Omega}_{pq},E_j)}\right] - cR \quad . \qquad (2.11)$$

Note that Eq.(2.9) cannot be used for

$$H(x_\ell,y_m,z_n,\bar{\Omega}_{pq},E_j) = 0 \quad ,$$

and/or

$$H(x',y',z',\bar{\Omega}_{pq},E_j) = 0 \quad ,$$

because of the functional form of Eq.(2.11), in which Eq.(2.1) should be applied in spite of the rather coarse approximation.

As is described later, the approximation by both linear and exponential functions introduces a leading error of Δ^3 ($\Delta \equiv$ spatial mesh interval), which is the same as that for the diamond difference scheme in the S_n method41). Hence, in order to improve the order of the leading error, we propose a new spatial approximation scheme using a quadratic function for the source spatial distribution.

Since the source term is calculated in advance at all the spatial meshes specified, the source spatial distribution within any restricted interval $(\bar{r}_{i-1},\bar{r}_i)$ can be approximated using the quadratic function satisfying the source conservation condition at the spatial mesh point $\bar{r}_i(x_\ell,y_m,z_n)$ of interest, and also at spatial points $\bar{r}_{i-1}(x',y',z')$ and $\bar{r}_{i+1}(x'',y'',z'')$ located on both sides of $\bar{r}_i(x_\ell,y_m,z_n)$, where spatial point $\bar{r}_{i-1}(x',y',z')$ and $\bar{r}_{i+1}(x'',y'',z'')$ do not usually coincide with any spatial mesh point. If $\bar{r}_{i+1}(x'',y'',z'')$ is so chosen that $|\bar{r}_{i+1}-\bar{r}_i| = |\bar{r}_i-\bar{r}_{i-1}| = R$, by substituting into Eq.(2.1) a source term $H(x,y,z,\bar{\Omega}_{pq},E_j)$ including external and scattering ones, approximated by a quadratic function as,

$$H(x,y,z,\bar{\Omega}_{pq},E_j) = \alpha D^2 + \beta D + \gamma \quad ,$$

the angular flux at $\bar{r}_i(x_\ell,y_m,z_n)$ is calculated from

$$\begin{aligned} I(x_\ell,y_m,z_n,\bar{\Omega}_{pq},E_j) = {} & I(x',y',z',\bar{\Omega}_{pq},E_j)\exp(-cR) \\ & + \frac{1}{c}\{\alpha[\frac{2}{c^2} - \exp(-cR)\sum_{r=0}^{2}(-1)^r \cdot \frac{2!\,R^{2-r}}{(2-r)!(-c)^r}] \\ & + \beta[\frac{1}{c} - \exp(-cR)\sum_{r=0}^{1}(-1)^r \cdot \frac{1!\,R^{1-r}}{(1-r)!(-c)^r}] \\ & + \gamma[1.0 - \exp(-cR)]\} \quad . \end{aligned} \tag{2.12}$$

Here

$$\alpha = \frac{1}{-2R^3}\begin{vmatrix} H(\bar{r}_{i-1},\bar{\Omega}_{pq},E_j) & D_{i-1} & 1 \\ H(\bar{r}_i,\bar{\Omega}_{pq},E_j) & D_i & 1 \\ H(\bar{r}_{i+1},\bar{\Omega}_{pq},E_j) & D_{i+1} & 1 \end{vmatrix} \quad , \tag{2.13}$$

$$\beta = \frac{1}{-2R^3}\begin{vmatrix} D_{i-1}^2 & H(\bar{r}_{i-1},\bar{\Omega}_{pq},E_j) & 1 \\ D_i^2 & H(\bar{r}_i,\bar{\Omega}_{pq},E_j) & 1 \\ D_{i+1}^2 & H(\bar{r}_{i+1},\bar{\Omega}_{pq},E_j) & 1 \end{vmatrix} \quad , \tag{2.14}$$

$$\gamma = \frac{1}{-2R^3}\begin{vmatrix} D_{i-1}^2 & D_{i-1} & H(\bar{r}_{i-1},\bar{\Omega}_{pq},E_j) \\ D_i^2 & D_i & H(\bar{r}_i,\bar{\Omega}_{pq},E_j) \\ D_{i+1}^2 & D_{i+1} & H(\bar{r}_{i+1},\bar{\Omega}_{pq},E_j) \end{vmatrix} \quad , \tag{2.15}$$

$$D = \sqrt{x^2 + y^2 + z^2} \quad ,$$

$$D_{i-1} = \sqrt{x'^2 + y'^2 + z'^2} \quad ,$$

$$D_i = \sqrt{x_\ell^2 + y_m^2 + z_n^2} \quad ,$$

and

$$D_{i+1} = \sqrt{x''^2 + y''^2 + z''^2} \quad .$$

When $\bar{r}_{i+1}(x'',y'',z'')$ is located beyond any boundaries of the material region where the spatial mesh point $\bar{r}_i$ belongs, Eq.(2.1) or (2.9) must be used to calculate the angular flux at $\bar{r}_i(x_\ell,y_m,z_n)$.

In order to obtain energy flux $I(x_\ell,y_m,z_n,\bar{\Omega}_{pq},E_j)$ by Eq.(2.1), (2.9) or (2.15), the spatial point $\bar{r}_{i-1}(x',y',z')$ and the flight path R must be expressed in (x,y,z) geometry. Once $\bar{r}_{i-1}$ is chosen, another unknown spatial point $\bar{r}_{i+1}$ in Eqs.(2.13), (2.14) and (2.15) is easily determined on the basis of a point symmetry condition with respect to $\bar{r}_i$.

Since the transport calculation is carried out at each angular mesh point $\bar{\Omega}_{pq}$ defined by both the polar angle $\cos^{-1}\omega$ and the aximuthal angle ϕ in neutron flight direction, the spatial point $\bar{r}_{i-1}(x',y',z')$ is determined for $\bar{\Omega}=\bar{\Omega}(\theta,\phi)$ referring to Fig.2.1 as follows:

1. For $z'=z_{n\pm1}$, $x_{\ell-1}\leqq x'\leqq x_{\ell+1}$, and $y_{m-1}\leqq y'\leqq y_{m+1}$, a mesh for $\bar{r}_{i-1}$ positions a point on the (x-y) plane at a z mesh of $z=z_{n+1}$ or $z=z_{n-1}$. Then,

$$x_\ell - x' = (z_n - z_{n\pm1})\cdot\frac{\cos\phi\cdot\sin\theta}{\cos\theta}\quad, \tag{2.16}$$

   and

$$y_m - y' = (z_n - z_{n\pm1})\cdot\frac{\sin\phi\cdot\sin\theta}{\cos\theta}\quad. \tag{2.17}$$

2. For $x'=x_{\ell\pm1}$, $y_{m-1}\leqq y'\leqq y_{m+1}$, and $z_{n-1}\leqq z'\leqq z_{n+1}$, a mesh for $\bar{r}_{i-1}$ positions a point on the (y-z) plane at an x mesh of $x=x_{\ell+1}$ or $x=x_{\ell-1}$. Then,

$$y_m - y' = (x_\ell - x_{\ell\pm1})\ \tan\phi\quad, \tag{2.18}$$

   and

$$z_n - z' = (x_\ell - x_{\ell\pm1})\cdot\frac{\cos\theta}{\cos\phi\cdot\sin\theta}\quad. \tag{2.19}$$

3. For $y'=y_{m\pm1}$, $x_{\ell-1}\leqq x'\leqq x_{\ell+1}$ and $z_{n-1}\leqq z'\leqq z_{n+1}$, a mesh for $\bar{r}_{i-1}$ positions a point on the (x-z) plane at a y mesh of $y=y_{m+1}$ or $y=y_{m-1}$. Then

$$x_\ell - x' = (y_m - y_{m\pm1})\cdot\cot\phi\quad, \tag{2.20}$$

and

$$z_n - z' = (y_m - y_{m\pm1}) \cdot \frac{\cos\theta}{\sin\phi \cdot \sin\theta} \quad . \tag{2.21}$$

Next, the flight path is determined from

$$R = [(x_\ell - x')^2 + (y_m - y')^2 + (z_n - z')^2]^{1/2} \quad . \tag{2.22}$$

2.1.2 Evaluation of Flux and Source at a Previous Spatial Point

It is now necessary to estimate both the angular flux and source at the spatial point $\bar{r}_{i-1}(x',y',z')$, since in general this point does not always coincide with any of the three-dimensional spatial mesh point defined by (x_i,y_j,z_k). As described in Ref.33, both the flux and source at $\bar{r}_{i-1}$ in two-dimensional (r,z) geometry are interpolated linearly using the values at the two mesh points adjacent to the position $\bar{r}_{i-1}$, selected either in radial or axial direction. In three-dimensional (x,y,z) geometry, however, the spatial point $\bar{r}_{i-1}(x',y',z')$ is always located on either the (x-y), (y-z), or (x-z) plane as shown in Fig.2.1. Hence, their spatial distributions should be expressed by any two-dimensional variations for estimating the flux and source at $\bar{r}_{i-1}(x',y',z')$. For this purpose, we introduce Lagrange's formula for expressing the curved surface$^{42)}$, in which a set of functional value $F(\xi_i,\eta_j)$ $(i = 1,2,\text{-----},m\ ;\ j = 1,2,\text{-----},n)$ on a certain $(\xi\text{-}\eta)$ plane are involved:

$$F(\xi,\eta) = \sum_{i=1}^{m} \sum_{j=1}^{n} W_{ij}\, F(\xi_i,\eta_j) \quad , \tag{2.23}$$

where ξ_i, η_j denote spatial mesh points located on either (x-y), (y-z) or (x-z) plane,

$$W_{ij} = U_i(\xi)V_j(\eta) \quad , \tag{2.24}$$

$$U_i(\xi) = \frac{(\xi-\xi_1)\ \text{-----}\ (\xi-\xi_{i-1})(\xi-\xi_{i+1})\ \text{-----}\ (\xi-\xi_m)}{(\xi_i-\xi_1)\ \text{-----}\ (\xi_i-\xi_{i-1})(\xi_i-\xi_{i+1})\ \text{-----}\ (\xi_i-\xi_m)} \quad , \tag{2.25}$$

and

$$V_j(\eta) = \frac{(\eta-\eta_1) \text{-----} (\eta-\eta_{j-1})(\eta-\eta_{j+1}) \text{-----} (\eta-\eta_n)}{(\eta_j-\eta_1) \text{-----} (\eta_j-\eta_{j-1})(\eta_j-\eta_{j+1}) \text{-----} (\eta_j-\eta_n)} \quad . \tag{2.26}$$

The alternative to application of Eq.(2.23) occurs when the values of fluxes and sources at adjacent spatial mesh points differ too much to be approximated by linear scale. In the case that the functional values at adjacent mesh points differ by a factor of 5 or more, an exponential variation is allowed, provided that $F(\xi_i,\eta_j) > 0$ for all i and j:

$$F(\xi,\eta) = \exp\left\{ \sum_{i=1}^{m} \sum_{j=1}^{n} W_{ij} \, \ell n[F(\xi_i,\eta_j)] \right\} \quad . \tag{2.27}$$

Since, in general, both $U_i(\xi)$ and $V_j(\eta)$ often tend to be shown oscillating functional variations for large m and n in Eqs.(2.25) and (2.26)$^{42)}$, the values $m = n = 3$ are chosen in the present method to approximate complicated spatial distributions of the angular flux and source. In this case W_{ij} in Eq.(2.24) takes the form of a biquadratic function consisting of nine mesh points on the same plane to define Eq.(2.23) or (2.27) as

$$F(\xi,\eta) = \sum_{i=1}^{3} \sum_{j=1}^{3} W_{ij} \, F(\xi_i,\eta_j) \quad , \tag{2.28}$$

and

$$F(\xi,\eta) = \exp\left\{ \sum_{i=1}^{3} \sum_{j=1}^{3} W_{ij} \, \ell n[F(\xi_i,\eta_j)] \right\} \quad . \tag{2.29}$$

The alternative option is if $\bar{r}_{i-1}(x',y',z')$ is located near any boundaries of a material region where all of the fluxes and sources at the nine spatial meshes are not always available because of crossing the boundary. In such a case, we employ a bilinear form of W_{ij} in Eq.(2.24) by setting $m = n = 2$ in Eqs.(2.25) and (2.26), in which only four spatial meshes surrounding $\bar{r}_{i-1}(x',y',z')$ are required to define $F(\xi,\eta)$ of Eq.(2.23) or (2.27) as

$$F(\xi,\eta) = \sum_{i=1}^{2} \sum_{j=1}^{2} W_{ij}\, F(\xi_i,\eta_j) \quad , \tag{2.30}$$

and

$$F(\xi,\eta) = \exp\left\{ \sum_{i=1}^{2} \sum_{j=1}^{2} W_{ij}\, \ell n[F(\xi_i,\eta_j)] \right\} \quad . \tag{2.31}$$

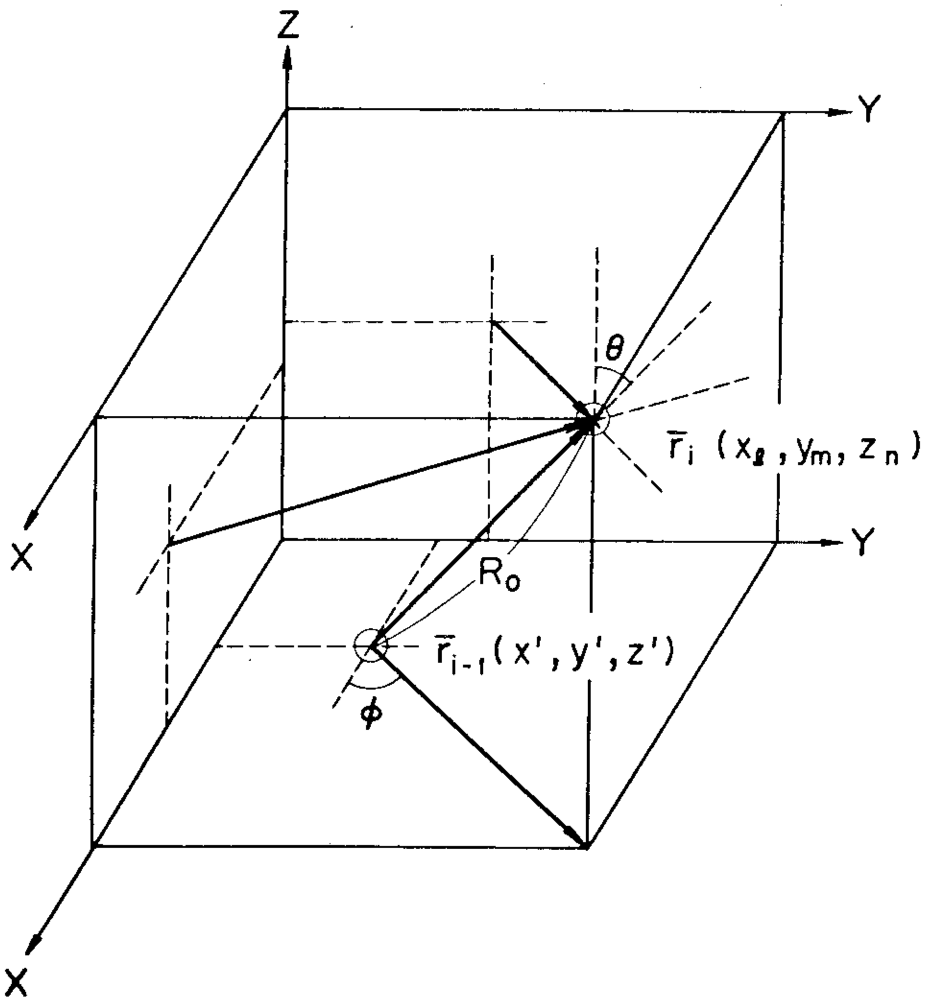

Fig.2.1 Representation of neutron flight direction in three-dimensional (x,y,z) geometry.

2.2 The Exponential Method

2.2.1 Introduction

Discrete ordinates S_n codes have been widely used for advanced shielding calculations, and the calculational accuracies have been investigated in many countries. One of the causes of calculational errors is the use of the diamond difference scheme for solving the transport equation, since this scheme does not always give positive fluxes. In such a situation, there had been no other remedy but the use of a set-to-zero function or a step function in order to supress negative fluxes whenever they occurred. The use of these fixup techniques, however, often led to additional numerical errors in shielding calculations. Accordingly, several improved methods such as the weighted diamond47), the weighted central48), and the new weighted49) difference schemes have been developed for ensuring positive fluxes. Furthremore, Barbucci and Di Pasquantonio have developed the exponential scheme50) and have shown that it always gives positive solutions without using any fixup techniques, provided that the source is non-negative and that it allows the use of large spatial meshes to obtaine solutions, always overestimating the exact solution by reasonable amounts. The exponential scheme certainly reduces numerical errors in the calculations with coarse meshes. Such errors are considered unavoidable in the S_n calculation due to its own structure, especially in problems with a steep gradient of the flux as in shielding calculations, in contrast to core calculations for which the flux is relatively flat.

On the other hand, in the direct integration method, the flux is calculated by integrating analytically the transport equation along the flight path between every two spatial mesh points adjacent to each other. Therefore, the fluxes obtained are almost rigorous except for the fact the source term, including scattering and external sources, is approximated by a linear function between two meshes to integrate numerically. Although the results of PALLAS calculations are considered to be better than those with S_n codes, there still appear relatively large numerical errors in the calculations with coarse meshes due to the approximation of the source term.

To improve the calculational accuracy, we present here a new approach that approximates the source distribution by either linear or exponential functions selected by a criterion presented later. This representation is more realistic than the one using only a linear function because of the exponential attenuation of radiation in shields. This new technique is implemented in the PALLAS-XYZ code[40), as well as in the PALLAS-PL, SP[20) and PALLAS-2DCY[21,51). With the one-dimensional PALLAS-PL, SP, extensive calculations were carried out to evaluate the calculational errors in transport problems.

2.2.2 Functional Representation of Scattering Integral

To integrate the source term on the right side of Eq.(1.2), it is necessary to approximate spatial distribution $H(\bar{r} - R\bar{\Omega}_{pq}, \bar{\Omega}_{pq}, E_j)$ by any appropriate function. Here, $H(\bar{r} - R\bar{\Omega}_{pq}, \bar{\Omega}_{pq}, E_j)$ involves scattering and external sources defined by Eq.(1.29). In the original version of the PALLAS code, $H(\bar{r} - R\bar{\Omega}_{pq}, \bar{\Omega}_{pq}, E_j)$ is approximated by a linear function within any restricted interval $(\bar{r}_{i-1}, \bar{r}_i)$. That is,

$$H(\bar{r}_i - R'\bar{\Omega}_{pq}, \bar{\Omega}_{pq}, E_j) \equiv H(\bar{r}_i - R'\bar{\Omega}_{pq}) = a(\bar{r}_i) + b(\bar{r}_i)R' \quad , \qquad (2.32)$$

which is substituted into Eq.(1.2) to obtain Eq.(1.30).

It is generally more realistic in radiation attenuation calculations for the source to be represented by an exponential function rather than by a linear one. Therefore, we introduce here a new approach to exponential function approximation to be implemented in the PALLAS code:

$$H(R') = a(\bar{r}_i)\exp\left[b(\bar{r}_i)R'\right] \quad , \tag{2.33}$$

where

$$a(\bar{r}_i) = H(\bar{r}_i) \quad ,$$

and

$$b(\bar{r}_i) = \frac{1}{R}\,\ell n\,\frac{H(\bar{r}_{i-1})}{H(\bar{r}_i)} \quad .$$

Substituting Eq.(2.33) into Eq.(1.2), we obtain the angular energy flux by Eq.(1.31) instead of Eq.(1.30). It is reasonable to represent the source distribution by an exponential function within mesh intervals in the region where the uncollided component of the fluxes is main. However, this representation is not always reasonable in the region where the scattered component is dominant, because the spatial distribution of the source may vary linearly. Thus, a compromise has been adopted between linear and exponential representations. The criterion of selection is that if $H(\bar{r}_{i-1})/H(\bar{r}_i) > 2.0$ or if $H(\bar{r}_{i-1})/H(\bar{r}_i) < 0.5$, the exponential one is used. Otherwise, the linear one is applied.

2.2.3 Calculational Results of Neutrons

A deep penetration problem of fission neutrons through water was adopted for evaluation of the numerical errors due to spatial mesh sizes. The problem was provided by Barbucci and Di Pasquantonio$^{50)}$ for evaluating numerical errors of ANISN calculations by varying the mesh size from 0.1

to 12 cm. To obtain a reference solution, we carried out the one-dimensional PALLAS calculation with a 20 angular quadrature set built in for the PALLAS code in a water slab 200 cm thick, with spatial mesh sizes of 1.0 cm (x = 0 to 42 cm), 1.5 cm (x = 42 to 192 cm), and 1.6 cm (x = 192 to 200 cm), assuming fission neutrons incident on the left plane boundary of the slab. The group constants used were generated using the RADHEAT-V3 code[53). The energy range from 14.2 MeV to 0.82 MeV was divided into 29 groups, each 0.1 lethargy unit wide.

First, a comparison was made between the two reference solutions by PALLAS and ANISN calculations, showing a fairly good agreement between them. Then, PALLAS calculations were carried out to obtain the total neutron fluxes by varying the spatial mesh size from 1.0 to 12.0 cm. The spatial intervals were assigned uniformly in almost the whole region, so that we could get a definite relation between the mesh size and the numerical errors of the total flux. The assignment of mesh sizes in our calculations went as follows:

1. Δx = 2.0 cm throughout the region
2. Δx = 4.0 cm throughout the region
3. Δx = 6.0 cm (x = 0 to 192 cm) and Δx = 4.0 cm (x = 192 to 200 cm)
4. Δx = 12.0 cm (x = 0 to 192 cm) and Δx = 8.0 cm (x = 192 to 200 cm)

The numerical errors were evaluated from the ratios of the solutions obtained with coarser meshes to the reference one.

Two solutions were obtained for each case of the above mesh assignment by using two kinds of functional representation for the source term. All total fluxes obtained were normalized to one fission source neutron. The results of calculations with the coarser meshes are plotted in Fig.2.2. Since the calculated total fluxes were not found to depend too much on the number of angular mesh points, the PALLAS calculations with 20 angular mesh points can be compared with the ANISN calculations by Barbucci and Di Pasquantonio[50)]. For comparison, the calculated results by Barbucci and Di Pasquantonio are plotted in Fig.2.3.

In Figs.2.2 through 2.5, four numerical methods are used for solving the transport equation, two implemented on ANISN and the other two on PALLAS:

1. LM = standard ANISN algorithm based on the diamond difference scheme.
2. EM = modified ANISN algorithm based on the exponential scheme proposed by Barbucci and Di Pasquantonio.
3. LP = original PALLAS algorithm with the linear function representation of the source term.
4. EP = modified PALLAS algorithm with the source term represented by a compromise between linear and exponential functions.

In ANISN calculations with a maximum mesh size of $\Delta x = 2.0$ cm, the numerical errors of LM and EM increase with the penetration distance. Contrary to this trend, the errors of LP and EP in PALLAS calculations do not always increase with the distance. In the case of calculations with the greatest coarse mesh size, ~12 cm, LP overestimates the reference solution by more than a factor of 2, but the errors of EP do not exceed 20% except for small distances. In fact, the results of EP are found to be near the reference solution at the deepest penetration distance. The errors of the four numerical methods at the deepest penetration distance with the largest mesh size are over 1700, 170, 70, and 2.2%, respectively. As is evident from the results of PALLAS calculations with a mesh size of ≤ 4.0 cm, only a small difference is seen between the results with different mesh size. Furthermore, an implementation of the EP scheme on the PALLAS gives a remarkable reduction in numerical errors without increasing the computer running time.

2.2.4 Calculational Results of Gamma-Rays

In order to investigate the numerical errors due to spatial mesh sizes in gamma-ray transport calculations, we carried out PALLAS calculations for a 50.0-cm-thick lead slab with mesh sizes varying between 0.25 and 4.0 cm. The sources adopted are (a) 1.0 MeV monoenergetic and monodirectional source incident normally on the slab face and (b) a prompt fission gamma-ray source incident isotropically on the face.
The calculated total energy fluxes were expressed in values relative to the solution obtained from the reference calculation with the mesh assignment, $\Delta x = 0.25$ cm ($x = 0$ to 24 cm) and $\Delta x = 0.5$ cm ($x = 24$ to 50 cm).
Fourteen energy meshes were assigned in an energy region from 100 keV to 1.0 MeV for the monoenergetic source problem and 24 energy meshes in an energy region from 100 keV to 8.0 MeV for the fission source problem.
Further, semi-empirical expressions of the fission gamma-ray spectrum $\Gamma(E)$ (photon·MeV^{-1}·fiss^{-1})[54) used in the calculation are:

$$\Gamma(E) = \begin{cases} 6.60 , & 0.1 \leqq E < 0.6 \text{ MeV} \\ 20.6 \exp(-1.78E) , & 0.6 \leqq E < 1.5 \text{ MeV} \\ 7.20 \exp(-1.09E) , & 1.5 \leqq E \leqq 8.0 \text{ MeV} \end{cases} . \qquad (2.34)$$

Calculations were carried out using the above two numerical methods, LP and EP, with uniformly spaced meshes of

1. $\Delta x = 0.5$ cm
2. $\Delta x = 1.0$ cm
3. $\Delta x = 2.0$ cm
4. $\Delta x = 4.0$ cm

throughout the region.

As in neutron transport calculations, Barbucci and Di Pasquantonio[50) investigated the numerical errors in the ANISN calculation for a gamma-ray deep penetration problem through a lead slab. However, their results cannot be compared with the PALLAS calculation because of a lack of detailed information. Therefore, instead of using their results, we carried out the PALLAS and ANISN calculations for the above problem. The ANISN reference solution was obtained from the $P_5 - S_{20}$ calculation with mesh sizes of $\Delta x = 0.1$ cm ($x = 0$ to 30 cm) and $\Delta x = 0.2$ cm ($x = 30$ to 50 cm).

All the results are expressed as total energy fluxes at spatial mesh points. The PALLAS results for the monoenergetic and the prompt fission gamma-ray source problems are depicted in Figs.2.4 and 2.5 in the form of ratios to the total fluxes of the respective reference solutions. The ANISN results are given in Figs.2.6 and 2.7.

For the isotropically incident fission gamma-ray source problem, the maximum error of the ANISN calculation with a mesh size of 1.0 cm is ~50%, but the errors with a mesh size of 2.0 cm or more are too large. On the other hand, the LP calculations with a mesh size of 2.0 cm or smaller give reasonable solutions (see Fig.2.5). In the case of a large mesh size such as 4.0 cm, the results of the EP method agree well with the reference solution within 4%. There appear slight differences in the ratios for mesh sizes of 2.0 cm or smaller, although these differences will not be significant. This is due to the fact that the ratios of source intensities at any adjacent mesh points are small enough to be able to represent the source distribution within a mesh interval by a linear function even in the EP calculation.

In the case of ANISN calculation for the normally incident monoenergetic gamma-ray source problem, the calculations with a mesh size of 2.0 cm or larger give an unrealistic overestimate (see Fig.2.6). On the other hand, in the PALLAS calculations shown in Fig.2.4, the errors of LP increase with an increase of the mesh size from 0.5 up to 4.0 cm.

The maximum error for the mesh size of 2.0 cm is ~50%, which is acceptable in a deep penetration problem. The errors in the EP method with a mesh size of 4.0 cm or smaller are within a few percent. Therefore, a major advantage of EP is that its errors do not depend too much on mesh sizes and source condition.

In comparing gamma-ray transport calculations with neutron calculations, it is seen that the advantage of PALLAS, especially the EP method, is more obvious in gamma-ray calculations than in neutron ones. The mean-free-path of gamma rays in lead is smaller than that of neutrons in water, so the gradient of the gamma-ray flux in lead is larger than that of the neutron flux in water. This large flux gradient may give rise to an obvious difference between the errors of PALLAS and ANISN calculations. Since PALLAS calculates the angular fluxes by integrating analytically for each set of two spatial mesh points, it can well follow the large flux gradient.
In particular, the solution by EP is better than the one by LP, because the former approximates the source distribution more accurately by using a combination of linear and exponential functions. In ANISN calculations, however, even the EM method is not sufficient to accurately express an abrupt change of the flux within a phase space cell.

2.2.5 Conclusion

A new technique has been introduced in the one-, two-, and three-dimensional PALLAS codes for evaluation of the source term through integration over the spatial variable between any mesh intervals. In order to verify the validity of the new technique of an exponential function representation for an approximation of the spatial distribution of the source term, an extensive numerical evaluation was made for the modified one-dimensional PALLAS code. The calculated results (EP) were compared with those of the original PALLAS code (LP) and the ANISN code. As a result, the following conclusions are summarized concerning the performance of the new technique:

1. The use of the new technique leads to calculations with small numerical errors irrespective of the spatial mesh size. This may enable the PALLAS code, especially the three-dimensional PALLAS-XYZ code, to be applied to deep penetration problems within a reasonable computer time by virture of the use of large spatial mesh intervals.
2. The results calculated by EP do not depend on the source conditions, therefore bringing no change to the mesh assignment in a given medium of different sources.
3. The advantage of EP is greater in gamma-ray transport calculations than in neutron ones.
4. The modification of a numerical method for the PALLAS code from LP to EP gives a reduction in numerical errors without increasing the computer running time.

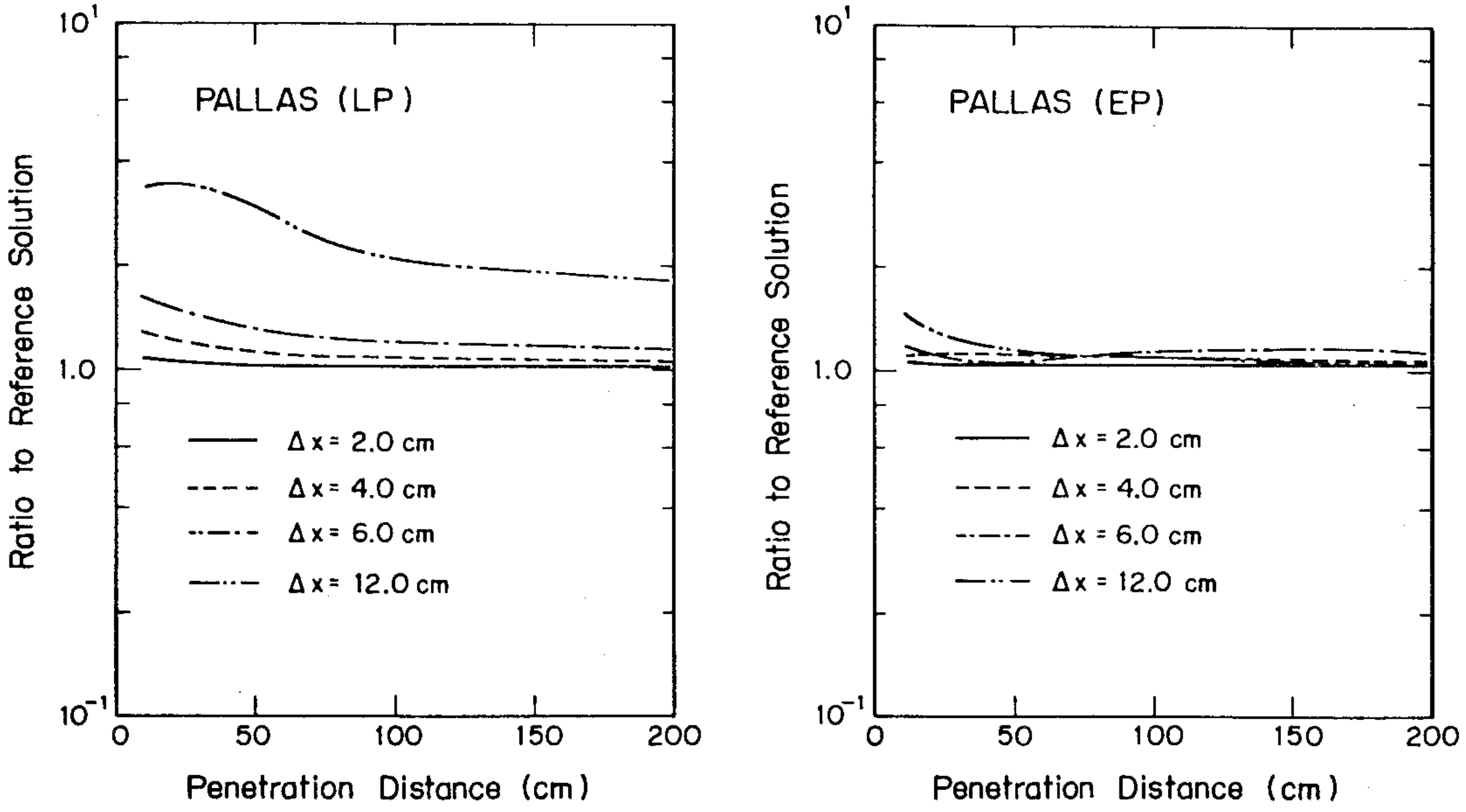

Fig.2.2 Numerical errors of PALLAS calculation due to spatial meshes for a problem of normally incident fission neutrons penetrating a 200-cm-thick water slab. LP and EP denote numerical schemes to represent the source distribution by linear function (LP) and by a combination of linear and exponential functions (EP).

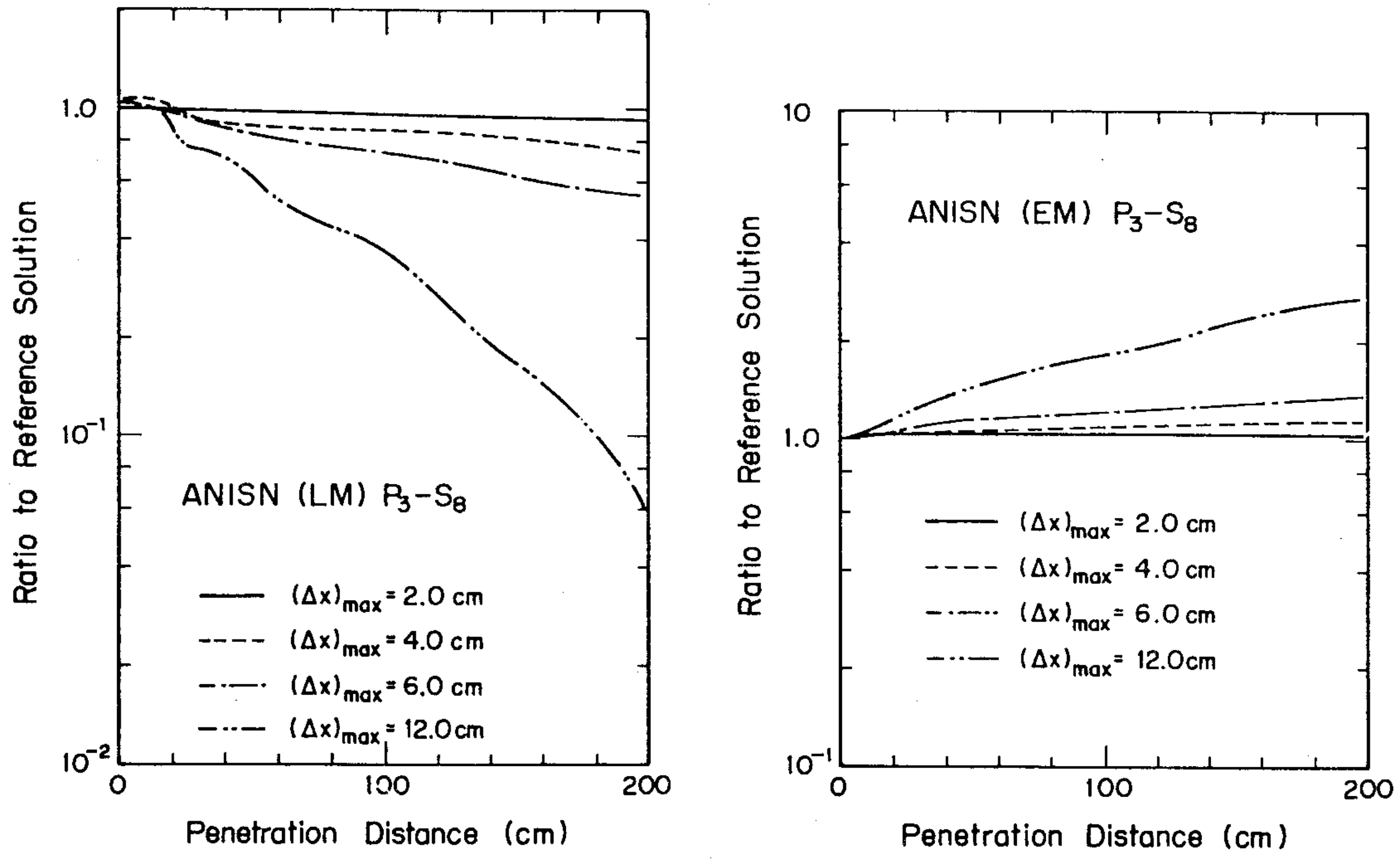

Fig. 2.3 Numerical errors of ANISN calculation due to spatial meshes for a problem of normally incident fission neutrons penetrating a 200-cm-thick water slab. LM and EM denote, respectively, diamond scheme plus step and exponential scheme.

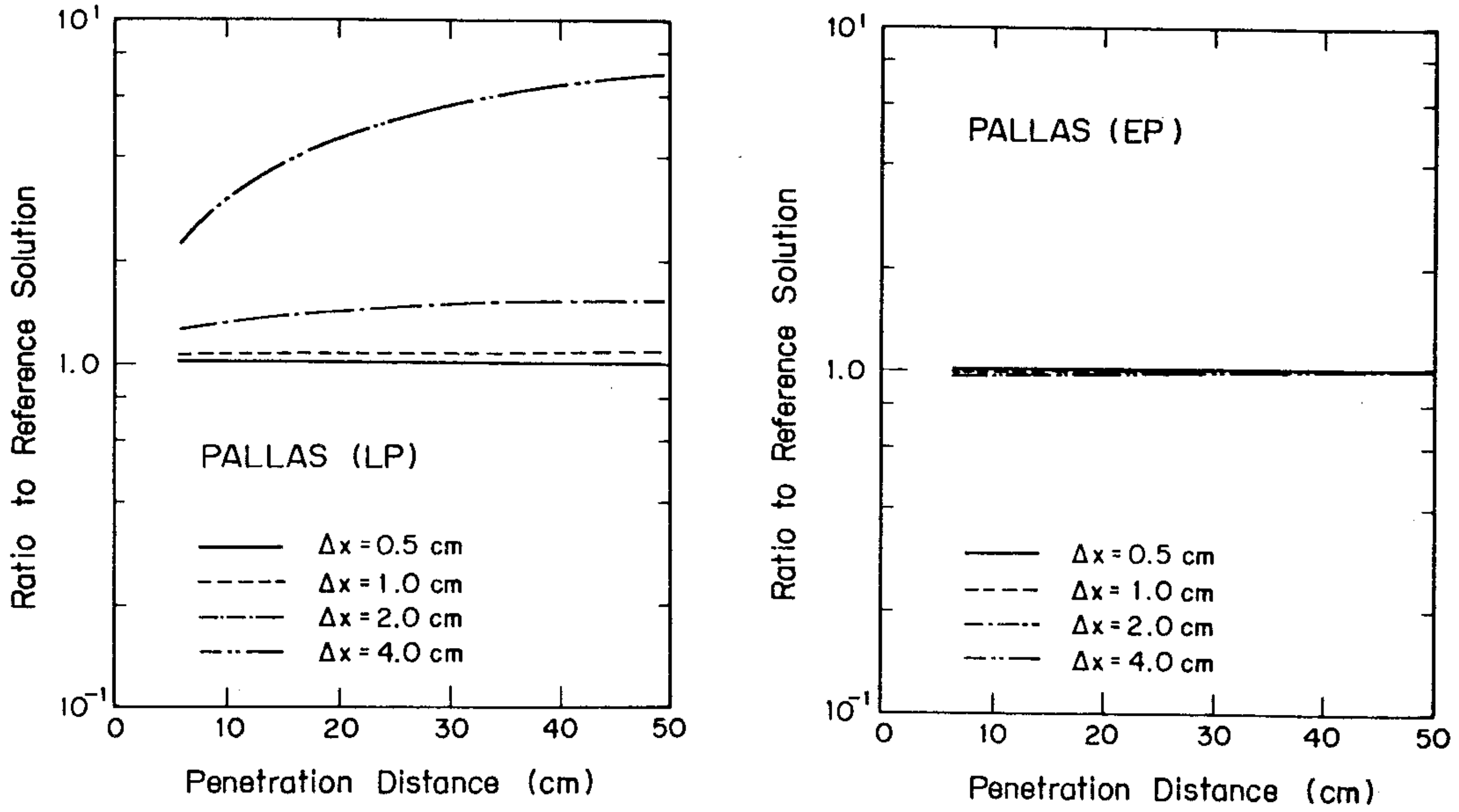

Fig.2.4 Numerical errors of PALLAS calculation due to spatial meshes for a problem of normally incident 1.0 MeV gamma-ray source penetrating a 50-cm-thick lead slab. Notations for LP and EP are the same as in Fig.2.2.

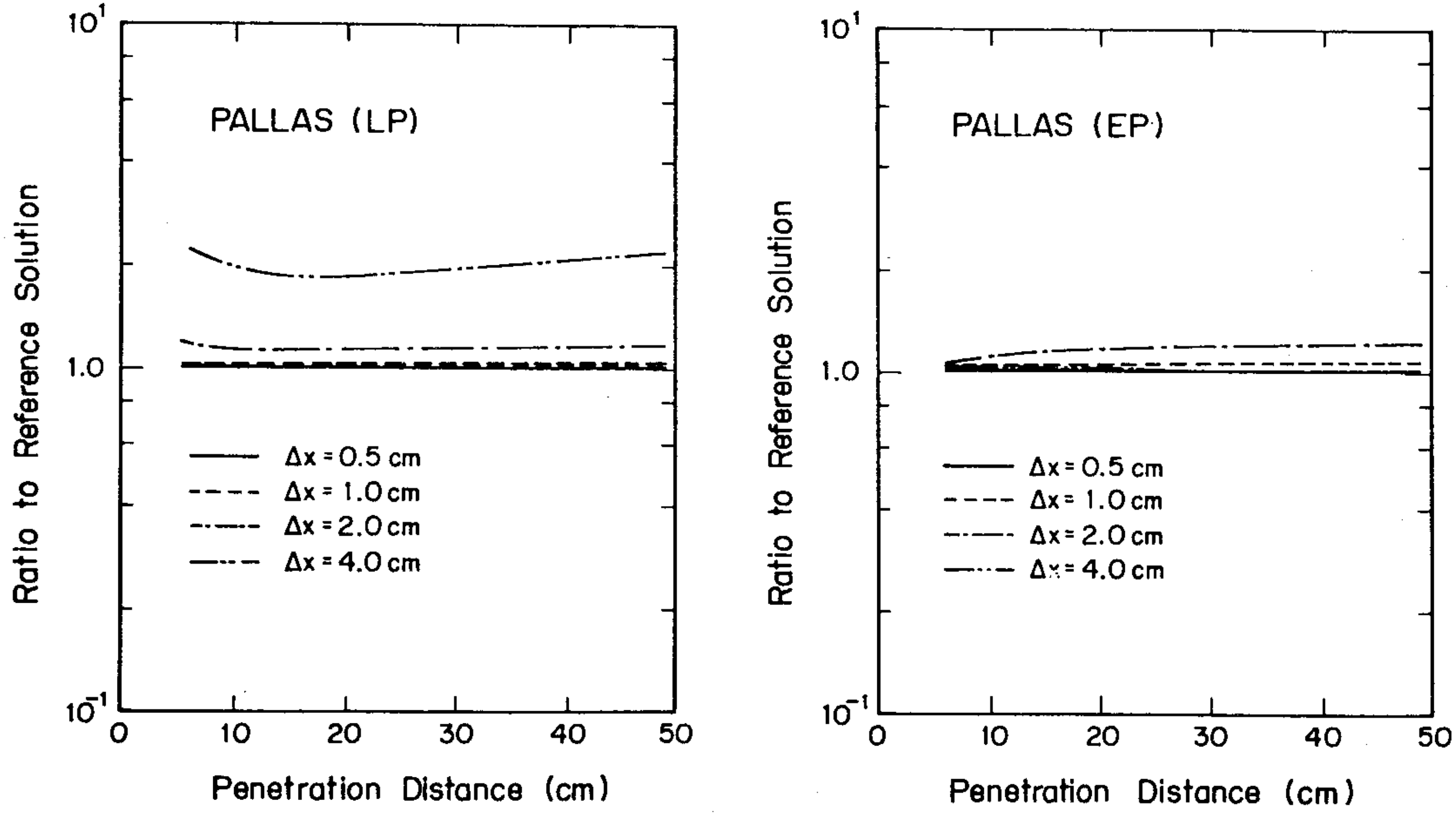

Fig.2.5 Numerical errors of PALLAS calculation due to spatial meshes for a problem of isotropically incident fission gamma-ray source penetrating a 50-cm-thick lead slab. Notations for LP and EP are the same as in Fig.2.2.

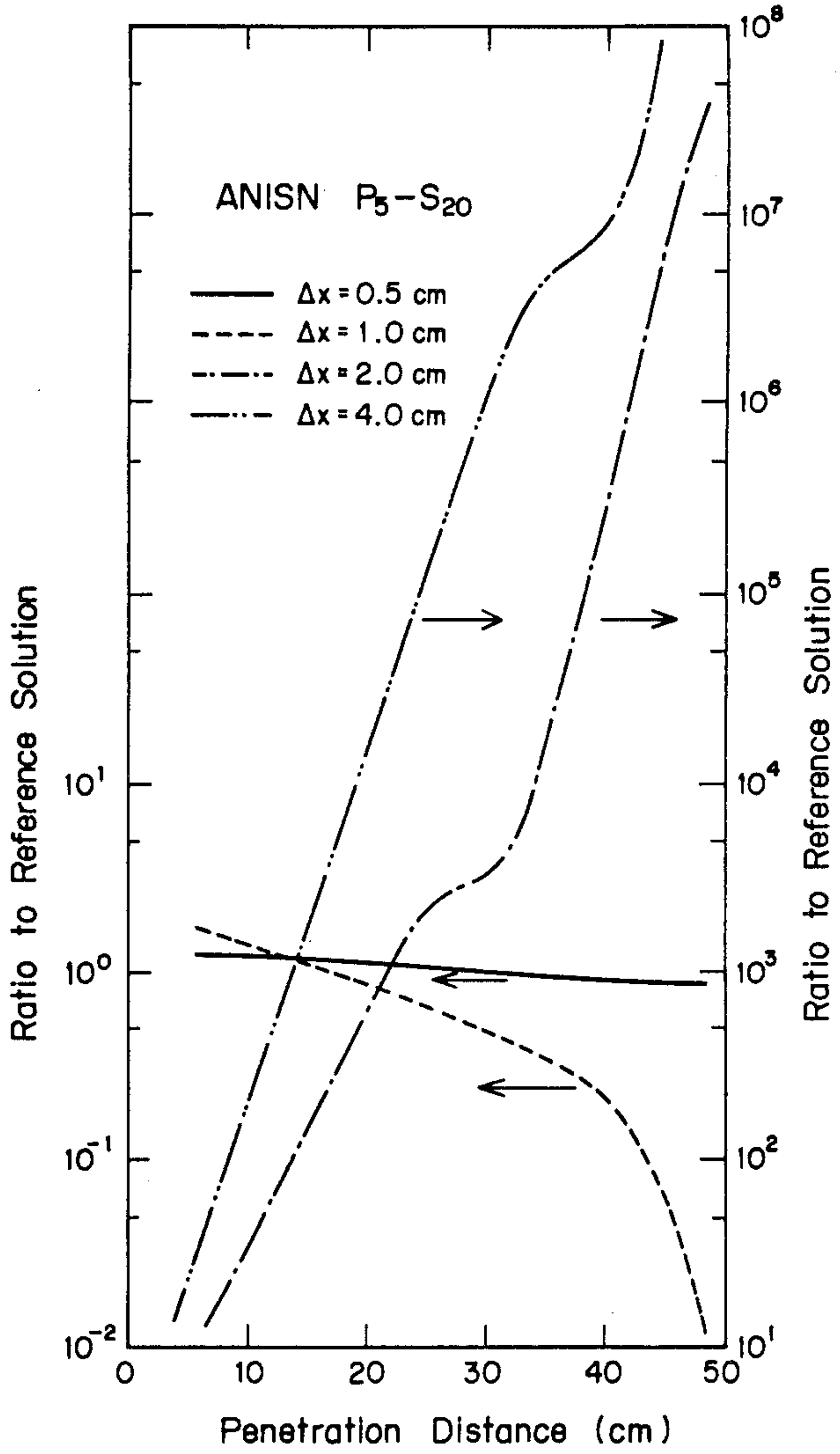

Fig.2.6 Numerical errors of ANISN calculation due to spatial meshes for a problem of normally incident 1.0 MeV gamma-ray source penetrating a 50-cm-thick lead slab.

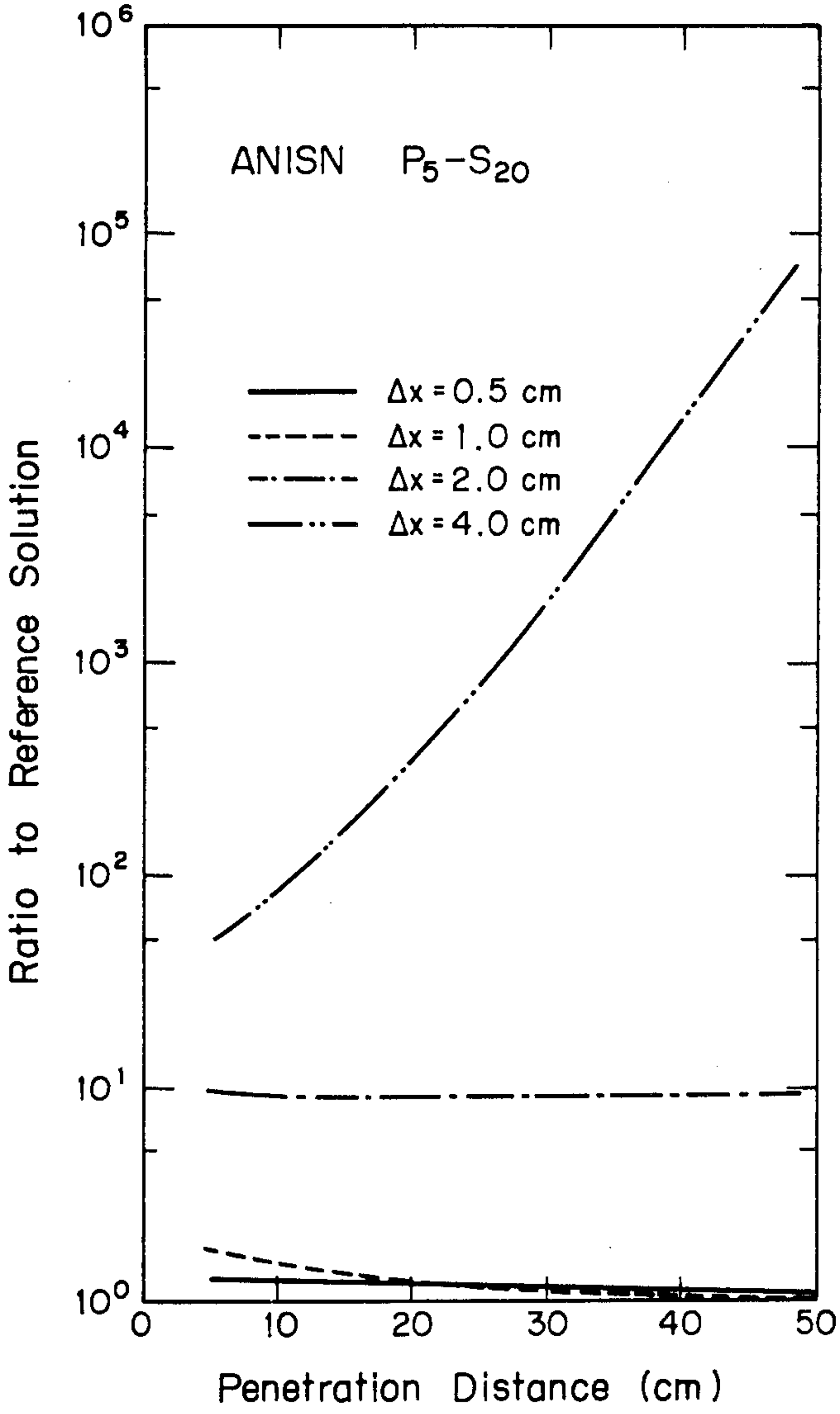

Fig.2.7 Numerical errors of ANISN calculation due to spatial meshes for a problem of isotropically incident fission gamma-ray source penetrating a 50-cm-thick lead slab.

2.3 Spectral Shape Estimation Technique

2.3.1 Fundamental Algorithm

As has already been described, the present method is formulated without the iterative techniques used in the S_n method for obtaining a solution. Instead, the present method requires fine energy meshes for the fundamental point energy calculation of neutron transport, except for thermal group calculations which are made using the conventional iterative technique. Whereas the straightforward technique used for the internal-mesh scattering calculation has been successfully applied to one- and two-dimensional PALLAS calculations, the use of such fine energy meshes is not adequate for three-dimensional transport calculations from the standpoint of computer running time.

To overcome this difficulty, we have introduced a new technique to keep the straightforward technique still valid for application to transport calculations with coarse energy meshes. This technique enables us to evaluate more accurately the energy flux $I(\bar{r},\bar{\Omega},E_{(m)})$ at an energy $E_{(m)}$ defined at $\mu=\mu_m$ in Eq.(2.4), since $I(\bar{r},\bar{\Omega},E_{(m)})$ must be evaluated from previously known values of $I(\bar{r},\bar{\Omega},E_k)$ at energy mesh points E_k $(k=1,2,\text{-----},j\text{-}1)$ in the energy region above the energy mesh point E_j of interest. A difficulty arises in the case of $E_{j-1} > E_{(m)} > E_j$ due to an invalid interpolation in determining the flux at $E_{(m)}$. When the energy spectral shape is approximated in such a way that $I(\bar{r},\bar{\Omega},E) = \text{constant}$ (1/E spectrum) as plotted by dashed lines to the left in Fig.2.8, then the flux at $E_{(m)}$ can be obtained from[33)]

$$I(\bar{r},\bar{\Omega},E_{(m)}) = I(\bar{r},\bar{\Omega},E_{j-1}) \quad . \tag{2.35}$$

This assumption, however, is valid only when an energy mesh interval is chosen so small as to approximate the energy spectrum by the 1/E spectrum. For a rough energy mesh interval, such as the one shown to the right in Fig.2.8, we find that the difference of the energy flux between 1/E and the actual flux becomes large. Consequently, adoption of the 1/E spectrum results in a considerable underestimation in the scattering calculation through Eq.(2.4). In such a case, we need some weight functions for approximating the actual energy spectral shape. It would be ideal to apply the actual energy spectral shape at the spatial point of interest; however, this is unrealistic. In stead of applying the actual energy spectral shape, we utilize an approximated one calculated with the one-dimensional PALLAS transport option implemented in the three-dimensional PALLAS-XYZ code as one of its subroutines.

A three-dimensional transport calculation, therefore, requires in advance, a one-dimensional neutron transport calculation with fine energy meshes for obtaining energy spectral shapes in finely divided material subregions. Now let $f_i(E)$ be the representative neutron energy spectrum in the i'th submaterial region, which is calculated at specified fine energy mesh points E_k with the one-dimensional PALLAS-PL, SP code[20] as

$$f_i(E_k) = I_0(x_\ell, E_k) \quad , \tag{2.36}$$

where

$$I_0(x_\ell, E_k) = \int d\bar{\Omega}\; I(x_\ell, \bar{\Omega}, E_k) \quad ,$$

the energy scalar flux at the energy mesh point E_k at a middle spatial mesh point x_ℓ within the i'th region. The rough energy mesh points E_j used for a three-dimensional calculation are always chosen so as to coincide with certain meshes in the fine energy mesh points E_k. Then the representative energy flux $f_i(E_{(m)})$ at $E_{(m)}$ defined at $\mu = \mu_m$ is determined by interpolating linearly the values of $f_i(E_k)$ at two energy mesh points adjoining the energy $E_{(m)}$. Thus, the energy flux at $E_{(m)}$ for the three-dimensional calculation can be obtained from

$$I(\bar{r},\bar{\Omega},E_{(m)}) = I(\bar{r},\bar{\Omega},E_{j-1}) \cdot f_i(E_{(m)}) / f_i(E_{j-1}) \quad . \qquad (2.37)$$

The above calculation is made for all the spatial meshes $\bar{r}_i$ belonging to the i-th submaterial region.

Introduction of this technique to the three-dimensional transport calculation enables us to apply it to practical neutron transport calculations with rather rough energy meshes, such as 0.4 lethargy intervals, even in the energy region above 0.1 MeV.

2.3.2 Validation of the Technique[40)]

An experiment of deep penetration through an iron slab[55)] is adopted for verifying the validity of this technique. The experimental configuration consists of a uranium fission converter, iron slabs ~150 cm thick, and other auxiliary components as accurately expressed by the two-dimensional (r,z) geometrical model in Fig.2.9. Based on this calculational model, the models for three-dimensional (x,y,z) geometry and for one-dimensional infinite plane geometry are obtained, respectively, as in Figs.2.10 and 2.11. An iron region of 100 cm in depth is considered here because the calculational results are to be compared with the experiment at a penetration distance up to 85 cm from the slab surface. While in the actual experimental set-up, iron slabs 5.85 cm thick are separated by a void region 0.635 cm thick utilized for setting neutron detectors, the laminated iron and void layers are assumed in the present calculation to be homozenized, resulting in diluted iron slab with a reduced number density of

7.543×10^{22} cm^{-3}. In three-dimensional calculations, a uniform spatial mesh interval of 6.25 cm in the axial direction was applied to the iron slab. Even with such a large spatial interval, the PALLAS-XYZ calculation was confirmed not to bring any serious errors to the solution owing to the use of the exponential method. To take account of spectral change in the iron slab as a function of penetration, the whole iron region is divided into four subregions 25 cm thick each. The one-dimensional weight functions are to be obtained for every subregions based on the energy fluxes at the corresponding subregions. In general, PALLAS calculation with coarse energy mesh is inadequate for accurately representing an abrupt increase in the energy spectrum around 1.0 MeV in deep penetration through heavy materials such as iron. For this reason, we employed this experiment to verify the validity of the application of the spectral shape estimation technique based on a one-dimensional transport calculation.
Comparisons are to be made of the neutron spectra at 22.6 cm (nominal 8-in.-thick), 56.6 cm (nominal 20-in.-thick), and 84.9 cm (nominal 30-in.-thick) distances from the front of the iron slab.

Group-averaged cross sections were generated using the RADHEAT-V3 code53) based on the basic data from the ENDF/B-IV library. Elastic scattering distribution functions at all energy meshes used in the calculation were generated by using all the Legendre polynomial coefficients included in the ENDF/B-IV library. Further, a self-shielding factor of iron for obtaining effective cross section data is calculated by using a RIFF code56) with an ultra-fine equi-lethargy energy structure of 0.0021 lethargy.

The calculation was carried out on the basis of the boundary source condition given below55,57) at the converter surface in the calculational model presented in Fig.2.9

$$\phi(r,E) = \nu \times 0.84\ e^{-E}\ \sinh(2E)^{1/2} \times 3.345 \times 10^{3} \times \cos(\pi r/142.9)\ ,\quad [n \cdot cm^{-2} \cdot s^{-1} \cdot MeV^{-1}]\ , \qquad (2.38)$$

where ν is a number of neutrons emitted by one fission reaction, and r and E are, respectively, radial distance and neutron energy in MeV. In the present calculation, we utilized number densities of iron with 7.543×10^{22} cm^{-3} for the iron slab and of aluminum with 4.633×10^{22} cm^{-3} for the aluminum plate. The PALLAS makes scattering calculations for every nuclide in the material region of interest as is apparent from Eq.(1.6), then, in order to save computer running time, all other minor nuclides are replaced by the dominant nuclides, iron or aluminum nuclide.

We made two calculations to verify the validity of the new technique introduced: one was with the weight functions obtained from the one-dimensional calculation and the other was without them. While the three-dimensional calculation was made with 0.4 equi-lethargy intervals, the one-dimensional one utilized 0.1 equi-lethargy intervals which are finer than those of 0.2 lethargy usually used in the actual two-dimensional PALLAS calculations[9)].

Figure 2.12 gives scalar energy fluxes $I(\bar{r},E)$ at the midpoint within every four subregions of the iron slab. From these, space dependent weight functions $f_i(E_{(m)})/f_i(E_{j-1})$ from Eq.(2.37) are determined. They are all normalized at $E = 14.2$ MeV, the first energy mesh. As is apparent in the figure, the spectrum shows more steep gradient above 0.5 MeV with the penetration depth from the slab surface, indicating a strong space dependency of the spectrum. It is therefore, absolutely necessary for the calculation with coarse energy meshes to take into account their space dependency adequately, instead of using approximations by 1/E spectrum as is adopted in the current version of the one- and two-dimensional PALLAS codes. As is evident from Fig.2.12, the deviation of the 1/E spectrum (flat lethargy spectrum) from the spectral weight function increases with the penetration distance through the iron slab. Therefore, the calculational accuracy without weight function can be predicted to decrease with the penetration distance. This trend is apparently reflected from the results given in Figs.2.13 through 2.15.

These figures provide comparisons of the calculations with the experiments at penetrations of nominally 8, 20 and 30 in. measured from the slab surface. As is evident from the figures, the calculations without using the weight function are respectively smaller than 1/10, 1/200, and 1/2000 as compared with the measured spectra at penetrations of 8, 20, and 30 in. The figures indicate that the calculations made using the weight functions can provide fairly accurate results, although there appear to be slight overestimates in the energy region $0.15 < E < 0.6$ MeV at penetrations of 8 and 20 in. and a considerable underestimate in the energy region $0.8 < E < 2$ MeV at a penetration of 30 in. The cause of these differences has not been clearly determined yet and is being investigated at present.

The transport calculation with the weight function required 28 min, 22 s CPU on the FACOM-M200 for 14 energy meshes with $15 \times 15 \times 23$ spatial meshes and 56 angular meshes, whereas the calculation without using the weight function required 28 min, 16 s. A negligibly small increase in CPU in order to add the one-dimensional calculation for obtaining the weight function is allowed to obtain a significant improvement in the accuracy of three-dimensional calculations with coarse energy meshes.

As a result of the above consideration, use of the spectral shape estimation technique has been found to enable us to perform PALLAS-XYZ calculations accurately with coarse energy meshes, which in turn leads to a considerable saving of computer running time.

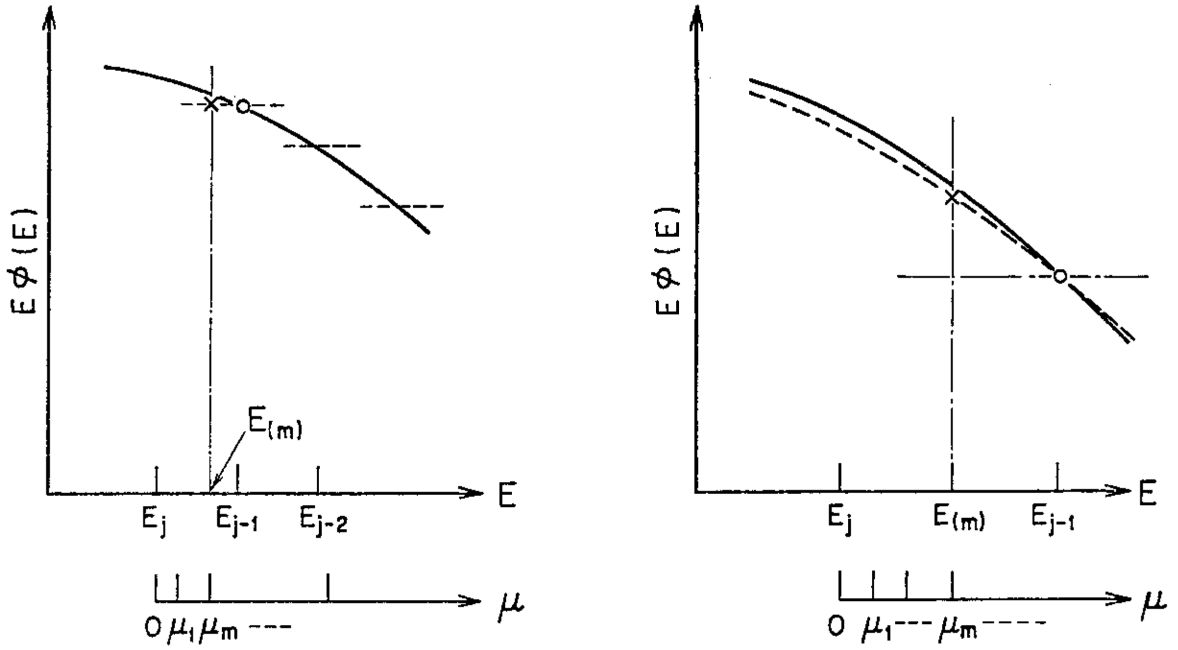

Fig.2.8 Determination of energy flux at an energy point $E_{(m)}$ defined at $\mu=\mu_m$. The left curve is for a 1/E spectrum approximation and the right is for a one-dimensional spectral shape approximation.

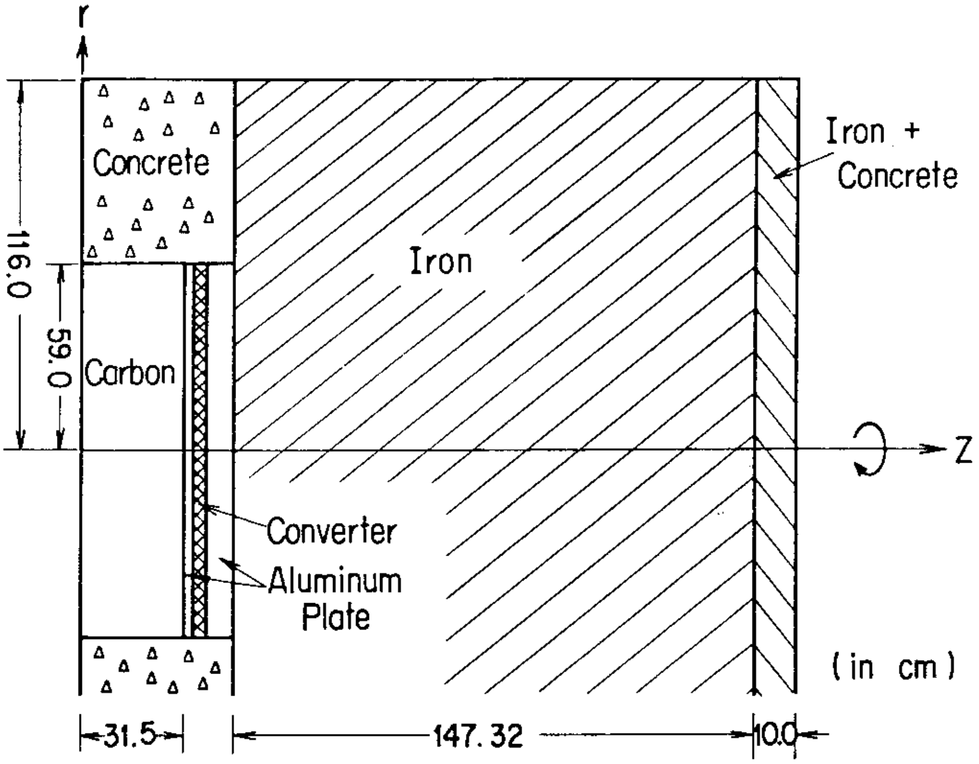

Fig.2.9 Simplified configuration of neutron deep penetration experiment through iron slab.

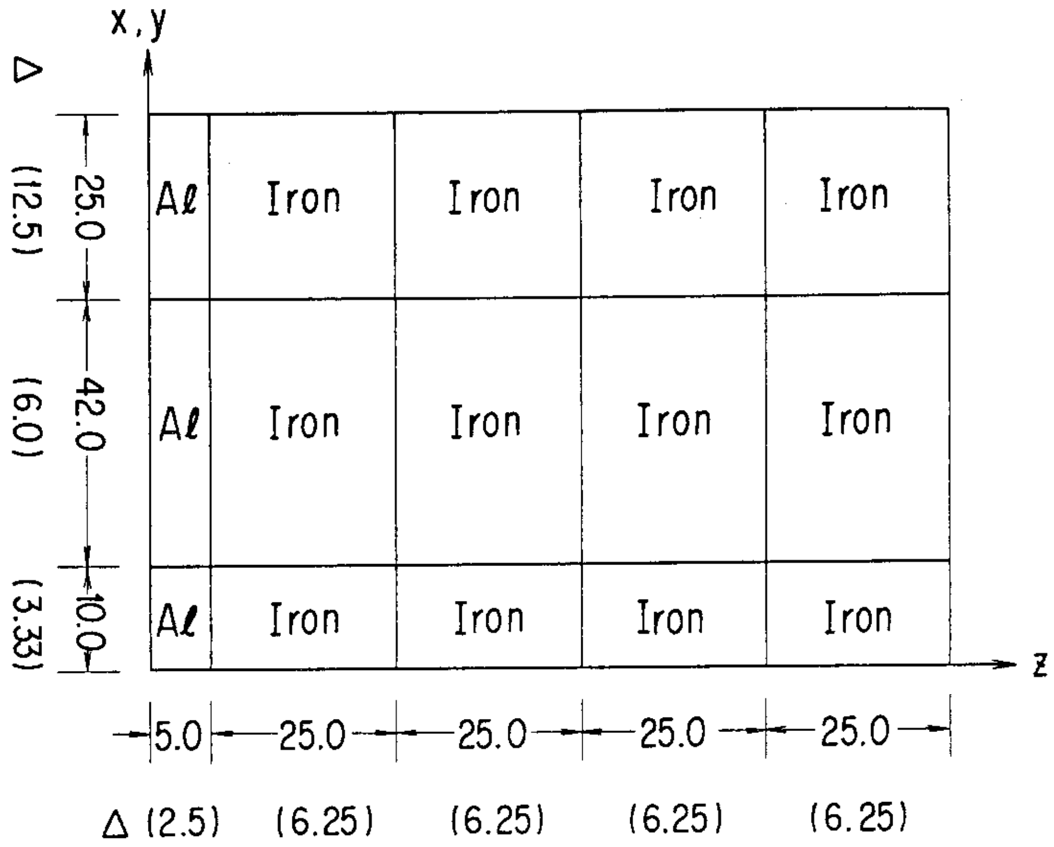

Fig.2.10 Calculational model of neutron deep penetration experiment through iron slab for three-dimensional PALLAS-XYZ. Δ designates mesh interval in unit of cm.

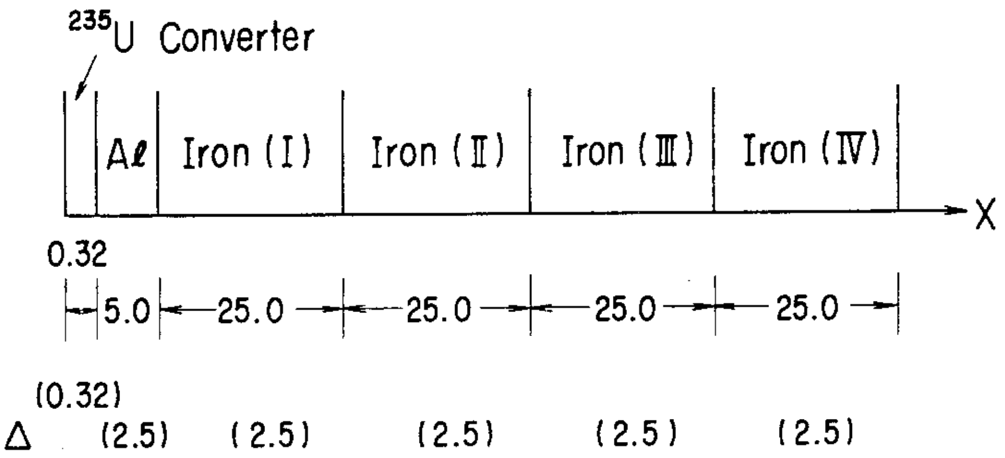

Fig.2.11 Calculational model of neutron deep penetration experiment through iron slab for one-dimensional PALLAS-PL,SP in plane geometry. Δ designates mesh interval in unit of cm.

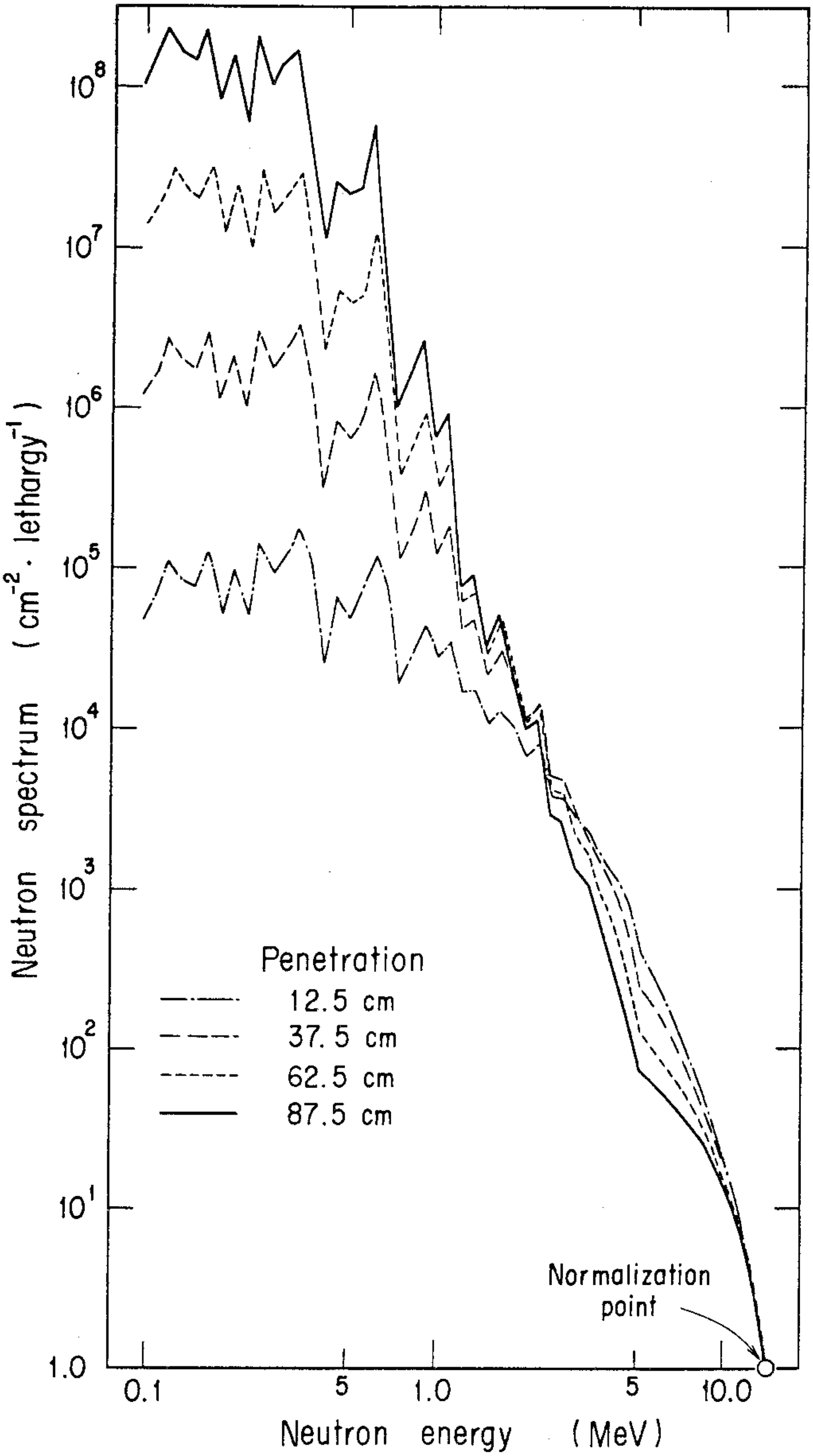

Fig.2.12 Energy flux at the midpoint of each subregion of iron.

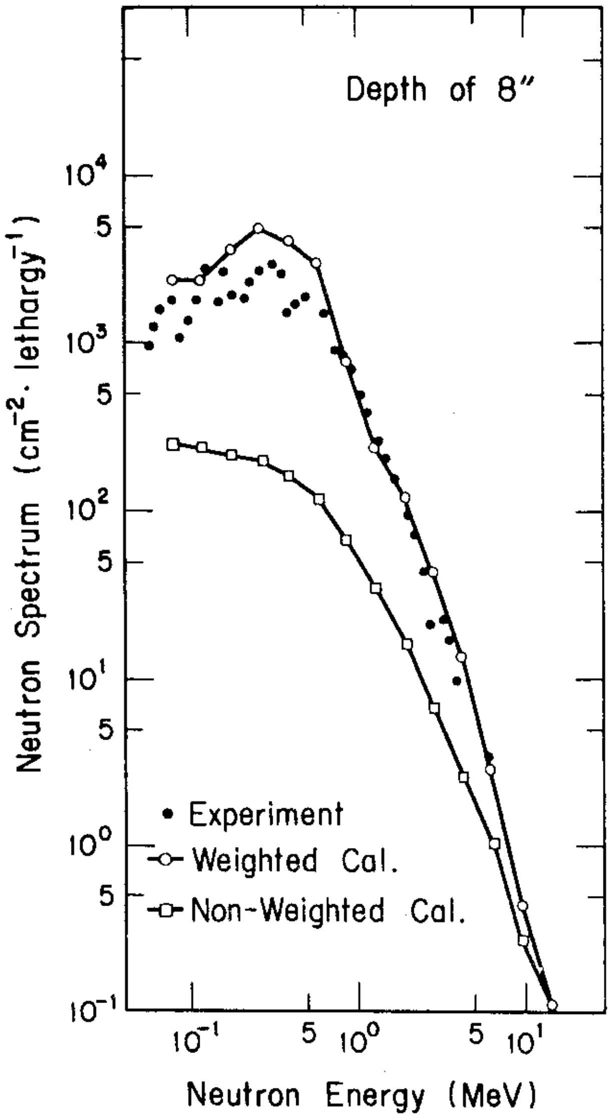

Fig.2.13 Comparison of PALLAS calculated with the experimental neutron spectra at a penetration of 8 in.

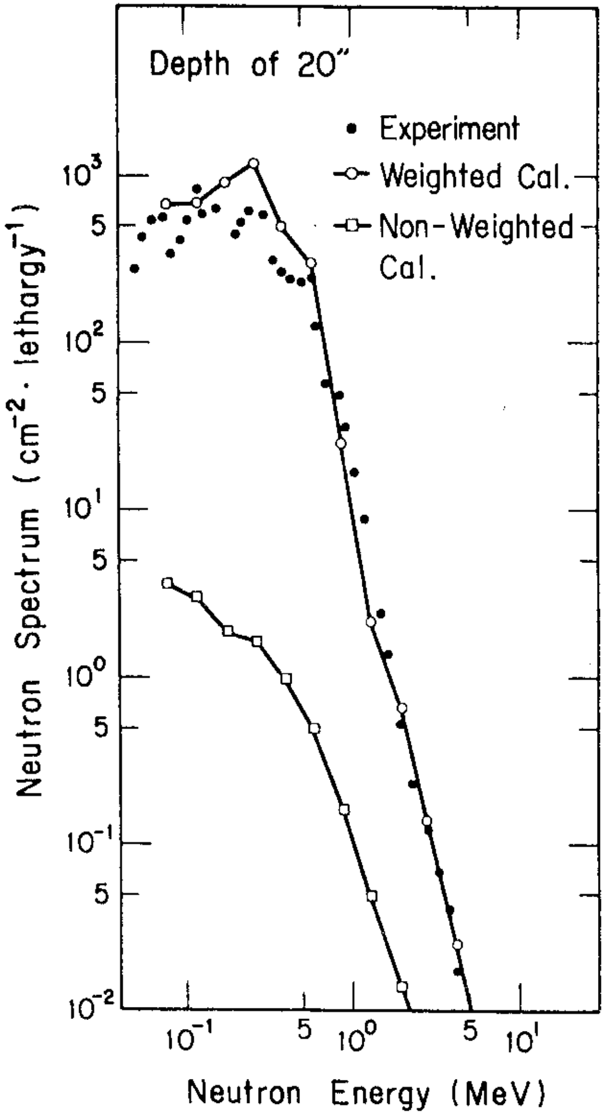

Fig.2.14 Comparison of PALLAS calculated with the experimental neutron spectra at a penetration of 20 in.

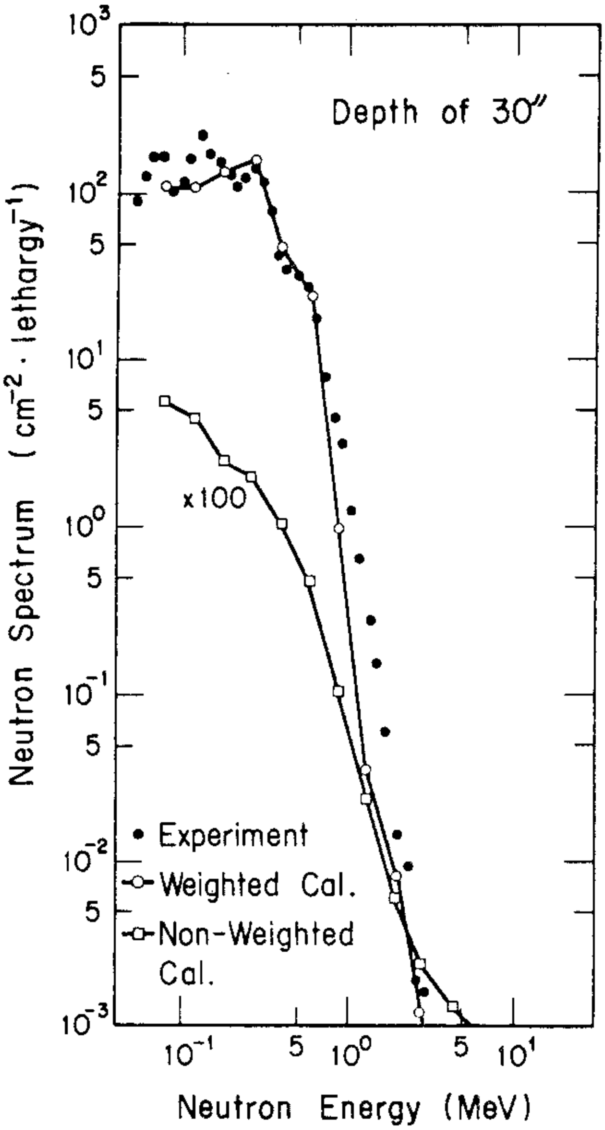

Fig.2.15 Comparison of PALLAS calculated with the experimental neutron spectra at a penetration of 30 in.

2.4 Error Analysis of the Direct Integration Method

2.4.1 Introduction

In a radiation transport code PALLAS based on the direct integration method[33], angular flux Φ at a certain spatial mesh $\bar{r}_{i+1}$, neglecting variables of both energy and angle, takes the following form:

$$\Phi(\bar{r}_{i+1}) = \Phi(\bar{r}_i)\exp(-\Sigma_t R) + \int S(\bar{r}'')\exp(-\Sigma_t R')dR' \quad , \tag{2.39}$$

where

$R = |\bar{r}_{i+1} - \bar{r}_i|$

$R' = |\bar{r}_{i+1} - \bar{r}''|$

$\bar{r}'' = \bar{r}_{i+1} - R'\bar{\Omega}$

$\bar{\Omega}$ = flight direction of radiation

Σ_t = macroscopic total cross section

$S(\bar{r})$ = source spatial distribution.

The first term on the right side of Eq.(2.39) forms an analytical solution, which gives no spatial error. In the second term, however, the source is numerically evaluated only at mesh points specified in advance. Hence, approximation of the source distribution introduces some errors in the integral calculation of the second term on the right side of Eq.(2.39).

Evaluation of the error is carried out through spatial approximation of the source distribution by linear and exponential functions used in the current version of PALLAS code[33]. In addition, evaluation is also made for a quadratic function approximation, which is expected to give a higher degree of spatial approximation than those for currently used functions.

2.4.2 Method of Error Analysis

In the case of one-dimensional plane geometry, Eq.(2.39) is simplified to obtain the solution as

$$\phi_{i+1} = \phi_i \exp(-f_i) + \frac{1}{\mu}\int_0^{\Delta_i} S(x_{i+1} - t) \exp(a_i t)dt \quad , \qquad (2.40)$$

where

$$\phi_{i+1} \equiv \phi(\bar{r}_{i+1})$$
$$\phi_i \equiv \phi(\bar{r}_i)$$
$$f_i = \Sigma_t \Delta_i / \mu$$
$$\Delta_i = x_{i+1} - x_i$$
$$a_i = -\Sigma_t / \mu$$
$$t = x_{i+1} - x$$

and where μ and Σ_t are respectively the cosine of polar angle in radiation moving direction and the macroscopic total cross sections. Let $L_i(x)$ denote a function approximating a variation of $S(x)$ within any mesh intervals. Then the difference between the exact and approximate solutions is obtained as

$$\text{Error} = \frac{1}{\mu}\int_0^{\Delta_i} dt \exp(a_i t)[S(x_{i+1} - t) - L_i(x_{i+1} - t)] \quad . \qquad (2.41)$$

Let us introduce a new function $f(x)$ as

$$f(t) = \exp(a_i t)[S(x_{i+1} - t) - L_i(x_{i+1} - t)] \quad ,$$

which is expanded by the Taylor series at $x = x_{i+1}$ leading to

$$f(t) = \sum_{n=0}^{\infty} \frac{t^n}{n!} \left\{ \exp(a_i t)[S(x_{i+1} - t) - L_i(x_{i+1} - t)] \right\}^{(n)}_{x=x_{i+1}} \quad . \qquad (2.42)$$

By differentiating Eq.(2.42) n times, we can rewrite f(t) as

$$f(t) = \sum_{n=0}^{\infty} \frac{t^n}{n!} \sum_{r=0}^{n} \binom{n}{r} \exp(a_i t)^{(n-r)}_{t=0} (-1)^r \times [S(x) - L_i(x)]^{(r)}_{x=x_{i+1}}$$

$$= \sum_{r=0}^{\infty} [S^{(r)}_{i+1} - L^{(r)}_{i+1}] \times \sum_{s=0}^{\infty} \frac{a_i{}^s}{r!s!} t^{r+s} \quad , \qquad (2.43)$$

where $s = n-r$. Substituting Eq.(2.43) into Eq.(2.41), we obtain an expression ε for error estimation as follows[41]:

$$\varepsilon = \frac{1}{\mu} \int_0^{\Delta_i} f(t)dt$$

$$= \frac{1}{\mu} \sum_{r=0}^{\infty} (D^r S_{i+1} - D^r L_{i+1}) \times \sum_{s=0}^{\infty} \frac{a_i{}^s}{r!s!(r+s+1)} \Delta_i^{r+s+1} \quad , \qquad (2.44)$$

where

$$D^r S_{i+1} = \left. \frac{d^r S}{dt^r} \right|_{t=0} = (-1)^r \left. \frac{d^r S}{dx^r} \right|_{x=x_{i+1}}$$

and

$$D^r L_{i+1} = \left. \frac{d^r L_i}{dt^r} \right|_{t=0} = (-1)^r \left. \frac{dL_i}{dx^r} \right|_{x=x_{i+1}} \quad .$$

Thus, we can obtain the degree of spatial approximation by substituting approximated functions into Eq.(2.44).

2.4.3 Evaluation of Degree of Spatial Approximation

(I) Linear Variation for $L_i(x)$

For a linear variation, $L_i(x)$ takes the form as

$$L_i(x) = C_{i0} + C_{i1}(x - x_i) \quad , \qquad (2.45)$$

where $C_{i0} = S_i$ and $C_{i1} = (S_{i+1} - S_i)/\Delta_i$ from the source conservation condition at $x = x_i$ and x_{i+1}.

To evaluate ε by Eq.(2.44), we obtain $D^r L_{i+1}$ $(r > 0)$ by the Taylor series as follows:

$$L_{i+1} = L(x_{i+1}) = C_{i0} + C_{i1}\Delta_i = S_{i+1} \quad , \tag{2.46}$$

and

$$DL_{i+1} = (-1)C_{i1} = \frac{-(S_{i+1} - S_i)}{\Delta_i} \quad , \tag{2.47}$$

where S_i is expressed also by the Taylor series as

$$S_i \equiv S(x_i) = \sum_{p=0}^{\infty} \frac{D^p S_{i+1}}{p!} \Delta_i^{\,p} \quad . \tag{2.48}$$

Substituting Eq.(2.48) into Eq.(2.47), we obtain

$$DL_{i+1} = DS_{i+1} + \sum_{p=0}^{\infty} \frac{D^{p+2} S_{i+1}}{(p+2)!} \Delta_i^{\,p+1} \quad , \tag{2.49}$$

using the expression

$$\sum_{p=0}^{\infty} \frac{D^p S_{i+1}}{p!} \Delta_i^{\,p} = \sum_{q=0}^{N} \frac{D^q S_{i+1}}{q!} \Delta_i^{\,q} + \sum_{p=0}^{\infty} \frac{D^{p+N+1} S_{i+1}}{(p+N+1)!} \Delta_i^{\,p} \quad (N \geqq 0). \tag{2.50}$$

Further, it is evident from Eq.(2.45)

$$D^r L_{i+1} = 0 \quad (r > 1) \quad . \tag{2.51}$$

Substituting Eqs.(2.46), (2.49) and (2.51) into Eq.(2.44), we obtain

$$\mu\varepsilon = - \sum_{p=0}^{\infty} \frac{D^{p+2} S_{i+1}}{(p+2)!} \Delta_i^{\,p+1} \left\{ \frac{1}{2} \Delta_i^{\,2} + \frac{a_i}{3} \Delta_i^{\,3} + \text{-----} \right\}$$

$$+ D^2 S_{i+1} \left\{ \frac{1}{6} \Delta_i^{\,3} + \frac{a_i}{8} \Delta_i^{\,4} + \text{-----} \right\} \quad ,$$

which is rearranged in ascending series of Δ_i to yield

$$\varepsilon = -\frac{1}{\mu} D^2 S_{i+1} \frac{\Delta_i^3}{12} + O(\Delta_i^4) \quad , \tag{2.52}$$

where $O(\Delta_i^r)$ denotes terms on the order of Δ_i^r and higher. Thus, the linear approximation has a leading error of order Δ_i^3.

(II) Quadratic variation for $L_i(x)$

In the case of a quadratic variation, $L_i(x)$ is expressed as,

$$L_i(x) = C_{i0} + C_{i1}(x - x_i) + C_{i2}(x - x_i)^2 \quad , \tag{2.53}$$

where coefficients C_{i0}, C_{i1} and C_{i2} are given as

$$C_{i0} = S_i \quad ,$$

$$C_{i1} = \frac{1}{2\Delta_i}(-S_{i-1} + S_{i+1}) \quad ,$$

and

$$C_{i2} = \frac{1}{2\Delta_i^2}(S_{i-1} - 2S_i + S_{i+1}) \quad ,$$

from the condition that $S(x) = L_i(x)$ at $x = x_{i-1}$, x_i and x_{i+1}.

To evaluate ε by Eq.(2.44), we obtain $D^r L_{i+1}$ $(r > 0)$ by the Taylor series as follows:

$$L_{i+1} = C_{i0} + C_{i1}\Delta_i = S_{i+1} \quad , \tag{2.54}$$

$$DL_{i+1} = (-1) \times (C_{i1} + 2C_{i2}\Delta_i) = -\frac{1}{2\Delta_i}(S_{i-1} - 4S_i + 3S_{i+1}) \quad , \tag{2.55}$$

where S_i and S_{i-1} are given respectively by Eq.(2.48) and the following Eq.(2.56):

$$S_{i-1} = \sum_{p=0}^{\infty} \frac{D^p S_{i+1}}{p!} (2\Delta_i)^p \quad . \tag{2.56}$$

Substituting Eqs.(2.48), (2.56) into Eq.(2.55) using Eq.(2.50), we obtain

$$DL_{i+1} = DS_{i+1} + 2 \sum_{p=0}^{\infty} \frac{D^{p+2} S_{i+1}}{(p+2)!} - \sum_{p=0}^{\infty} \frac{D^{p+2} S_{i+1}}{(p+2)!} (2\Delta_i)^{p+1} \quad . \tag{2.57}$$

Similarly,

$$D^2 L_{i+1} = (-1)^2 \cdot 2C_{i2} = \frac{1}{\Delta_i^{\,2}} (S_{i-1} - 2S_i + S_{i+1})$$

$$= D^2 S_{i+1} - 2 \sum_{p=0}^{\infty} \frac{D^{p+3} S_{i+1}}{(p+3)!} \Delta_i^{\,p+1} + \sum_{p=0}^{\infty} \frac{D^{p+3} S_{i+1}}{(p+3)!} 2^{p+3} \Delta_i^{\,p+1} \quad . \tag{2.58}$$

Also it is evident from Eq.(2.53),

$$D^r L_{i+1} = 0 \quad . \qquad (r > 2) \tag{2.59}$$

Substituting Eqs.(2.54), (2.57) through (2.59) into Eq.(2.44), we obtain

$$\varepsilon\mu = \left[\sum_{p=0}^{\infty} \frac{D^{p+2} S_{i+1}}{(p+2)!} (2\Delta_i)^{p+1} - 2 \sum_{p=0}^{\infty} \frac{D^{p+2} S_{i+1}}{(p+2)!} \Delta_i^{\,p+1} \right]$$

$$\times \left(\frac{1}{2} \Delta_i^{\,2} + \frac{a_i}{3} \Delta_i^{\,3} + \text{-----} \right)$$

$$+ \left[2 \times \sum_{p=0}^{\infty} \frac{D^{p+3} S_{i+1}}{(p+3)!} \Delta_i^{\,p+1} - \sum_{p=0}^{\infty} \frac{D^{p+3} S_{i+1}}{(p+3)!} \cdot 2^{p+3} \Delta_i^{\,p+1} \right]$$

$$\times \left(\frac{1}{6} \Delta_i^{\,3} + \frac{a_i}{8} \Delta_i^{\,4} + \text{-----} \right) \quad ,$$

which is rearranged in ascending series of Δ_i to yield

$$\varepsilon = \frac{1}{9\mu} D^3 S_{i+1} \Delta_i^{\,4} + O(\Delta_i^{\,5}) \quad . \tag{2.60}$$

Thus, the approximation of the quadratic function introduces an error of order $\Delta_i^{\,4}$, and hence it is superior to that of the linear function.

(III) Exponential variation for $L_i(x)$

In the case of an exponential variation, $L_i(x)$ takes the form as

$$L_i(x) = C_{i0} \exp[C_{i1}(x - x_{i+1})] \quad , \tag{2.61}$$

where

$$C_{i0} = S_{i+1}$$

and

$$C_{i1} = -\frac{1}{\Delta_i} \ln\left(\frac{S_i}{S_{i+1}}\right) \quad , \tag{2.62}$$

from the condition of source conservation at $x = x_i$ and x_{i+1}. Applying the Taylor series expansion to $\ln(S_i/S_{i+1})$, we can rewrite Eq.(2.62) using Eq.(2.48) as

$$C_{i1} = -\frac{1}{\Delta_i} \sum_{n=1}^{\infty} \frac{(-1)^{n-1}}{n} \cdot \frac{1}{S_{i+1}^{n}} \left[\sum_{p=0}^{\infty} \frac{D^{p+1} S_{i+1}}{(p+1)!} \Delta_i^{\,p+1} \right]^n \quad . \tag{2.63}$$

To evaluate ε by Eq.(2.44), we obtain $D^r L_{i+1}$ $(r \geqq 0)$ by the Taylor series as follows:

$$L_{i+1} = S_{i+1} \quad , \tag{2.64}$$

and using Eqs.(2.48) and (2.50), we obtain

$$L_{i+1} = - C_{i0}C_{i1}$$

$$= \frac{1}{\Delta_i}\left[(S_i - S_{i+1}) - \frac{(S_i - S_{i+1})^2}{2S_{i+1}} + \frac{(S_i - S_{i+1})^3}{3S_{i+1}^2} - \text{-----} \right]$$

$$= \frac{1}{\Delta_i}\left\{ \sum_{p=0}^{\infty} \frac{D^{p+1}S_{i+1}}{(p+1)!} \Delta_i^{p+1} - \frac{1}{2S_{i+1}}\left[\sum_{p=0}^{\infty} \frac{D^{p+1}S_{i+1}}{(p+1)!} \Delta_i^{p+1} \right]^2 \right.$$

$$\left. + \frac{1}{3S_{i+1}}\left[\sum_{p=0}^{\infty} \frac{D^{p+1}S_{i+1}}{(p+1)!} \Delta_i^{p+1} \right]^3 - \text{-----} \right\} \quad . \tag{2.65}$$

Rearranging Eq.(2.65) in ascending series of Δ_i, we obtain

$$DL_{i+1} = DS_{i+1} + \frac{1}{2}\left[D^2S_{i+1} - \frac{(DS_{i+1})^2}{S_{i+1}} \right] \Delta_i + O(\Delta_i^{\,2}) \quad . \tag{2.66}$$

In much the same way as DL_{i+1}, we obtain

$$D^2L_{i+1} = (-1)^2 C_{i0}C_{i1}^2$$

$$= \{D^2S_{i+1} - (DS_{i+1})^2\} + O(\Delta_i) \quad . \tag{2.67}$$

Since

$$(D^rS_{i+1} - D^rL_{i+1}) \times \sum_{s=0}^{\infty} \frac{a_i^{\,s}}{r!s!(r+s+1)} \Delta_i^{\,r+s+1} \quad ,$$

introduces the minimum order of Δ_i to be > 3 for $r > 2$, irrespective of the order obtained from $(D^rS_{i+1} - D^rL_{i+1})$, furthermore, the minimum order of Δ_i for $r \leqq 2$ is seen to be three; thus, we do not need to evaluate D^rL_{i+1} $(r > 2)$ in order to evaluate the order of the leading error.

Substituting Eqs.(2.64), (2.66) and (2.67) into Eq.(2.44), we obtain

$$\varepsilon = \frac{1}{4\mu}\left[-D^2S_{i+1} + \frac{(DS_{i+1})^2}{S_{i+1}} \right] \Delta_i^{\,3} + O(\Delta_i^{\,4}) \quad . \tag{2.68}$$

Thus, the approximation of the exponential function introduces an error of the order of Δ_i^3, which is the same as that of the linear function.

As discussed in §2.2, exponential approximation for the source distribution is more realistic than the one of a linear function because of exponential attenuation of radiation in shields. If the true source distribution S(x) is expressed as

$$S(x) = \exp[\alpha(x - x_{i+1})] \quad ,$$

we obtain

$$S_{i+1} = S(x_{i+1}) = 1 \quad , \tag{2.69}$$

$$DS_{i+1} = \left.\frac{dS(x)}{dx}\right|_{x=x_{i+1}} = \alpha \quad , \tag{2.70}$$

$$D^2S_{i+1} = \left.\frac{d^2S(x)}{dx^2}\right|_{x=x_{i+1}} = \alpha^2 \quad . \tag{2.71}$$

Substituting Eqs.(2.69) through (2.71) into Eq.(2.68), we obtain

$$\varepsilon = 0 \cdot \Delta_i^3 + O(\Delta_i^4) \quad .$$

On the other hand, substituting Eqs.(2.69) through (2.71) into Eq.(2.52) for linear approximation, we obtain

$$\varepsilon = -\frac{\alpha^2}{12\mu} \cdot \Delta_i^3 + O(\Delta_i^4) \quad .$$

This is the reason why the calculational accuracy of the exponential method in §2.2 is superior to the one of the method based on linear approximation, despite both methods have the leading errors of the same order.

3. Development of PALLAS-XYZ Code

3.1 Description of PALLAS-XYZ Code

The PALLAS-XYZ, a neutron transport code, has been developed for solving the energy and angle dependent integral transport equation with general anisotropic scattering in three-dimensional (x,y,z) geometry. The code has been designed based on a method of direct integration by integrating along a flight path of radiation in the direction of its motion at each discrete ordinate angle. The specific features of this method are:

(1) The radiation flux is calculated at each energy mesh without using the inner iteration method widely used in the S_n transport calculational method for obtaining the angular flux at each energy group.

(2) The scattering calculations are made using directly the differential scattering cross section for neutrons. Thus a Legendre polynomial expansion approximation widely used in the S_n method is not adopted in the calculation of radiation scattering. Consequently, PALLAS-XYZ can always provide positive and physically meaningful angular and scalar fluxes.

(3) Since it does not require use of the average flux in the calculation, PALLAS-XYZ is suitable for application to such problems as violently varying angular and spatial distributions of radiation fluxes.

Due to the enormous amount of mesh points for angular fluxes and sources, it is very hard to store all of these data in a main memory. In order to avoid this difficulty, the following data handling system is employed. In the main memory is stored at a time a block of data of angular fluxes and sources of a certain energy group of all spatial meshes over the (x-y) planes belonging to a certain axial region. The block data in the main memory are then transferred to an auxiliary memory device in the order of the axial region and of the energy mesh. Application of the variable dimensioning scheme to variables of angular flux and source, and of scalar flux is also useful for saving main memory size required for calculations.

The neutron group constants are always referred to from the PALLAS library[58,59)] by designating identification numbers to nuclides of interest given in Table 4.5. Although effective cross sections of single nuclides and some specified mixtures are available from the PALLAS library, they cannot be applied to the nuclides involved in any homogenized materials. In order to answer to this problem, an option is implemented into the code to replace the smoothed cross sections of σ_t and σ_s from the PALLAS library with the effective data of mixtures calculated externally by any proper method such as the RIFF code[56)].

PALLAS calculations are always carried out using the nuclear data taken from the PALLAS library with energy mesh structure by equi-spaced width of 0.05, 0.1, 0.2, 0.4 or 0.8 lethargy. Usually, a 0.1 lethargy width structure is utilized for one-dimensional calculations by the PALLAS-PL, SP code[20)] implemented into the PALLAS-XYZ code for the spectral shape estimation technique described in §2.3. We are planning in the future a code modification for performing a finer one-dimensional spectrum estimation using the library with a 0.05 lethargy structure.
However, a structure of 0.2 or 0.4 lethargy width is preferable in three-dimensional calculations in an energy region above ~1.0 MeV because of a steep gradient in the shape of energy spectrum as compared with 1/E spectrum. The structure of 0.4 lethargy width is recommended in an intermediate energy region and that of 0.8 lethargy width below the intermediate region. As a result of the above recommendation, a series calculation is

needed in practical shielding calculations with a combined structure by 0.2 + 0.4 + 0.8 lethargy widths. Figure 3.1 illustrates how to couple a calculation with a finer equi-lethargy energy structure to one with a coarser structure in the case of a combined 0.2 + 0.4 lethargy structure. First, a PALLAS calculation with a 0.2 lethargy structure is performed up to the fifth energy mesh and all the calculated angular fluxes are temporarily stored in an auxiliary memory device. Then, stored angular fluxes of every other energy mesh are transferred to another memory device to be used for scattering source calculations with 0.4 lethargy structure. As a result, the PALLAS calculation with 0.4 lethargy structure starts at the fourth energy mesh using the angular fluxes obtained from the previous calculation. Thus, a series calculation can be expanded to 0.8 lethargy structure in the same manner as described above.

Figure 3.2 gives a definition of boundaries adopted in three-dimensional (x,y,z) coordinates system. A vacuum boundary condition is always assumed at the top, right and front boundaries. However, either reflective or vacuum conditions can be specified at bottom, left and back boundaries.

The PALLAS-XYZ code uses a built-in angular quadrature set of 56 directional points covering the whole surface of unit sphere, arranged symmetrically with respect to x-, y- and z-axes. Angular variable $\bar{\Omega}$ is represented by $\bar{\Omega}(\omega_p,\phi_{pq})$, where ω_p ($\equiv \cos\theta_p$) and ϕ_{pq} are the cosine of the polar angle and the azimuthal angle, designating a midpoint of its corresponding angular segment. The polar angle mesh is specified by the index p and the azimuthal angle mesh by index q. Assignment of directional points and their corresponding quadrature weights are given in Table 3.1 and their arrangement on a unit spherical surface is illustrated in Fig.3.3.

Table 3.1 Angular Quadratures for PALLAS-XYZ

No.	p 1)	q 2)	ω_p	ϕ_{pq}	Weight
1	1	1	0.99240	0.78450	0.02386
2	1	2	0.99240	2.35620	0.02386
3	1	3	0.99240	-2.35620	0.02386
4	1	4	0.99240	-0.78450	0.02386
5	2	1	0.91174	0.78450	0.22956
6	2	2	0.91174	2.35620	0.22956
7	2	3	0.91174	-2.35620	0.22956
8	2	4	0.91174	-0.78450	0.22956
9	3	1	0.63852	0.31420	0.25152
10	3	2	0.63852	1.09960	0.37727
11	3	3	0.63852	2.04200	0.37727
12	3	4	0.63852	2.82740	0.25152
13	3	5	0.63852	-2.82740	0.25152
14	3	6	0.63852	-2.04200	0.37727
15	3	7	0.63852	-1.09960	0.37727
16	3	8	0.63852	-0.31420	0.25152
17	4	1	0.21918	0.19640	0.17215
18	4	2	0.21918	0.68710	0.25822
19	4	3	0.21918	1.27620	0.25822
20	4	4	0.21918	1.86540	0.25822
21	4	5	0.21918	2.45440	0.25822
22	4	6	0.21918	2.94520	0.17215
23	4	7	0.21918	-2.94520	0.17215
24	4	8	0.21918	-2.45440	0.25822
25	4	9	0.21918	-1.86540	0.25822
26	4	10	0.21918	-1.27620	0.25822
27	4	11	0.21918	-0.68710	0.25822
28	4	12	0.21918	-0.19640	0.17215
29	5	1	-0.21918	0.19640	0.17215
30	5	2	-0.21918	0.68710	0.25822
31	5	3	-0.21918	1.27620	0.25822
32	5	4	-0.21918	1.86540	0.25822
33	5	5	-0.21918	2.45440	0.25822
34	5	6	-0.21918	2.94520	0.17215
35	5	7	-0.21918	-2.94520	0.17215
36	5	8	-0.21918	-2.45440	0.25822
37	5	9	-0.21918	-1.86540	0.25822
38	5	10	-0.21918	-1.27620	0.25822
39	5	11	-0.21918	-0.68710	0.25822
40	5	12	-0.21918	-0.19640	0.17215
41	6	1	-0.63852	0.31420	0.25152
42	6	2	-0.63852	1.09960	0.37727
43	6	3	-0.63852	2.04200	0.37727
44	6	4	-0.63852	2.82740	0.25152
45	6	5	-0.63852	-2.82740	0.25152
46	6	6	-0.63852	-2.04200	0.37727
47	6	7	-0.63852	-1.09960	0.37727
48	6	8	-0.63852	-0.31420	0.25152
49	7	1	-0.91174	0.78450	0.22956
50	7	2	-0.91174	2.35620	0.22956
51	7	3	-0.91174	-2.35620	0.22956
52	7	4	-0.91174	-0.78450	0.22956
53	8	1	-0.99240	0.78450	0.02386
54	8	2	-0.99240	2.35620	0.02386
55	8	3	-0.99240	-2.35620	0.02386
56	8	4	-0.99240	-0.78450	0.02386

1) polar angle index

2) azimuthal angle index

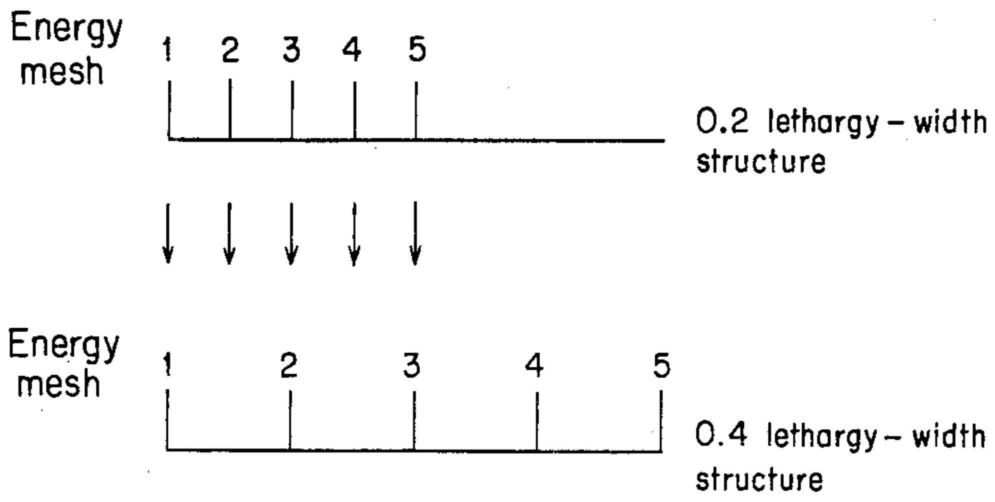

Fig.3.1 Coupling scheme with respect to energy in a series calculation.

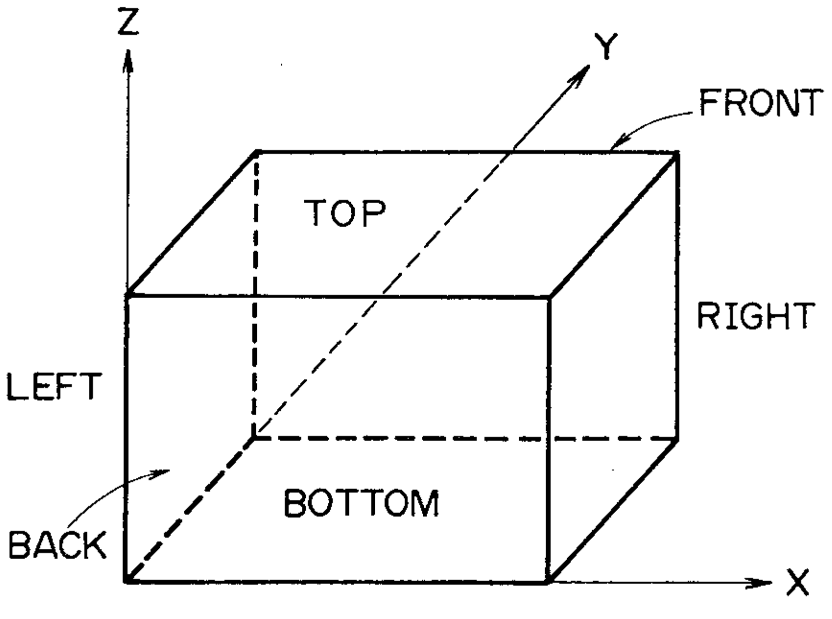

Fig.3.2 Definition of boundaries in (x,y,z) geometry.

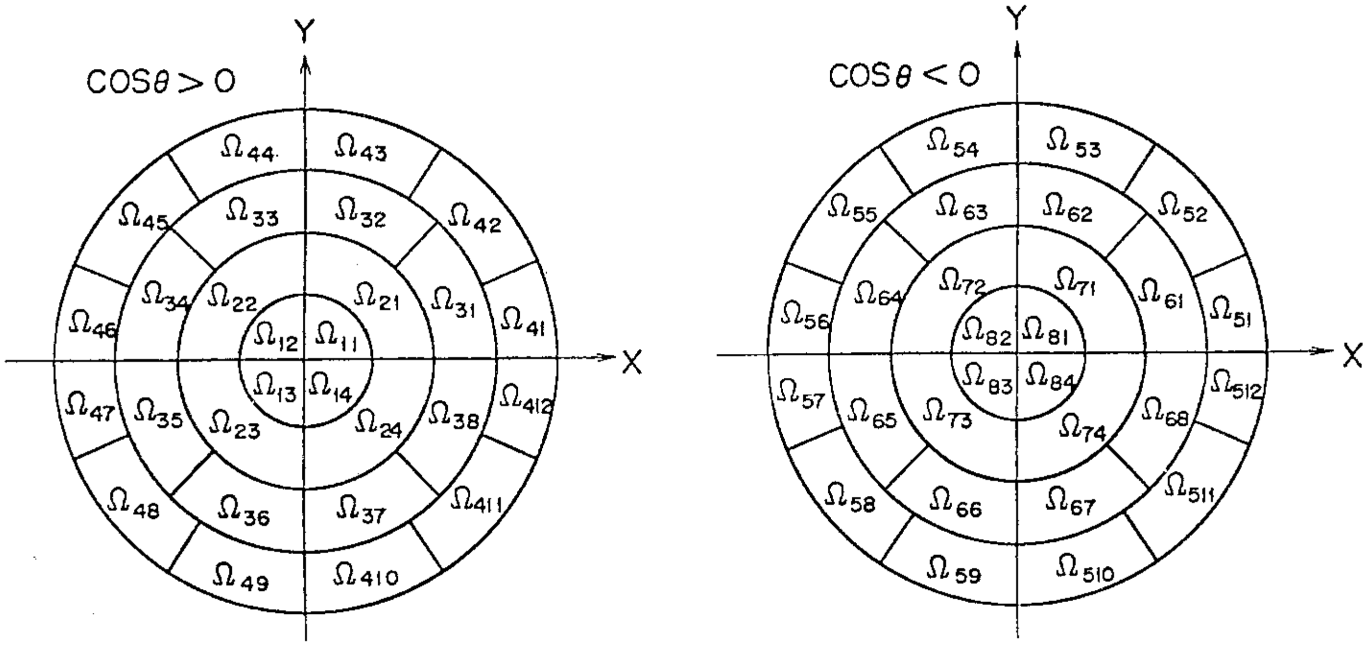

Fig.3.3 Order of angular quadrature mesh adopted in PALLAS-XYZ.

3.2 Structure of PALLAS-XYZ Code

The code is made up using an overlay structure with one BLOCK DATA, one system program, 21 SUBROUTINEs and two FUNCTIONs. Figure 3.4 gives an entire structure map of the code. The structure is mainly divided into two blocks; one is for three-dimensional transport calculations and another for one-dimensional calculations[20)] for obtaining regionwise spectral shape data. A brief description is presented below to explain the functions of the constituent modules.

1) BLOCKD: initialize angular quadrature data, Gaussian quadrature data, etc.
2) MAIN : input number of spatial and angular meshes, with which array sizes of angular flux and source, and of scalar flux are calculated.
3) DTLIST: print all input data read from data cards. DTLIST is a system program at the Japan Atomic Energy Research Institute Computer Center.
4) MAINX : control the main flow of the program.
5) OPEN : define the relationship between the directional point $\overline{\Omega}_{pq}$ $[\equiv \overline{\Omega}(\omega_p,\phi_{pq})]$ and the indexes of the subscripts p and q.
6) TOKYO : read input data from cards, print them, define geometrical assignment such as spatial meshes, material regions etc., calculate source conditions, etc.
7) YOKHAM: calculate for each nuclide, σ_t, σ_s, the elastic scattering angular distribution function $f(E,\mu)$ and slowing down matrix due to inelastic scattering and (n,2n') reactions, etc.
8) LBREAD: read from the PALLAS library, σ_t, σ_s, σ_c, Legendre polynomial coefficients for scattering distribution function and slowing down matrix.

9) ONEWAY: calculate regionwise energy spectra through one-dimensional PALLAS calculations, through which the weighting functions for three-dimensional scattering calculations are determined.

10) PALLAS: control main flow of the one-dimensional energy spectrum calculation.

11) PALTKY: one-dimensional calculation routine which corresponds to TOKYO in the three-dimensional one.

12) PALYKH: one-dimensional routine which corresponds to YOKHAM in the three-dimensional one.

13) YH : define energy meshes for one-dimensional calculation with detailed energy structure.

14) READ : one-dimensional calculation routine which corresponds to LBREAD in the three-dimensional one.

15) PALATM: one-dimensional calculation routine which corresponds to ATAMI in the three-dimensional one described later.

16) PALNGO: one-dimensional calculation routine which corresponds to NAGOYA in the three-dimensional one described later.

17) PSU : define inner boundary meshes on both sides of a material region for one-dimensional calculation.

18) PALPLN: carry out neutron transport calculations within a material region in one-dimensional plane geometry.

19) PALSPR: carry out neutron transport calculations within a material region in one-dimensional spherical geometry.

20) ATAMI: determine integral points and calculate their corresponding weights in scattering integral calculation over azimuthal scattering angle.

21) MISIMA: calculate coordinates $\overline{r}'$ (x',y',z'), just a previous mesh point to the mesh point of interest $\overline{r}$.

22) NAGOYA: carry out neutron scattering integral calculations to obtain angular sources at every spatial mesh within a whole configuration.

23) KYOTO : carry out neutron transport calculations within a material region in three-dimensional (x,y,z) geometry.

24) INTEP : calculate angular fluxes and sources at $\overline{r}'$ (x',y',z') by interpolation scheme.

25) OSAKA : print calculated angular and scalar fluxes, reaction rates, etc. and store them optionally.

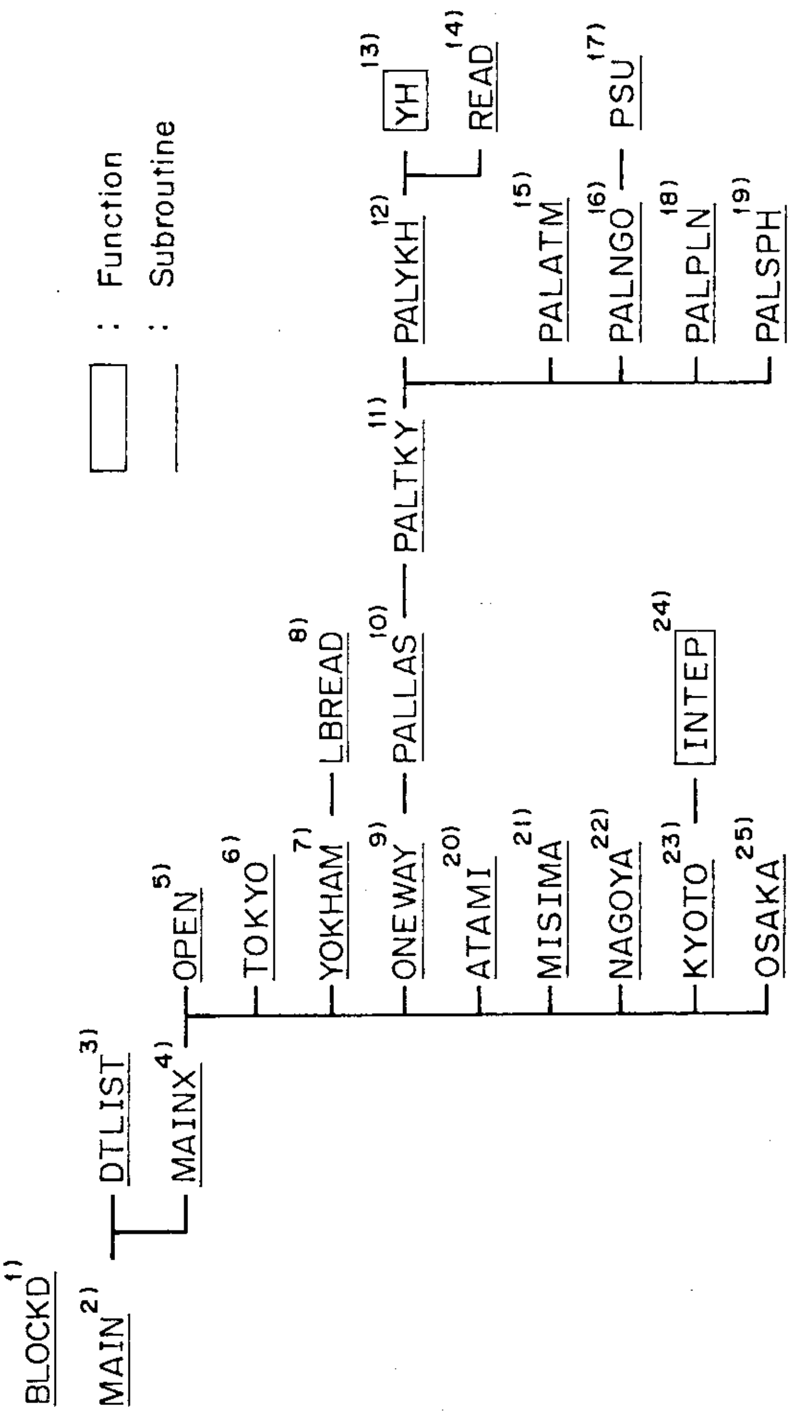

Fig.3.4 Structure map of PALLAS-XYZ.

3.3 Program for Reaction Rate Calculation Using Spline Function

In analyzing a shielding experiment, we often encounter a comparison between experiments and calculations in terms of reaction rate of threshold and/or resonance reactions instead of an energy spectrum. In our code system, a reaction rate calculation is not performed with the PALLAS-XYZ code for reasons of simplicity. Instead it is carried out with a separate code based on the angular fluxes obtained from PALLAS-XYZ calculations. While threshold reaction cross sections abruptly decrease in the vicinity of threshold energy usually above 1.0 MeV, we often observe in the same energy region, a steep gradient in the spectral shape particularly in a problem of neutron deep penetration in heavy materials such as iron. Therefore, partial reaction rate around the threshold energy usually contribute much to the total reaction rate. So if the group averaged responses (reaction cross sections) are not accurately evaluated, they may introduce serious errors in the calculated reaction rate. In order to avoid these errors, it is absolutely necessary to utilize regionwise group averaged responses generated by using the corresponding energy spectra as weighting functions. The responses thus obtained, however, depend on the energy spectra within material regions of interest. Basides, the two-dimensional transport calculations with few energy groups involves numerical errors due to use of few group responses calculated by using one-dimensional spectra.

At present, two dosimetry files 60,61) based on the 620 energy group structures of a SAND-II library 60) are available. The group structures of the 620 groups are so fine that the group averaged responses can be considered to be independent of the weighting functions considered. Collapsing threshold reaction cross sections with abrupt decrease in the vicinity of threshold energy, brings numerical errors into few group responses, hence, new method was presented of reaction rate calculations using responses of the 620 groups. We then established as an auxiliary code of the PALLAS-XYZ, the reaction rate calculation program using the 620 energy groups and the corresponding fine energy spectrum determined by interpolating the PALLAS-XYZ calculated spectrum. Since through use of the PALLAS-XYZ, the energy spectrum per unit energy width is obtained at equi-lethargy spaced energy meshes, a smooth spectrum of 620 groups can be easily calculated by an interpolation scheme based on third-degree natural spline function62).

Third-degree spline functions have been more widely used than those of any other degrees. If the abscissas of the data points are equally spaced, the parameters of the third-degree interpolating natural spline function can be explicitly obtained. Given a set of data $\{(x_1,f(x_1)), (x_2,f(x_2)), \text{-----}, (x_n,f(x_n))\}$ for $x_j = j$ $(j = 1,2,\text{-----},n)$, $f(x)$ $(x_1 \leqq x \leqq x_n)$ can be expressed by

$$f(x) = f(1) + (x-1)d + \sum_{j=1}^{n} c_j (x-j)_+^3 \quad , \tag{3.1}$$

where $z_+^3 = z^3$ $(z \geqq 0)$ and 0 $(z < 0)$. The coefficients d and c_j are to be determined. Table 3.2 gives the values of integer constants α_j and β_j corresponding to each integer $j \geqq 2$ to be used in Eqs.(3.1) and (3.2). The coefficient d is given by

$$\begin{aligned} d &= \{\alpha_2[f(x_n) - f(x_1)] + \alpha_3[f(x_{n-1}) - f(x_1)] + \text{-----} \\ &\qquad + \alpha_n[f(x_2) - f(x_1)]\} / \beta_n \\ &\equiv N / \beta_n \quad . \end{aligned} \tag{3.2}$$

The quantities $\beta_n c_j$ $(j = 1,2,\text{-----},n)$ are then obtained recursively with the formulas

$$\beta_n c_1 = \beta_n (y_2 - y_1) - N \tag{3.3}$$

$$\beta_n c_j = \beta_n (y_{i+1} - y_1) - jN - 2^3\beta_n c_{j-1} - 3^3\beta_n c_{j-2} - \text{------}\, j^3\beta_n c_1$$
$$(j = 2,3,\text{-----},n-1) \tag{3.4}$$

$$\beta_n c_n = - \beta_n c_1 - \beta_n c_2 - \text{------}\, \beta_n c_{n-1} \quad . \tag{3.5}$$

Substituting d and c_j $(j = 1,2,\text{-----},n)$ thus obtained into Eq.(3.1), we obtain an interpolated value f(x) at any point x $(x_1 \leqq x \leqq x_n)$.

While Greville gives a table of α_j and β_j up to $j = 20$$^{62)}$, it was verified that α_j and β_j up to $j = 10$ are sufficient for accurate interpolation based on PALLAS calculated energy spectra. Table 3.3 gives a program list of interpolation calculation in subroutine form for general use.

Table 3.2 Constants for Calculating Third-Degree Interpolating Natural Spline Function for Equally Spaced Arguments

j	α_j	β_j
2	1	1
3	-6	-4
4	24	15
5	-90	-56
6	336	209
7	-1254	-780
8	4680	2911
9	-17466	-10864
10	65184	40545

The table can be continued by means of the following relations (the first of which does not hold for $j = 3$):

$$\alpha_{j+1} = -4\alpha_j - \alpha_{j-1}$$
$$\beta_{j+1} = -4\beta_j - \beta_{j-1}$$
$$\alpha_j = \beta_j - 2\beta_{j-1} + \beta_{j-2}$$

Table 3.3 A Program List of Interpolation Calculation by Third-Degree Natural Spline Function

```
      SUBROUTINE NSPLN3(SN,RR,X,NMAX,SX)
C     THIRD-DEGREE NATURAL SPLINE INTERPOLATION WITH EQUI-SPACED KNOTS
      DIMENSION SN(20),C(20),RR(20),BNC(20),NA(20),NB(20),IR(20)
      DOUBLE PRECISION BNC,XS,NA,NB
      DATA
     1 (NA(I),I=1,17)/0,1,-6,24,-90,336,-1254,4680,-17466,65184,-243270
     2 ,907896,-3388314,12645360,-47193126,176127144,-657315450/,
     4 (NB(I),I=1,17)/0,1,-4,15,-56,209,-780,2911,-10864,40545,-151316
     5 ,564719,-2107560,7865521,-29354524,109552575,-408855776/
C
      HH=RR(2)-RR(1)
      DO 100 I=1,NMAX
      IR(I)=1+(RR(I)-RR(1))/HH
  100 CONTINUE
      XS=0.0
      DO 105 I=2,NMAX
      XS=XS+NA(I)*DBLE(SN(NMAX-I+2)-SN(1))
  105 CONTINUE
      D=XS/NB(NMAX)
      DO 110 I=1,NMAX
      IF(X.LT.RR(I)) GO TO 120
  110 CONTINUE
      NC=NMAX
      GO TO 130
  120 NC=I-1
  130 CONTINUE
      BNC(1)=NB(NMAX)*DBLE(SN(2)-SN(1))-XS
      DO 150 I=2,NC
      IF(I.EQ.NMAX) GO TO 160
      BNC(I)=NB(NMAX)*DBLE(SN(I+1)-SN(1))-I*XS
      DO 150 J=1,I-1
      BNC(I)=BNC(I)-DFLOAT(I+1-J)**3*BNC(J)
  150 CONTINUE
      GO TO 175
  160 BNC(I)=0.0D+0
      DO 170 J=1,NMAX-1
      BNC(I)=BNC(I)-BNC(J)
  170 CONTINUE
  175 CONTINUE
      DO 180 I=1,NC
      C(I)=BNC(I)/NB(NMAX)
  180 CONTINUE
      RX=1.0+(X-RR(1))/HH
      SX=SN(1)+(RX-1.0)*D
      DO 190 I=1,NC
      SX=SX+C(I)*(RX-FLOAT(I))**3
  190 CONTINUE
      RETURN
      END
```

4. Preparation of PALLAS Library[58,59]

4.1 Introduction

Up until the time when the nuclear data library for the PALLAS code was generated, all nuclear data necessary for PALLAS calculations, had to be prepared manually in cards. A large amount of manual data preparation inevitably introduces mistakes and a reduction of data accuracy into the calculation. Further, data preparation tasks are usually very tedious and time-consuming. Therefore, unavailability of the PALLAS nuclear data library was apparently one of the reasons why the PALLAS code had not been proposed for general use in any practical shielding calculations in spite of some of its distinguished features.

In order to solve this problem, a multi-group neutron cross section library for PALLAS was produced in 1977[58] for the first time using a cross section processing code system RADHEAT-V3[53]. The basic neutron cross section data were taken from the ENDF/B-IV libraries. Generation of this library greatly improved the PALLAS calculation method not only in nuclear data handling but also in its calculational accuracy. In the library, the energy structures with equi-spaced lethargy width of 0.1, 0.2, 0.4 and 0.8 lethargies are taken into account for 22 nuclides frequently encountered in practical shielding calculations. Nuclear group constants considered in the library are 1) microscopic smoothed cross sections ($\sigma_t, \sigma_c, \sigma_s$), 2) Legendre polynomial expansion coefficients for differential elastic scattering cross section and 3) scattering matrices due to inelastic scattering and (n,2n') reactions.

Recently, an option for neutron-photon coupling transport calculation was added to the PALLAS code[63]. Besides, some new techniques were implemented in the three-dimensional PALLAS-XYZ code for more accurate and efficient calculation. Therefore, in accordance with the code modification, an overall revision of the PALLAS library was made in 1981[59] using a modified version of the nuclear data processing system NJOY[64] based on the original data from ENDF/B-IV libraries. The reason for changing the processing code from the RADHEAT-V3 to the NJOY is that the JNOY can process both neutron and secondary gamma-ray data from ENDF/B-IV libraries, while the RADHEAT-V3 processes neutron data from ENDF/B-IV but the secondary gamma-ray data must be taken from POPOP4 library[65]. In addition to the four energy structures in the previous library, a structure with 0.05 equi-spaced lethargy width was newly introduced. Furthermore, nine nuclides, including four mixtures (stainless steels, concretes), were added. Because of numerical errors due to interpolation scheme for self-shielding factor table (f-table), a method was newly introduced for estimation of the self-shielding factor, using the RIFF code[56] which calculates self-shielding factors with the calculated ultra-fine group (0.0021 lethargy width) neutron energy spectra in a homogenized infinite medium. The PALLAS library was originally designed to be utilized for all the PALLAS codes of various geometries, so the PALLAS-XYZ code can read in nuclear data from this library, too. The library of the previous version together with the two-dimensional transport code PALLAS-2DCY[51] has been included in the Computer Code Collection (CCC) of the Radiation Shielding Information Center (RSIC) at ORNL and also in the Computer Program Library (CPL) at the NEA Data Bank for its general distribution.

4.2 Energy Mesh Structures and Materials

A neutron energy mesh structure with equi-spaced lethargy width is assumed by the requirement from the fundamental algorithm of the PALLAS code. In addition, the PALLAS code requires fine energy meshes, e.g., 0.1 or 0.2 lethargy width, especially for the energy region above 1.0 MeV, since no use is made of the iterative convergence technique for internal-mesh scattering calculations. Hence, it is obviously unrealistic to carry out neutron transport calculations with fine equi-lethargy structure throughout the energy region from 14 MeV to thermal neutron energy from the standpoint of computer running time. Therefore, the PALLAS library of the revised version includes group constants for five energy mesh structures given in Table 4.1. These structures are represented by midpoints E_i, upper and lower boundaries, E_i^{up} and E_i^{low}, of the i-th energy group defined as

$$E_i = 14.2 \cdot \exp[-\Delta u(i-1)] \quad ,$$

$$E_i^{up} = E_i \cdot \exp(\Delta u/2) \quad ,$$

and

$$E_i^{low} = E_i \cdot \exp(-\Delta u/2) \quad ,$$

where Δu designates equi-spaced lethargy width. Contrary to the neutron energy structure, gamma-ray energy can be assigned arbitrarily depending on the problem to be solved. Thus we define the energy structure for secondary gamma-ray data as presented in Table 4.2.

Table 4.3 gives the list of names and mass numbers of the 27 nuclides and four mixtures included in the library. Material compositions of the four mixtures are presented in Table 4.4. Note that hydrogen is excluded from the composition tables of the two concretes. This is due to the fact that hydrogen cannot be mixed with other nuclides because hydrogen is dealt with separately from other nuclides in neutron scattering calculations with the PALLAS code. Therefore, it is necessary to specify both hydrogen and concrete mixture for a concrete region. Since all fissile and fertile nuclides except for ^{235}U and ^{238}U are not included in the library, one should refer to the library data of ^{235}U and ^{238}U for other fissile and fertile nuclides, respectively.

Table 4.1 Energy Mesh Structures Used in the PALLAS Library

No.	Lethargy width	Energy meshes	Energy range (eV)
1	0.05	100	1.42 + 7*) - 1.00 + 5
2	0.1	172	1.42 + 7 - thermal
3	0.2	88	1.42 + 7 - thermal
4	0.4	45	1.42 + 7 - thermal
5	0.8	23	1.42 + 7 - thermal

*) read as 1.42×10^7

Table 4.2 Gamma-ray Energy Structure

No.	Energy (MeV)	Width*) (MeV)	No.	Energy (MeV)	Width*) (MeV)
1	13.0	3.0	14	0.24	0.08
2	10.0	2.5	15	0.18	0.045
3	8.0	1.5	16	0.15	0.0275
4	7.0	1.0	17	0.125	0.021
5	6.0	1.0	18	0.108	0.0155
6	5.0	1.0	19	0.094	0.0125
7	4.0	1.0	20	0.083	9.5×10^{-3}
8	3.0	1.0	21	0.075	7.5×10^{-3}
9	2.0	0.75	22	0.068	6.5×10^{-3}
10	1.5	0.5	23	0.062	5.0×10^{-3}
11	1.0	0.5	24	0.058	5.0×10^{-3}
12	0.5	0.33	25	0.052	6.0×10^{-3}
13	0.34	0.13			

*) $\Delta E_i = (E_{i+1} - E_{i-1}) / 2.0$

Table 4.3 Nuclides and Mixtures in the PALLAS Library

No.	Nuclide	MAT No. 1)	Mass	No.	Nuclide	MAT No. 1)	Mass
1	H - 1	1269	1.0	17	Cr	1191	52.0
2	H - 2	1120	2.0	18	Mn-55	1197	55.0
3	Li- 6	1271	6.0	19	Fe	1192	55.85
4	Li- 7	1272	7.0	20	Ni	1190	58.71
5	Be- 9	1289	9.0	21	Cu	1295	63.55
6	B -10	1273	10.0	22	Zr	1284	91.22
7	B -11	1160	11.0	23	Mo	1287	95.94
8	C -12	1274	12.0	24	W	* 2)	183.85
9	N -14	1275	14.0	25	Pb	1288	207.2
10	O -16	1276	16.0	26	U-235	1261	235.0
11	F	1277	19.0	27	U-238	1262	238.0
12	Na-23	1156	23.0	28	SUS304		1.0 3)
13	Mg	1280	24.31	29	SUS316		1.0 3)
14	Aℓ-27	1193	27.0	30	O. Conc 4)		1.0 3)
15	Si	1194	28.09	31	H. Conc 5)		1.0 3)
16	Ca	1195	40.08				

1) ENDF/B-IV

2) Natural tungsten {^{182}W(1128)/^{183}W(1129)/^{184}W(1130)/^{186}W(1131) = 0.265/0.145/0.306/0.284}

3) designate macroscopic data

4) ordinary concrete ($\rho = 2.30$)

5) heavy concrete ($\rho = 3.72$)

Table 4.4 Material Composition of Mixtures

(10^{24} atoms/cm^3)

Nuclide	SUS (304)	SUS (316)	ordinary concrete[1] ($\rho = 2.30$)	heavy concrete[1] ($\rho = 3.72$)
O			4.393-2 [2]	4.390-2
Si	2.127-3	2.127-3	1.936-2	3.935-3
Ca			2.374-3	2.278-3
Cr	1.741-2	1.558-2		
Mn	1.734-3	1.734-3		
Fe	5.787-2	5.574-2	6.791-4	2.360-2
Ni	8.112-3	9.734-3		
Mo		1.242-3		

1) hydrogen (^1H) is excluded

2) read as 4.393×10^{-2}

4.3 Nuclear Constants

4.3.1 Microscopic Smooth Cross Sections

Group averaged smooth data include total, capture and total elastic scattering cross sections in the library. The weighting functions used in group averaging calculations are the combined spectrum composing of fission spectrum with fission temperature of 1.35×10^6 eV, 1/E spectrum and a Maxwellian spectrum with thermal temperature of 0.0253 eV. The 1/E spectrum is coupled to the fission spectrum at neutron energy of 4×10^5 eV and to the Maxwellian spectrum at 0.394 eV. Microscopic infinite dilution cross sections were calculated by the NJOY code with the above weighting function. Effective cross sections were then evaluated by multiplying the infinite dilution data with the corresponding self-shielding factors calculated using the RIFF code56). Koyama pointed out the necessity of some corrections on Maxwellian averaged thermal neutron group constants66), so the thermal group constants obtained by NJOY were replaced with the evaluated data by Koyama66).

4.3.2 Scattering Matrix

While the scattering matrix for S_n calculation involves ealstic, inelastic scattering and (n,2n') reactions representing its anisotropy by Legendre expansion, the scattering matrix for PALLAS calculation involves only inelastic scattering and (n,2n') reactions, assuming isotropic scattering in the laboratory system. Thus, the scattering matrix in the PALLAS library was determined with the NJOY code as the P_0 component of the matrix excluding elastic scattering reaction, based on the basic nuclear data from ENDF/B-IV libraries. On the other hand, anisotropy of elastic scattering is accurately described with the angular distribution function calculated from the Legendre polynomial coefficient.

4.3.3 Angular Distribution Function for Elastic Scattering

The library involves at every energy mesh the Legendre polynomial expansion coefficients with which the angular distribution function is calculated. The only exception is for hydrogen which needs no coefficient because an isotropic scattering in the center-of-mass system is assumed. The coefficients at every energy mesh are obtained by linearly interpolating the coefficients taken from the ENDF/B-IV libraries up to the 20'th term. Validity of the interpolated values are certified by confirming that the integration

$$I = \int_{1}^{-1} \left[\sum_{\ell=0}^{\ell_{max}} \frac{2\ell+1}{2} \cdot f_\ell \cdot P_\ell(\mu) \right] d\mu \qquad (4.1)$$

takes values

$$I = 1.000 \begin{array}{l} + 0.01 \\ - 0.001 \end{array} \quad ,$$

where f_ℓ, $P_\ell(\mu)$ and ℓ_{max} denote ℓ'th order Legendre coefficient, Legendre polynomial and maximum number of terms, respectively.

4.3.4 Secondary Gamma-Ray Production Data

Secondary gamma-ray production matrices were generated with the NJOY code, based on the secondary gamma-ray production reaction cross sections and the secondary gamma-ray production probability in the form of either yield or cross section, both from ENDF/B-IV libraries. Secondary gamma-ray production reactions considered are radiative capture, inelastic scattering, (n,2n') and fission reactions of neutrons.

4.4 Structure of the PALLAS Library

The library consists of separate group constant data blocks with equi-lethargy spaced energy structures of $\Delta u = 0.05$, 0.1, 0.2, 0.4 and 0.8 lethargy width. So, when one wants to refer to PALLAS library data, one must specify both the energy structure and the nuclide of interest, by designating the specially prepared identification number (ID No.) shown in Table 4.5 consisting of four digits having the following meanings:

i) $\underline{X}\ \underline{YY}\ \underline{Z}$ for nuclide

$\underline{X}$(I1) : identification of equi-spaced lethargy width structure

1 for $\Delta u = 0.1$ lethargy

2 for $\Delta u = 0.2$ lethargy

4 for $\Delta u = 0.4$ lethargy

5 for $\Delta u = 0.05$ lethargy

8 for $\Delta u = 0.8$ lethargy

$\underline{YY}$(I2) : atomic number

When the atomic number is less than 10, the former digit is assigned 0

$\underline{Z}$(I1) : end digit of mass number

Zero is always assigned to a natural element

ii) $\underline{X}\ \underline{YYY}$ for mixture

X(I1) : same as that for nuclide

YYY(I3) : arbitrary number by three digits indicating a mixture

Group constants are stored in magnetic tapes and disk memories according to the BCD format with record size and block size of 80 and 3200 bite, respectively. They are arranged for each nuclide or mixture using the following format:

Record #1　　4H****

Symbol indicating the first card of the data block

Record #2　　IDNO, NAME(I), I = 1, 12　　(I6, 12A4)

IDNO : identification number of the nuclide or the mixture　　(c.f. Table 4.5)

NAME : name of the nuclide or the mixture

Record #3　　NGN, NGG, JAM, JBM, JFMU, LP, JPM　　(7I6)

NGN : number of neutron energy mesh points

NGG : number of secondary gamma-ray energy mesh points

JAM : upper limit of the energy mesh number for zero slowing down probability

JBM : upper limit of the energy mesh number below which neither inelastic nor (n,2n') scattering reaction occurs

JFMU : lower limit of the energy mesh number above which anisotropy of elastic scattering should be taken into account

LP : maximum number of terms for Legendre polynomials

JPM : ≡ NGN

Record #4　　SIG(I), I = 1, NGN　　(6E12.5)

SIG : microscopic total cross section (σ_t)

Record #5　　SIGC(I), I = 1, NGN　　(6E12.5)

SIGC : microscopic radiative capture cross section (σ_c)

Record #6　　SIGS(I), I = 1, NGN　　(6E12.5)

SIGS : microscopic total elastic scattering cross section ($\sigma_{e\ell}$)

Record #7　　(CL(I,J), J = 1, LP), I = 1, JFMU　　[JFMU > 0]　　(6E12.5)

CL : Legendre polynomial coefficient

Record #8 (SCT(J,I), I = 1, JAM), J = 1, JBM [JAM > 0 and JBM > 0] (6E12.5)

SCT : scattering matrix

Record #9 (SCG(I,J), I = 1, NGG), J = 1, JPM [JPM > 0] (6E12.5)

SCG : secondary gamma-ray production matrix

Table 4.5 List of Identification Numbers

No.	Nuclide	Identification Number				
		Δu = 0.05	Δu = 0.1	Δu = 0.2	Δu = 0.4	Δu = 0.8
1	H - 1	5011	1011	2011	4011	8011
2	H - 2	5012	1012	2012	4012	8012
3	Li- 6	5036	1036	2036	4036	8036
4	Li- 7	5037	1037	2037	4037	8037
5	Be- 9	5039	1039	2039	4039	8039
6	B -10	5050	1050	2050	4050	8050
7	B -11	5051	1051	2051	4051	8051
8	C -12	5062	1062	2062	4062	8062
9	N -14	5074	1074	2074	4074	8074
10	O -16	5086	1086	2086	4086	8086
11	F	5090	1090	2090	4090	8090
12	Na-23	5113	1113	2113	4113	8113
13	Mg	5120	1120	2120	4120	8120
14	Aℓ-27	5137	1137	2137	4137	8137
15	Si	5140	1140	2140	4140	8140
16	Ca	5200	1200	2200	4200	8200
17	Cr	5240	1240	2240	4240	8240
18	Mn-55	5255	1255	2255	4255	8255
19	Fe	5260	1260	2260	4260	8260
20	Ni	5280	1280	2280	4280	8280
21	Cu	5290	1290	2290	4290	8290
22	Zr	5400	1400	2400	4400	8400
23	Mo	5420	1420	2420	4420	8420
24	W	5740	1740	2740	4740	8740
25	Pb	5820	1820	2820	4820	8820
26	U-235	5925	1925	2925	4925	8925
27	U-238	5928	1928	2928	4928	8928
28	SUS(304)	5500	1500	2500	4500	8500
29	SUS(316)	5510	1510	2510	4510	8510
30	Ordinary Concrete	5520	1520	2520	4520	8520
31	Heavy Concrete	5530	1530	2530	4530	8530

4.5 Nuclear Data Processing Code System NJOY-PALLAS

Based on the general purpose code system NJOY$^{64)}$, a group constant processing code system NJOY-PALLAS was formulated to generate group constants for the PALLAS library. The NJOY-PALLAS is divided into two parts. The first part is to generate infinite dilution cross sections and the second part is, i) to generate effective cross sections based on the infinite dilution ones and ii) to store them in accordance with the structure of the PALLAS library. Figure 4.1 gives a flow chart of this system. Description is given below about the functions of each calculational step using the symbols (A), (B), (C), (D) and (E) in Fig.4.1:

1) the NJOY code calculates infinite dilution cross sections referring to the basic nuclear data from ENDF/B-IV libraries (A) and store them in the file (B).
2) the PREPALIB code arranges infinite dilution data taken from the file (B), identification numbers and Legendre coefficients according to the PALLAS library structure, yielding infinite dilution data file (C). So the group constants of mixtures are not included in the file (C). PREPALIB also calculates Legendre coefficients at the specified energy meshes.
3) the RIFF code calculates self-shielding factors at T = 300°K of all nuclides and mixtures of interest, and stores them in the file (D).
4) the SELFS codes calculates effective cross sections by multiplying infinite dilution cross sections from the file (C) with the corresponding self-shielding factors from the file (D).

   The effective cross section is stored in the file (E) following the same structure as the infinite dilution cross section library (C).

Thus, we can finally obtain both the infinite dilution and effective cross section libraries, using the NJOY-PALLAS code system.

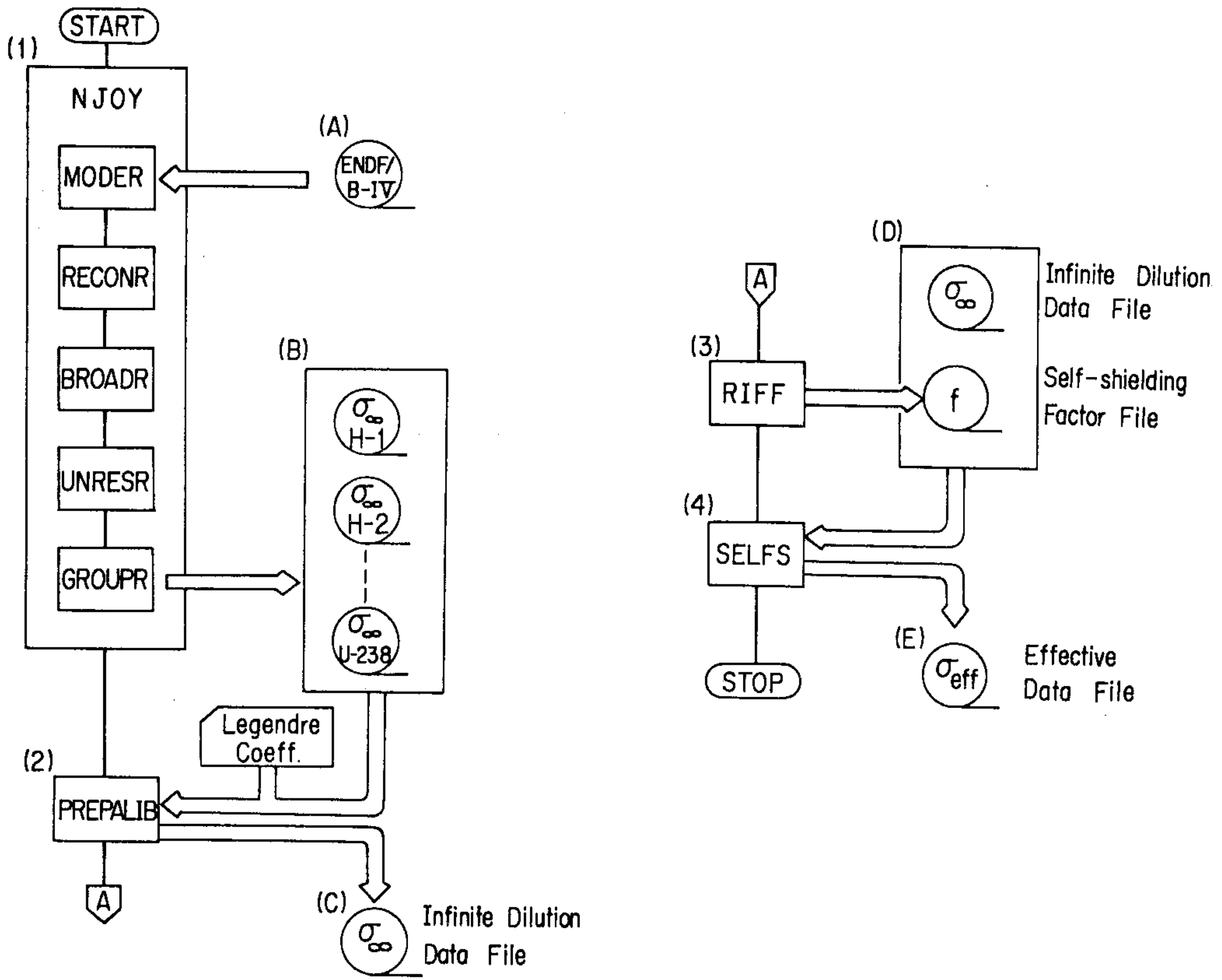

Fig.4.1 Flow chart of library data processing code system NJOY-PALLAS.

Part-II Benchmark Calculations and Analyses of Real Problems with Three-Dimensional PALLAS-XYZ Code

5. Calculation of PCA Benchmark Experiment[44)]

5.1 Description of Experimental Facility

A Pressure Vessel Wall Benchmark Facility was established at the Pool Critical Assembly (PCA) of ORNL to test and validate reactor physics calculations in a simple geometry simulating a commercial power reactor. Knowledge of the reactor core source and the neutron flux and spectrum at locations inside and outside the core was essential to qualify this facility as a reference benchmark field. Hence, an extensive experimental program was performed to provide highly accurate and precise measurement data throughout the facility.

The PCA Benchmark Facility consists of the PCA reactor core of 60-× 38-× 40-cm rectangular geometry and the ex-core components that are used to mock up pressure vessel surveillance configurations for light water reactors (LWRs). These components are: the thermal shield (TS) made of a 6-cm-thick stainless steel slab; the pressure vessel simulator (PVS) of 22.5-cm-thick steel; and the simulated reactor cavity [void box (VB) in PCA of 30.5-cm-thick void]. The whole configuration immersed in pool water is represented in Fig.5.1. Dosimetry integral and differential experiments were performed in two different PCA configurations, X/Y = 8/7 and 12/13. Here, X/Y refers to the water gaps (in cm) from the core edge to the thermal shield/thermal shield to pressre vessel.

Since the whole experimental configuration can be accurately expressed in three-dimensional (x,y,z) geometry and its size is not so large as to neglect neutron leakage from the outer boundary, the PCA experiment is appropriate for verifying three-dimensional neutron transport calculations. Besides, in order to assess state-of-the-art neutronics methodology relative to reactor surveillance, the USNRC conducted a computational Blind Test based on the PCA experiment, in which we participated with the PALLAS-XYZ calculation. Hence, it is possible to compare our calculation with other transport calculations by using discrete ordinates and the Monte Carlo methods, as well as with measurements.

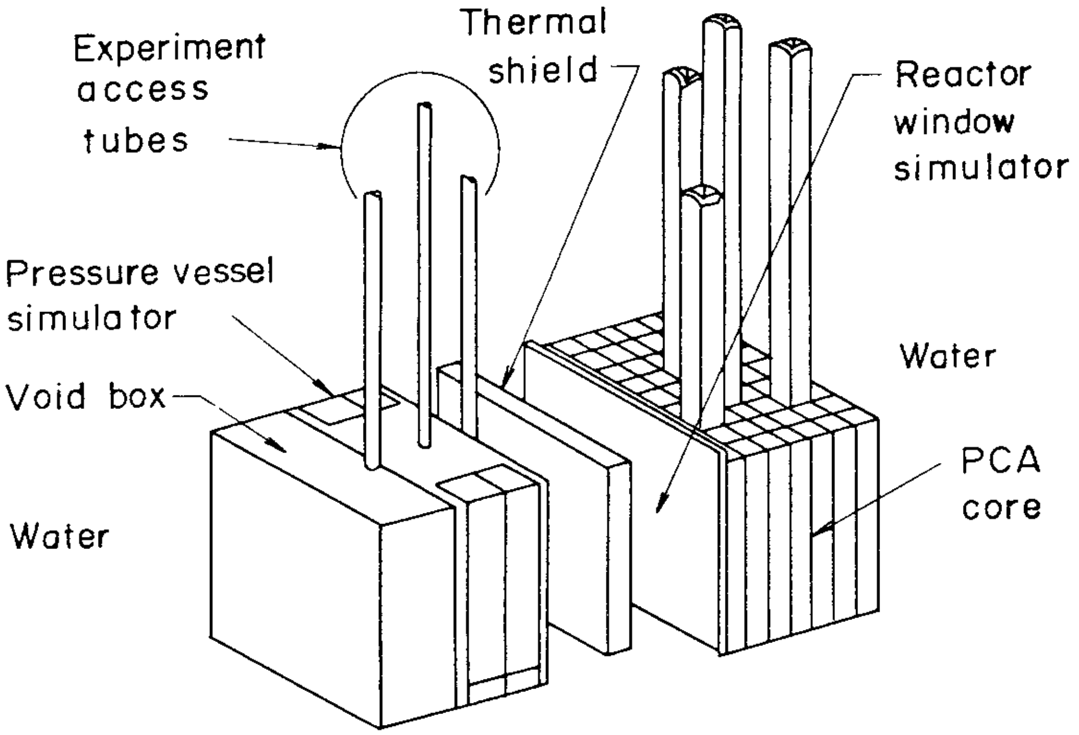

Fig.5.1 Experimental setup of the PCA experiment.

5.2 Calculation with the PALLAS-XYZ Code

The calculational model is given in Fig.5.2. Here, a one-eighth configuration of the actual experimental setup was taken for the calculation because of symmetrical conditions with respect to x, y and z axes, while a vacuum boundary condition was employed for the outermost boundary. The one-dimensional transport calculation in spherical geometry for spectral shape estimation was performed along the horizontal direction of Fig.5.1, along which the experimental configuration extends. Detector points A1 through A8 in the PCA (8/7) and PCA (12/13) configurations are given in Fig.5.3, as the distance from front surface of the aluminum window. The material compositions used in the calculation are given in Table 5.1. Group constants were taken from the PALLAS library58), generated by using the RADHEAT-V3 code system53) with a spectral weighting function of fission + 1/E, based on the original cross section data from the ENDF/B-IV files.

The calculation was carried out with 21 energy meshes above 78 keV as listed in Table 5.2: 14 energy meshes with 0.2 lethargy intervals were used in the energy region 1.06 MeV $\leq E \leq$ 14.2 MeV and 7 energy meshes with 0.4 lethargy intervals for 63 keV $\leq E <$ 1.06 MeV. The bottom energy mesh of 64 keV was employed on the basis of the fact that the neutron fluence above 0.1 MeV plays the most important role in reactor surveillance.
The calculation was of the fixed source type, with the relative power distribution within the PCA core represented by

$$S(x,y,z) = S(x,z) \times S(y)$$

so that it can well express source distribution partially depressed due to insertion of safety and regulating rods. In Table 5.3 are given the source distributions determined on the basis of measurement of the power distribution 67), in which the source normalization was made so that the total neutron sources generated per second within the core were 1.0, that is,

$$8 \times \int_{0.0}^{19.2} dx \int_{0}^{20.25} dz\ S(x,z) \int_{0}^{30.0} dy\ S(y) = 1.0 \quad .$$

Furthermore, all fissions were assumed to be thermal neutron fissions. Therefore, the energy distribution was represented by the Watt fission spectrum model 52). Fractional spectrum as a function of energy mesh is listed in Table 5.4. Spatial mesh assignment is presented in Table 5.5, in which the number of meshes is given in each x-, y- and z-directional material regions together with the thickness and equal mesh interval. Spatial mesh intervals of 2.5 to 6.0 cm were employed in material regions along the z-axis, while 3.75 to 10.0 cm were used along the other axes. Since our interest is mainly forcused on neutron transport calculation along the z-axis, it may be allowed to employ a rather large interval, such as 10.0 cm, at the outer water layer surrounding the experimental configuration.

Table 5.1 PCA Blind Test Material Compositions

(10^{24} atoms/cm^3)

	PCA Core	Aℓ Window	Thermal Shield	Pressure Vessel	Water
H	4.048E-2*)				6.674E-2
C				9.815E-4	3.337E-2
O	2.339E-2				
Aℓ	2.024E-2	6.024E-2			
Mn				5.150E-4	
Fe			8.486E-2	8.372E-2	

*) read as 4.048×10^{-2}

Table 5.2 Energy Group Structure for PALLAS-XYZ Calculation

Group No.	Upper Boundary (MeV)		Group No.	Upper Boundary (MeV)
1	1.569E+1*)		12	1.739E+0
2	1.285E+1		13	1.424E+0
3	1.052E+1		14	1.166E+0
4	8.613E+0		15	9.543E-1
5	7.052E+0		16	7.070E-1
6	5.773E+0		17	4.739E-1
7	4.727E+0		18	3.177E-1
8	3.870E+0		19	2.129E-1
9	3.168E+0		20	1.427E-1
10	2.594E+0		21	9.568E-2
11	2.124E+0			6.414E-2

*) read as 1.569×10^{1}

Table 5.3 Relative Power Distribution S(x,z) and S(y) within the PCA Core

S (x,z)						
z Mesh (cm)	x Mesh (cm)					
	0.0	3.84	7.68	11.52	15.36	19.20
0.0	2.55	2.35	2.66	1.48	1.70	1.55
4.05	2.40	0.97	0.00	0.74	1.59	1.46
8.10	2.32	1.29	0.00	0.00	1.55	1.46
12.15	1.85	1.54	1.79	1.18	1.22	1.12
16.20	1.56	1.19	1.42	0.93	1.05	0.95
20.25	1.41	1.12	1.28	0.92	0.96	0.86

y Mesh (cm)	S (y)
0.0	0.982
3.75	0.968
7.50	0.925
11.25	0.863
15.00	0.778
18.75	0.670
22.50	0.570
26.25	0.488
30.00	0.550

Table 5.4 Source Neutron Spectrum Calculated from Watt's Formula

Group No.	Spectrum (MeV^{-1})	Group No.	Spectrum (MeV^{-1})
1	3.398E - 5	12	2.872E - 1
2	2.685E - 4	13	3.188E - 1
3	1.396E - 3	14	3.405E - 1
4	5.173E - 3	15	3.524E - 1
5	1.458E - 2	16	3.516E - 1
6	3.298E - 2	17	3.281E - 1
7	6.242E - 2	18	2.931E - 1
8	1.024E - 1	19	2.543E - 1
9	1.496E - 1	20	2.164E - 1
10	1.994E - 1	21	1.818E - 1
11	2.466E - 1		

Table 5.5 Spatial Mesh Assignment for the PCA (8/7) and PCA (12/13) Configurations

Region	X-axis			Y-axis			Z-axis		
	Meshes	Thickness (cm)	Interval (cm)	Meshes	Thickness (cm)	Interval (cm)	Meshes	Thickness (cm)	Interval (cm)
1	6	19.2	3.84	9	30.0	3.75	6	20.25	4.05
2	3	9.28	4.64	3	20.0	10.0	2	2.5	2.5
3	3	20.0	10.0				4	8.4	2.8
							(5	12.3	3.08)*
4							3	5.9	2.95
5							4	6.7	2.23
							(5	12.8	3.2)*
6							5	11.25	2.81
7							5	11.25	2.81
8							6	30.0	6.0
9							5	20.0	5.0

*) data for the PCA (12/13)

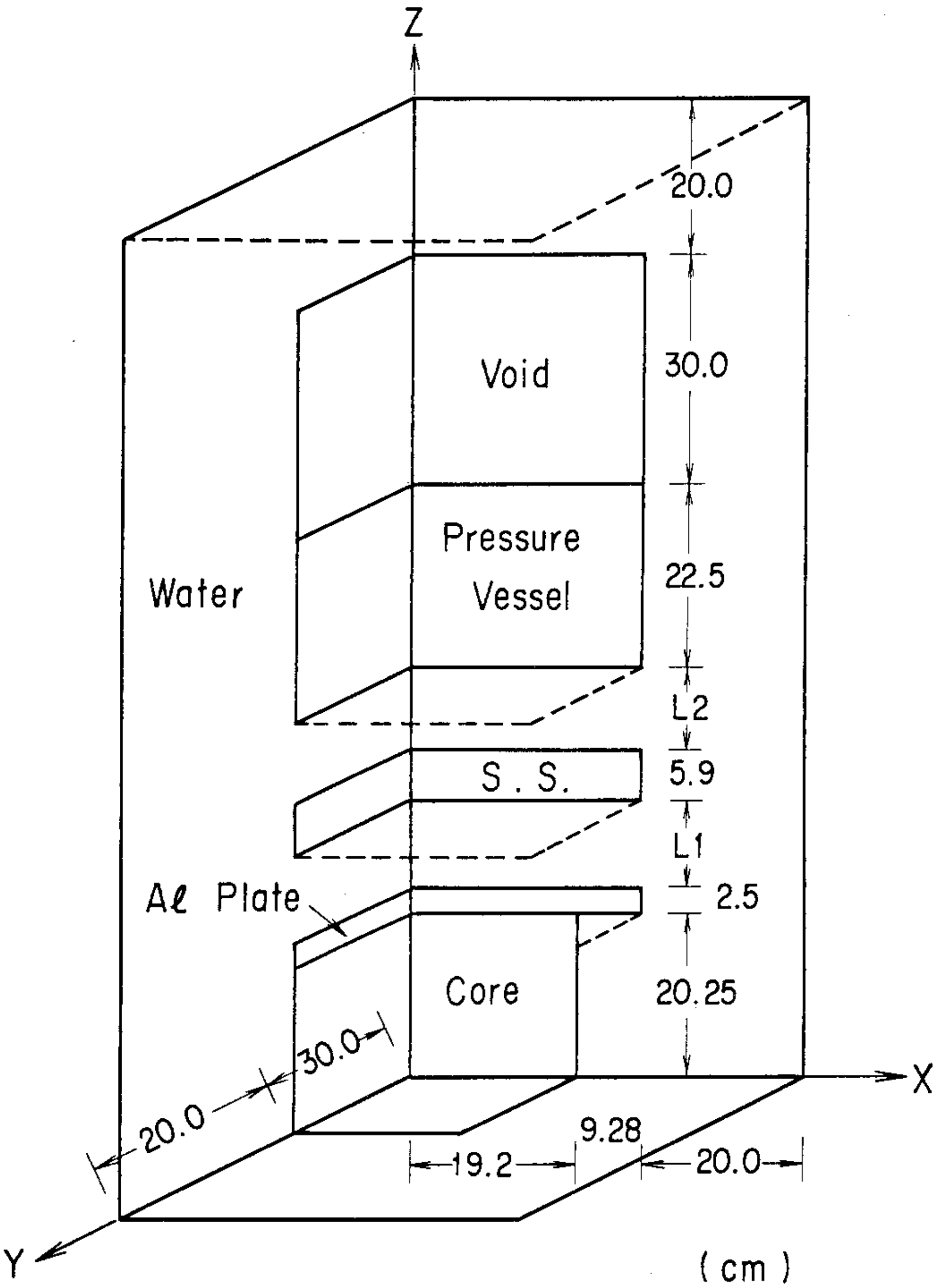

Fig.5.2 Calculational model of the PCA experiment for PALLAS-XYZ. PCA(8/7) and PCA(12/13) configurations are respectively defined by designating L1/L2 as 8.4/6.7 and 12.3/12.8.

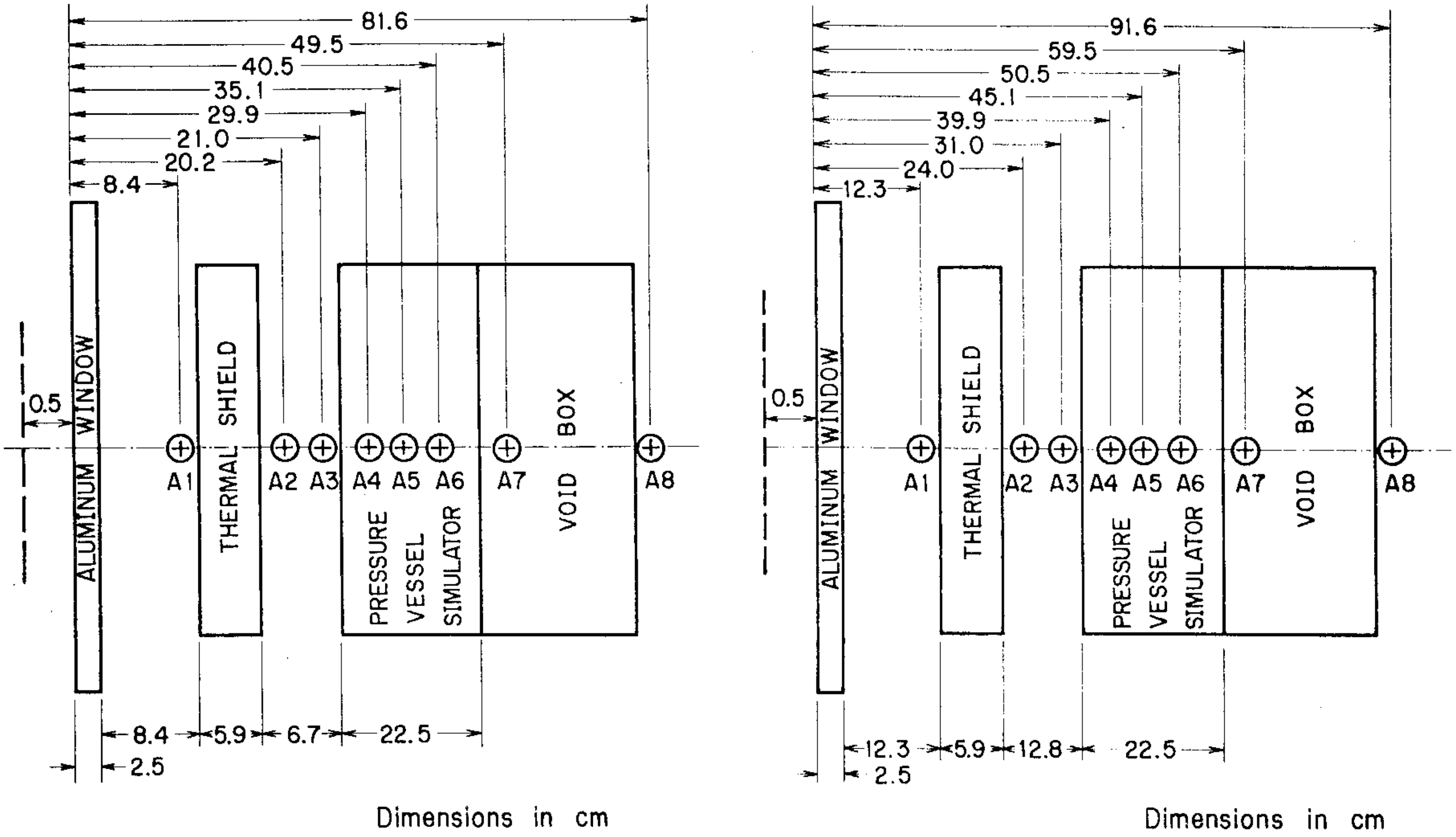

Fig.5.3 Two-dimensional expressions of the PCA(8/7)(left) and PCA(12/13)(right) configurations, where A1 through A8 designate detector points.

5.3 Calculational Results and Discussion

The calculated group fluxes $\phi(u)\Delta u$ at the detector points A1 through A8 for the PCA (8/7) and PCA (12/13) configurations are given in Tables 5.6 and 5.7, respectively. Calculation of reaction rates from the calculated group flux introduces uncertainties from the reaction cross sections and collapsing procedures to the specified group structure. Thus, a more accurate assessment of the calculational accuracy can be obtained through comparison of measured and calculated equivalent fission fluxes defined as 44)

$$\phi_{fi} = \frac{\int_0^\infty \sigma_i(E)\phi(E)dE}{\int_0^\infty \chi_{25}(E)\sigma_i(E)dE} , \qquad (5.1)$$

where

$\sigma_i(E)$ = appropriate reaction cross section,

$\phi(E)$ = neutron energy spectrum of interest at a certain PCA location,

$\chi_{25}(E)$ = ^{235}U fission spectrum normalized to an integral of unity.

The calculated group fluxes participating in the PCA Blind Test, including ours, were converted to present the C/E ratios of some reaction rates for the equivalent fission fluxes, using the reaction cross sections of the ENDF/B-IV file, except for the ^{103}Rh(n,n') reaction in which a EURATOM cross section file was used 44). In Tables 5.8 and 5.9 are listed the C/E ratios of our calculations for the PCA (8/7) and PCA (12/13) configurations, respectively, together with those of other participants for comparison with each other.

As is evident from Tables 5.8 and 5.9, the PALLAS-XYZ calculation underestimates the experiment by a reasonable amount at almost all the detector points. Besides, the underestimate for the PCA (8/7) is found to be slightly larger than the underestimate for the PCA (12/13). The cause for this may be that the direct integration scheme with relatively coarse energy meshes of 0.2 or 0.4 lethargy interval, cannot sufficiently follow such a steep gradient as in the energy spectrum above 1.0 MeV. Underestimate for the PCA (8/7) is sharper than that for the PCA (12/13) because of a steeper gradient in the spectrum due to thinner water gaps than those for the latter. Further, the PALLAS-XYZ calculation also has a tendency to slightly increase the amount of underestimate with the z directional distance because of rather rough angular quadrature mesh, especially the first polar angular one.

In spite of all these errors, the PALLAS-XYZ calculation provides a good agreement with the experiment within a 30% error. In comparison with other calculations, most of which were carried out with S_n discrete ordinate codes in two-dimensional (x,y) geometry with help of leakage correction, the PALLAS-XYZ calculation is certified to be as accurate or more accurate than other calculations.

The same procedure was used to calculate the iron damage exposure parameter dpa (displacement per atom) using the iron displacement cross section taken from Ref.68, and to obtain integral fluxes greater than 1.0 MeV and greater than 0.1 MeV. They are listed in Tables 5.10 and 5.11 for the PCA (8/7) and PCA (12/13) configurations, respectively. The PALLAS calculation is seen to underestimate the experiment within its standard deviation for the PCA (8/7), while an overestimate with reasonable amount is obtained for the PCA (12/13). The difference between calculations for the two configurations is caused by the same factor already discussed just above. As in the case of reaction rate calculation, the PALLAS-XYZ can calculate the integral parameters (dpa, integral fluxes) above neutron energy of 0.1 MeV within the experimental error, the accuracy of which is seen to be equal or better than the accuracy of other calculations.

The calculations required 1 hour, 45 min, 48 s CPU time on the FACOM M200 using main memory size of about 1900 kbite.

In summary, through investigation of the calculational accuracy of reaction rates of threshold reaction, dpa and the integral neutron fluxes greater than 0.1 MeV and greater than 1.0 MeV, it was certified that the PALLAS-XYZ can calculate without any leakage correction the neutron field greater than 0.1 MeV within experimental error.

Table 5.6 Group Flux Calculated with PALLAS-XYZ for the PCA (8/7) Configuration

Group No.	Location							
	A1	A2	A3	A4	A5	A6	A7	A8
1	1.4053E - 9*	1.7240E - 10	1.5570E - 10	3.6679E - 11	1.5194E - 11	6.1851E - 12	2.1512E - 12	2.7403E - 13
2	9.0502E - 9	1.1372E - 9	1.0225E - 9	2.5114E - 10	1.0646E - 10	4.3641E - 11	1.4888E - 11	2.4970E - 12
3	3.9099E - 8	4.5594E - 9	4.0946E - 9	9.1631E - 10	3.7159E - 10	1.4620E - 10	4.8993E - 11	9.0713E - 12
4	1.0610E - 7	1.1064E - 8	9.8670E - 9	2.0448E - 9	7.9248E - 10	2.9835E - 10	9.6240E - 11	1.8855E - 11
5	2.4843E - 7	2.4257E - 8	2.1584E - 8	4.2023E - 9	1.5462E - 9	5.4918E - 10	1.6894E - 10	3.7112E - 11
6	4.1932E - 7	3.7177E - 8	3.2861E - 8	6.1635E - 9	2.1900E - 9	7.5586E - 10	2.2053E - 10	4.9849E - 11
7	5.8000E - 7	4.8824E - 8	4.2800E - 8	8.1206E - 9	2.8683E - 9	9.7728E - 10	2.7350E - 10	6.0842E - 11
8	5.7361E - 7	4.6916E - 8	4.0547E - 8	8.7396E - 9	3.2925E - 9	1.2035E - 9	3.3409E - 10	5.9413E - 11
9	1.1999E - 6	1.0042E - 7	8.7218E - 8	1.6227E - 8	5.8620E - 9	2.0369E - 9	5.5601E - 10	1.2270E - 10
10	1.3035E - 6	1.2585E - 7	1.0960E - 8	2.7660E - 8	1.0679E - 8	3.8880E - 9	1.0320E - 9	1.6896E - 10
11	1.1047E - 6	1.1226E - 7	9.7657E - 8	3.2235E - 8	1.3880E - 8	5.5605E - 9	1.4446E - 9	1.7740E - 10
12	1.1802E - 6	1.2155E - 7	1.0586E - 7	3.6591E - 8	1.6747E - 8	7.0334E - 9	1.8089E - 9	2.1284E - 10
13	1.0429E - 6	1.1473E - 7	9.9584E - 8	4.5713E - 8	2.2849E - 8	1.0195E - 8	2.6925E - 9	2.3514E - 10
14	9.4883E - 7	1.1311E - 7	9.7640E - 8	5.7139E - 8	3.2878E - 8	1.6560E - 8	4.5464E - 9	2.7500E - 10
15	1.3687E - 6	1.6165E - 7	1.3994E - 7	7.6725E - 8	4.6635E - 8	2.4873E - 8	6.7173E - 9	4.1784E - 10
16	1.6068E - 6	2.0946E - 7	1.8295E - 7	1.7835E - 7	1.2704E - 7	7.7187E - 8	2.2346E - 8	7.9176E - 10
17	9.9736E - 7	1.2716E - 7	1.1142E - 7	1.0644E - 7	7.9176E - 8	4.9387E - 8	1.4518E - 8	5.1958E - 10
18	1.0608E - 6	1.4190E - 7	1.2334E - 7	1.1311E - 7	9.2039E - 8	6.2521E - 8	2.1816E - 8	6.4074E - 10
19	9.2307E - 7	1.2557E - 7	1.0820E - 7	6.9158E - 8	5.5236E - 8	3.6783E - 8	1.0023E - 8	5.7333E - 10
20	8.1100E - 7	1.1253E - 7	9.7117E - 8	1.0481E - 7	8.4980E - 8	5.6002E - 8	1.6426E - 8	5.2086E - 10
21	7.2949E - 7	1.0234E - 7	8.8347E - 8	6.3517E - 8	5.1404E - 8	3.3526E - 8	8.6628E - 9	4.8126E - 10

*) read as 1.4053×10^{-9}

(n/cm^2)

Table 5.7 Group Flux Calculated with PALLAS-XYZ for the PCA (12/13) Configuration

Group No.	Location							
	A1	A2	A3	A4	A5	A6	A7	A8
1	7.9270E－10*	1.0783E－10	4.7756E－11	1.2636E－11	5.2338E－12	2.0491E－12	6.5976E－13	5.9805E－14
2	4.9949E－9	6.8409E－10	2.9074E－10	7.9307E－11	3.3603E－11	1.3534E－11	4.4990E－12	8.3775E－13
3	2.1391E－8	2.7328E－9	1.1500E－9	2.8077E－10	1.1370E－10	4.4020E－11	1.4441E－11	2.9490E－12
4	5.5953E－8	6.4846E－9	2.5762E－9	5.7835E－10	2.2408E－10	8.3360E－11	2.6645E－11	5.9434E－12
5	1.2987E－7	1.4142E－8	5.4725E－9	1.1447E－9	4.2214E－10	1.4891E－10	4.5978E－11	1.1506E－11
6	2.1050E－7	2.1162E－8	7.6998E－9	1.5598E－9	5.6088E－10	1.9473E－10	5.8171E－11	1.5225E－11
7	2.7879E－7	2.6806E－8	9.0243E－9	1.8766E－9	6.7853E－10	2.3555E－10	6.8101E－11	1.7746E－11
8	2.5552E－7	2.4604E－8	7.4300E－9	1.8316E－9	7.1719E－10	2.7093E－10	7.8085E－11	1.6290E－11
9	5.5757E－7	5.2119E－8	1.5904E－8	3.2260E－9	1.2039E－9	4.3107E－10	1.2167E－10	3.1366E－11
10	6.1807E－7	6.5187E－8	1.9234E－8	5.3305E－9	2.1276E－9	7.9752E－10	2.1790E－10	4.0255E－11
11	5.1177E－7	5.7275E－8	1.6078E－8	6.0237E－9	2.6956E－9	1.1137E－9	2.9821E－10	4.0379E－11
12	5.4331E－7	6.1401E－8	1.7109E－8	6.6911E－9	3.1910E－9	1.3840E－9	3.6541E－10	4.7208E－11
13	4.8071E－7	5.7664E－8	1.5373E－8	8.1933E－9	4.2684E－9	1.9659E－9	5.3518E－10	5.0331E－11
14	4.3553E－7	5.6173E－8	1.4519E－8	1.0091E－8	6.0540E－9	3.1421E－9	8.8591E－10	5.7221E－11
15	6.2608E－7	7.9721E－8	2.0821E－8	1.3528E－8	8.5932E－9	4.7250E－9	1.3172E－9	8.6674E－11
16	7.4346E－7	1.0225E－7	2.7001E－8	3.1110E－8	2.3132E－8	1.4459E－8	4.2682E－9	1.5917E－10
17	4.5254E－7	6.1783E－8	1.6336E－8	1.8525E－8	1.4332E－8	9.1815E－9	2.7821E－9	1.0430E－10
18	4.8251E－7	6.8688E－8	1.7568E－8	1.9621E－8	1.6557E－8	1.1520E－8	4.1066E－9	1.2865E－10
19	4.1616E－7	6.0849E－8	1.4602E－8	1.1962E－8	9.9181E－9	6.7647E－9	1.8823E－9	1.1447E－10
20	3.7411E－7	5.4111E－8	1.3761E－8	1.8043E－8	1.5168E－8	1.0232E－8	3.0676E－9	1.0408E－10
21	3.2309E－7	4.9456E－8	1.1767E－8	1.0892E－8	9.1471E－9	6.1074E－9	1.6105E－9	9.5749E－11

*) read as 7.9270×10^{-10}

(n/cm^2)

Table 5.8 C/E Ratios of Reaction Rates Based on Equivalent Fission Fluxes for the PCA (8/7) Configuration

Code*	Location				Location			
	A3M**	A4	A5	A6	A3M**	A4	A5	A6
	^{237}Np (n,f)				^{238}U (n,f)			
PAL3	0.86	0.92	0.93	0.90		0.77	0.73	0.67
C1	0.79	0.76	0.73	0.68		0.74	0.70	0.62
C2	1.03	1.11	1.08	1.01		1.02	0.97	0.89
C3	0.94	1.05	1.05	1.03		0.96	0.93	0.88
C4	1.03	0.75	0.75	0.73		0.77	0.77	0.74
C5	0.76	0.68	0.66	0.58		0.66	0.70	0.62
C6	0.88	0.90	0.87	0.84		0.77	0.69	0.61
C7	0.76	0.78	0.75	0.71		0.73	0.64	0.57
C8	0.83	0.80	0.79	0.73		0.82	0.80	0.76
C9	0.85	0.88	0.84	0.78		0.86	0.81	0.75
C10	1.16	1.12	1.07	0.98		1.11	1.06	0.98
C11	0.86	0.88	0.85	0.81		0.81	0.76	0.70

	^{103}Rh (n,n')				^{58}Ni (n,p)			
PAL3		0.92	0.89	0.87	1.05	0.81	0.78	0.79
C1		0.81	0.78	0.73	1.05	0.82	0.77	0.70
C2		1.19	1.14	1.09	1.20	1.15	1.09	1.06
C3		1.12	1.11	1.10	1.10	1.09	1.05	1.05
C4		0.84	0.82	0.82	0.92	0.92	0.89	0.90
C5		0.73	0.70	0.62	0.96	0.70	0.81	0.78
C6		0.94	0.91	0.88	1.06	0.86	0.76	0.70
C7		0.83	0.79	0.76	0.85	0.82	0.69	0.62
C8		0.88	0.85	0.81	1.06	0.93	0.88	0.85
C9		0.95	0.90	0.85	1.00	0.98	0.94	0.92
C10		1.21	1.13	1.05	1.38	1.26	1.19	1.14
C11		0.95	0.90	0.88	1.07	0.93	0.87	0.86

	^{115}In (n,n')				^{27}Aℓ (n,α)			
PAL3		0.88	0.82	0.77	0.95	0.78	0.79	0.83
C1		0.82	0.76	0.68	0.99	0.80	0.75	0.70
C2		1.15	1.07	0.99	1.17	1.15	1.10	1.10
C3		1.09	1.04	0.99	1.12	1.17	1.16	1.21
C4		0.85	0.82	0.80	0.88	0.95	0.89	0.87
C5		0.75	0.76	0.69	0.95	0.86	0.82	0.82
C6		0.88	0.79	0.73	1.14	0.96	0.84	0.80
C7		0.82	0.73	0.67	0.83	0.84	0.65	0.57
C8		0.90	0.86	0.82	0.98	0.84	0.74	0.66
C9		0.95	0.88	0.81	0.98	1.04	1.02	1.06
C10		1.22	1.14	1.04	1.42	1.37	1.30	1.28
C11		0.92	0.85	0.81	1.11	0.90	0.82	0.78

*) Code PAL3 indicates the calculation with PALLAS-XYZ, while C2 and C7 means the ones with ANISN and other codes with DOT or TWOTRAN in (x,y) geometry with leakage corrections.

**) Location A3M is 0.8 cm closer to the core than location A3.

Table 5.9 C/E Ratios of Reaction Rates Based on Equivalent Fission Fluxes for the PCA (12/13)

Code*	Location					Location				
	A1	A3M**	A4	A5	A6	A1	A3M*	A4	A5	A6
	^{237}Np (n,f)					^{238}U (n,f)				
PAL3	0.98	0.98	1.06	1.09	1.09			0.84	0.80	0.77
C1	0.81	0.82	0.74	0.71	0.70			0.72	0.67	0.64
C2	1.01	1.15	1.17	1.14	1.09			1.07	1.01	0.94
C3	0.92	1.05	1.15	1.14	1.11			1.05	1.01	0.96
C4	1.04	0.82	0.85	0.85	0.83			0.86	0.85	0.83
C5	0.79	0.72	0.77	0.73	0.67			0.75	0.71	0.66
C6	0.87	0.85	0.83	0.82	0.81			0.71	0.65	0.60
C7	0.75	0.80	0.72	0.71	0.70			0.62	0.57	0.52
C8	0.88	0.95	0.81	0.80	0.75			0.81	0.79	0.75
C9	0.77	0.74	0.83	0.77	0.83			0.89	0.84	0.94
C10	0.83	0.95	0.94	0.91	0.85			0.90	0.86	0.82
C11	0.87	0.90	0.89	0.86	0.83			0.82	0.76	0.72
	^{103}Rh (n,n')					^{58}Ni (n,p)				
PAL3	1.13	1.03	1.06	1.06	1.05	1.00	0.97	0.87	0.84	0.87
C1	0.96	0.89	0.80	0.77	0.75	0.97	1.00	0.79	0.73	0.73
C2	1.19	1.27	1.27	1.24	1.18	1.18	1.36	1.17	1.12	1.12
C3	1.08	1.15	1.23	1.22	1.19	1.07	1.27	1.17	1.14	1.15
C4	1.24	0.91	0.95	0.95	0.94	1.19	0.99	0.97	0.96	1.00
C5	0.93	0.80	0.84	0.81	0.74	0.93	0.89	0.86	0.82	0.82
C6	1.04	0.94	0.88	0.87	0.85	1.08	1.07	0.79	0.71	0.69
C7	0.89	0.88	0.76	0.75	0.73	0.87	0.96	0.65	0.58	0.55
C8	1.05	1.05	0.90	0.88	0.84	1.06	1.16	0.92	0.87	0.84
C9	0.92	0.84	0.93	0.88	0.94	0.91	0.98	1.05	0.99	1.16
C10	0.98	1.04	1.02	1.00	0.94	0.98	1.15	1.03	0.99	1.01
C11	1.03	0.99	0.96	0.93	0.91	1.03	1.12	0.93	0.87	0.88
	^{115}In (n,n')					^{27}Aℓ (n,α)				
PAL3	1.06	1.04	1.00	0.97	0.96	0.89	0.86	0.82	0.81	0.82
C1	0.92	0.93	0.82	0.77	0.76	0.91	0.95	0.78	0.73	0.71
C2	1.14	1.31	1.24	1.18	1.14	1.13	1.31	1.15	1.11	1.11
C3	1.03	1.17	1.21	1.18	1.16	1.07	1.35	1.26	1.27	1.29
C4	1.18	0.93	0.97	0.97	0.97	1.07	0.95	0.95	0.91	0.89
C5	0.89	0.83	0.86	0.82	0.77	0.91	0.89	0.86	0.84	0.84
C6	1.00	0.97	0.83	0.78	0.75	1.15	1.16	0.88	0.81	0.77
C7	0.85	0.91	0.74	0.70	0.67	0.84	0.96	0.56	0.48	0.45
C8	1.01	1.09	0.92	0.90	0.89	0.96	0.97	0.80	0.70	0.61
C9	0.87	0.88	0.99	0.94	1.02	0.86	1.25	1.24	0.83	1.31
C10	0.95	1.08	1.03	0.99	0.96	0.97	1.20	1.12	1.11	1.13
C11	0.99	1.03	0.95	0.90	0.88	1.07	1.13	0.92	0.83	0.78

*) Code PAL3 indicates the calculation with PALLAS-XYZ, while C2 and C7 mean the ones with ANISN, C9 with Monte Carlo code McBEND and other codes with DOT or TWOTRAN in (x,y) geometry with leakage corrections.

**) Location A3M is closer to the core than location A3.

Table 5.10 C/E Ratios of Integral Parameters Based on Equivalent Fission Fluxes for the PCA (8/7) Configuration

Code*	Location			Location			Location		
	A4	A5	A6	A4	A5	A6	A4	A5	A6
	Flux(E ≧ 0.1 MeV)			Flux(E ≧ 1.0 MeV)			DPA**		
PAL3	0.92	0.92	0.92	0.91	0.85	0.80	0.90	0.90	0.89
C1	0.75	0.73	0.70	0.80	0.75	0.68	0.77	0.73	0.69
C2	1.15	1.11	1.08	1.16	1.07	0.99	1.10	1.03	0.97
C3	1.05	1.03	1.03	1.10	1.05	1.01	1.05	1.01	0.99
C4	0.80	0.80	0.80	0.81	0.78	0.77	0.81	0.80	0.78
C5	0.45	0.36	0.29	0.75	0.74	0.67	0.58	0.51	0.41
C6	0.95	0.93	0.92	0.87	0.78	0.72	0.89	0.84	0.81
C7	0.76	0.73	0.72	0.81	0.73	0.67	0.76	0.70	0.67
C8	0.82	0.79	0.75	0.90	0.87	0.85	0.84	0.80	0.75
C9	0.93	0.90	0.85	0.94	0.87	0.80	0.93	0.88	0.83
C10	0.90	0.86	0.82	0.91	0.83	0.79	0.91	0.80	0.83

*) Same as those in Table 5.8.

**) Displacement per atom.

Table 5.11 C/E Ratios of Integral Parameters Based on Equivalent Fission Fluxes for the PCA (12/13) Configuration

Code*	Location					Location					Location				
	A1	A3	A4	A5	A6	A1	A3	A4	A5	A6	A1	A3	A4	A5	A6
	Flux(E ≧ 0.1 MeV)					Flux(E ≧ 1.0 MeV)					Displacements per Atom				
PAL3	1.03	0.97	1.14	1.08	1.18	1.08	0.97	1.04	1.00	0.99	1.05	0.95	1.07	1.10	1.13
C1	0.87	0.78	0.76	0.73	0.72	0.89	0.82	0.80	0.76	0.75	1.11	1.00	0.77	0.74	0.73
C2	1.07	1.12	1.25	1.23	1.19	1.13	1.18	1.25	1.19	1.15	1.48	1.56	1.19	1.14	1.10
C3	0.97	1.02	1.17	1.14	1.12	1.03	1.08	1.23	1.20	1.19	1.13	1.18	1.17	1.13	1.10
C4	1.12	0.83	0.91	0.92	0.92	1.15	0.82	0.93	0.93	0.94	1.13	0.83	0.91	0.91	0.92
C5	0.82	0.69	0.81	0.78	0.72	0.87	0.73	0.83	0.79	0.75	0.91	0.79	0.81	0.77	0.73
C6	0.91	0.83	0.91	0.90	0.90	0.97	0.86	0.83	0.78	0.75	1.10	0.99	0.84	0.82	0.81
C7	0.79	0.78	0.74	0.73	0.73	0.83	0.81	0.74	0.71	0.68	0.94	0.92	0.71	0.69	0.68
C8	0.94	0.93	0.85	0.82	0.78	0.99	0.97	0.92	0.91	0.91	1.42	1.37	0.86	0.84	0.80
C9	0.81	0.68	0.84	0.81	0.84	0.87	0.77	0.95	0.91	0.97	0.83	0.75	0.87	0.81	0.85
C10	0.90	0.85	0.93	0.90	0.87	0.96	0.91	0.93	0.88	0.86	1.20	1.10	0.93	0.90	0.88

*) Same as those in Table 5.9.

6. Calculation of Annular Duct Neutron Streaming Experiment[40)]

6.1 Description of Experimental Configuration

Problem-II is based on an experiment of neutron streaming through an annular duct made of steel (SS-41), performed at a swimming pool-type reactor JRR-4 at JAERI[28)]. The experimental arrangement consists of the JRR-4 core of 40.5- × 34.4- × 60.0-cm rectangular geometry, a graphite reflector surrounding the core in the horizontal direction, a core tank made of aluminum and the annular duct of 150-cm-length in the axial direction consisting of annular layers of water and void in the radial direction. The whole configuration was immersed in pool water. The duct was positioned so that its front surface was 20 cm apart from the core tank, with the duct axis 60 cm upward from the core midplane intersecting at right angle the horizontal axis of the core. The whole experimental configuration simplified for calculation is presented in Fig.6.1, which was modeled as Fig.6.2 in (x,y,z) geometry for PALLAS-XYZ calculations.

It is apparent from this configuration that the neutron flux at the duct mouth shows radial distribution which is asymmetric with respect to the duct axis. If one wants to apply a transport calculation in two-dimensional (r,z) geometry to this problem, the calculation is forced to be carried out based on symmetric boundary fluxes at the duct mouth obtained by averaging the asymmetric distribution with respect to the duct axis, which may yield erroneous results. Therefore, application of a three-dimensional transport calculation is essential in order to take such asymmetric distribution exactly into consideration.

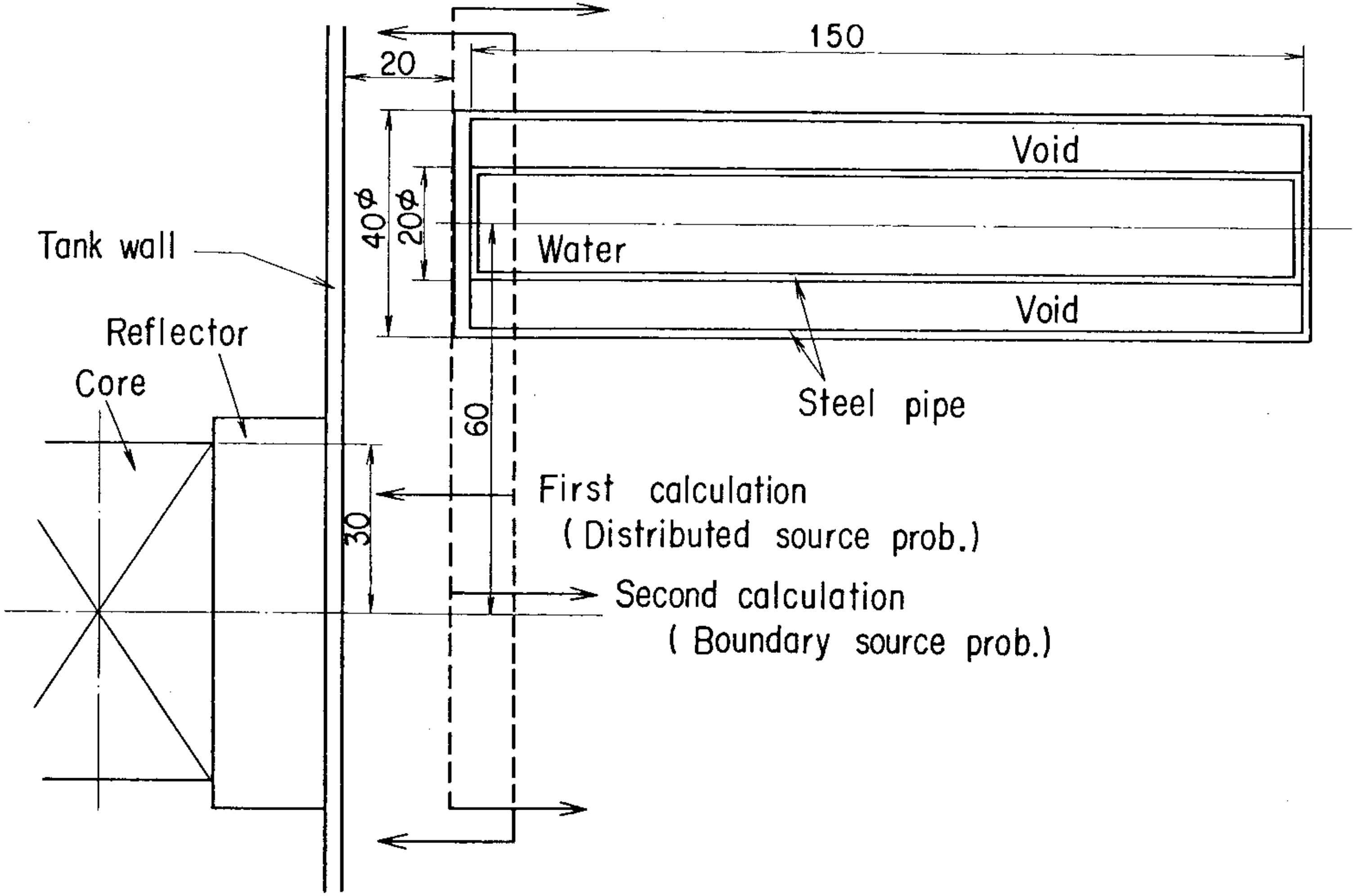

Fig.6.1 Simplified configulation of the annular duct streaming experiment. Dimensions are in cm.

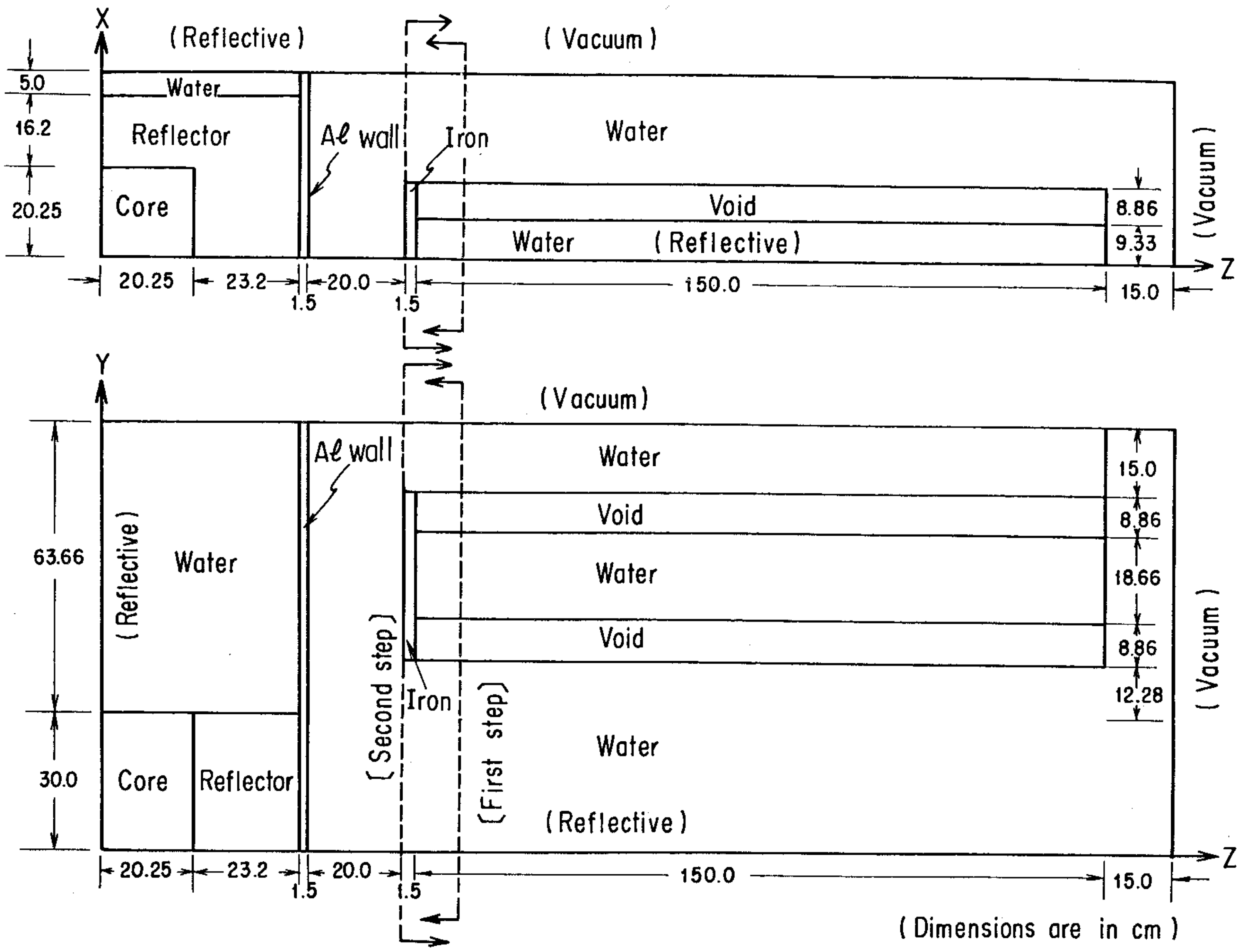

(Dimensions are in cm)

Fig.6.2 Calculational model of the annular duct streaming experiment for PALLAS-XYZ.

6.2 The Calculational Method

As depicted in Fig.6.2, the z-axis coincides with the horizontal axis of the reactor core, parallel to the annular duct axis. The annular duct was modeled by a rectangular duct so that the cross sectional area of the void region could be preserved. Because of symmetrical conditions with respect to x, y and z axes, a one-eighth configuration of the actual one was employed for the present calculation, while a vacuum boundary condition was set for the outermost boundary.

To obtain the reaction rate distribution along the duct axis in detail, the calculation was divided into two parts on space. As shown in Fig.6.2, the first calculation was performed for the region consisting of the core, reflector, core tank and the front part of the annular duct where void was filled with water, then the second calculation for the region of the annular duct immersed in water. Whereas the first calculation was of the distributed source type, the second calculation was of the boundary flux type. The material compositions used in the calculation are listed in Table 6.1.

The calculation was carried out using 56 angular points with 7 energy meshes above 1.92 MeV for estimation of the ^{58}Ni(n,p) reaction rate. As presented in Table 6.2, 3 energy meshes with 0.2 lethargy intervals were used in the energy region $9.52\ \mathrm{MeV} \leqq E \leqq 14.2\ \mathrm{MeV}$ and 4 energy meshes with 0.4 lethargy intervals for $1.92\ \mathrm{MeV} \leqq E < 9.52\ \mathrm{MeV}$. In the first calculation, the distributed source information is represented as

$$S(x,y,z,E) = S(x,z) \times S(y) \times S(E) \quad , \tag{6.1}$$

where spatial distributions S(x,z) and S(y) are listed in Table 6.3 with a normalization of 7.6×10^{10} neutrons generation per second within the core, where S(E), the fractional source spectrum, by the Watt fission model[52)] is given in Table 6.4. Spatial mesh assignments for the first and the second cases are presented in Tables 6.5 and 6.6, respectively. To examine spatial mesh effect on calculational results, a calculation with coarser spatial meshes was carried out by the spatial mesh assignments also included in Tables 6.5 and 6.6.

Table 6.1 Material Compositions Used in the Calculation

(10^{24} atoms/cm^3)

Nuclide	Material Region			
	JRR-4 Core	Reflector	Water	Core Tank
H	4.577E - 2*	1.638E - 3	6.674E - 2	
C		7.341E - 2	3.337E - 2	
O	2.291E - 2			
Aℓ	1.842E - 2			6.025E - 2

*) read as 4.577×10^{-2}

Table 6.2 Energy Group Structure for Analysis of the JRR-4 Experiment

Group No.	Energy Mesh (MeV)	Group No.	Energy Mesh (MeV)
1	14.2	5	4.28
2	11.6	6	2.87
3	9.52	7	1.92
4	6.38		

Table 6.3 Relative Power Distribution S(x,z) and S(y) within the JRR-4 Core

S (x,z)								
z Mesh (cm)	x Mesh (cm)							
	0.0	4.67	9.33	9.33*	13.76	18.19	18.19*	20.77
0.0	1.50	1.46	1.36	1.36	1.14	0.88	0.88	0.76
4.05	1.46	1.46	1.36	1.36	1.14	0.88	0.88	0.76
8.10	1.36	1.36	1.36	1.36	1.14	0.88	0.88	0.76
12.15	1.18	1.18	1.18	1.18	1.14	0.88	0.88	0.76
16.20	0.95	0.95	0.95	0.95	0.95	0.88	0.88	0.76
20.25	0.76	0.76	0.76	0.76	0.76	0.76	0.76	0.76

*) required to assign the same mesh at the boundary of material region

y Mesh (cm)	S (y)
0.0	1.50
4.29	1.48
8.57	1.38
12.86	1.24
17.14	1.02
21.43	0.86
25.71	0.73
30.00	0.67

Table 6.4 Source Neutron Spectrum Calculated from Watt's Formula

Group No.	Spectrum (MeV^{-1})	Group No.	Spectrum (MeV^{-1})
1	3.398E - 5*	5	6.242E - 2
2	2.685E - 4	6	1.496E - 1
3	1.396E - 3	7	2.466E - 1
4	1.458E - 2		

*) read as 3.398×10^{-5}

Table 6.5 Spatial Mesh Assignment for the First Calculation of the Neutron Duct Streaming Experiment

Region	x-Direction			y-Direction			z-Direction		
	Meshes	Thickness (cm)	Interval (cm)	Meshes	Thickness (cm)	Interval (cm)	Meshes	Thickness (cm)	Interval (cm)
1	3	9.33	4.67	8	30.0	4.29	6	20.25	4.05
2	3	8.86	4.43	4	12.28	4.09	7	23.2	3.87
				(3	12.28	6.14)*	(5	23.2	5.80)*
3	2	2.58	2.58	3	8.86	4.43	2	1.5	1.50
4	5	16.2	4.05	5	18.66	4.67	6	20.0	4.00
	(4	16.2	5.40)*	(4	18.66	6.22)*	(5	20.0	5.00)*
5	2	5.0	5.00	3	8.86	4.43	4	10.0	3.33
							(3	10.0	5.00)*
6				3	15.0	7.50			

*) Assigned data in parenthesis are for a calculation with coarser spatial meshes.

Table 6.6 Spatial Mesh Assignment for the Second Calculation of the Neutron Duct Streaming Experiment

Region	x-Direction			y-Direction			z-Direction		
	Meshes	Thickness (cm)	Interval (cm)	Meshes	Thickness (cm)	Interval (cm)	Meshes	Thickness (cm)	Interval (cm)
1	3	9.33	4.67	8	30.0	4.29	2	1.5	1.50
2	3	8.86	4.43	4	12.28	4.09	6	30.0	6.00
				(3	12.28	6.14)*	(5	30.0	7.50)*
3	2	2.58	2.58	3	8.86	4.43	8	40.0	5.71
							7	40.0	6.67
4	5	16.2	4.05	5	18.66	4.67	8	40.0	5.71
				(4	18.66	6.22)*	(7	40.0	6.67)*
5	2	5.0	5.00	3	8.86	4.43	8	40.0	5.71
							(6	40.0	8.00)*
6				3	15.0	7.50	3	15.0	7.50
							(2	10.0	10.00)*

*) Assigned data in parenthesis are for a calculation with coarser spatial meshes.

6.3 Calculational Results and Discussion

The ^{58}Ni(n,p) reaction rate distribution calculated with the PALLAS-XYZ code was compared with that of the experiment and also with that of the three-dimensional S_n code ENSEMBLE, as shown in Fig.6.2. The S_n calculation was made with 4 energy groups above 0.8 MeV with S_4/P_1 approximation$^{11)}$. As is apparent from the comparison, the PALLAS-XYZ calculation somewhat overestimates the experiment at the duct mouth and underestimates it in the vicinity of its exit. On the other hand, the ENSEMBLE calculation agrees relatively well with the experiment at the duct mouth and shows a more rapid decrease within the annular duct than that of both the experiment and the PALLAS-XYZ calculation. The underestimate of the ENSEMBLE calculation has been found to be due to the use of an insufficient number of angular direction$^{11)}$. Representing the cross section of the annular duct by a rectangular model is considered to be another cause for the difference of trends in neutron attenuation within the annular duct between the experiment and the calculations with the PALLAS-XYZ and ENSEMBLE codes.

Another PALLAS-XYZ calculation was carried out with coarser spatial meshes to show that it overestimates the experiment by a larger amount than that of the calculation with finer meshes and that it shows quite a similar tendency towards decrease within the annular duct as that in the fine mesh calculation.

The calculations with fine spatial meshes and with coarse ones required 61 min 11 s and 42 min 54 s on the FACOM M200, respectively, using main memory size of about 3400 kbite.

Since both calculations with the PALLAS-XYZ and the ENSEMBLE are presented as examples of the first examination of their applicability to practical three-dimensional shielding problems, the cause of their errors is not studied in detail in the present study. This will be an important subject for study about the present method, to be carried out in future research.

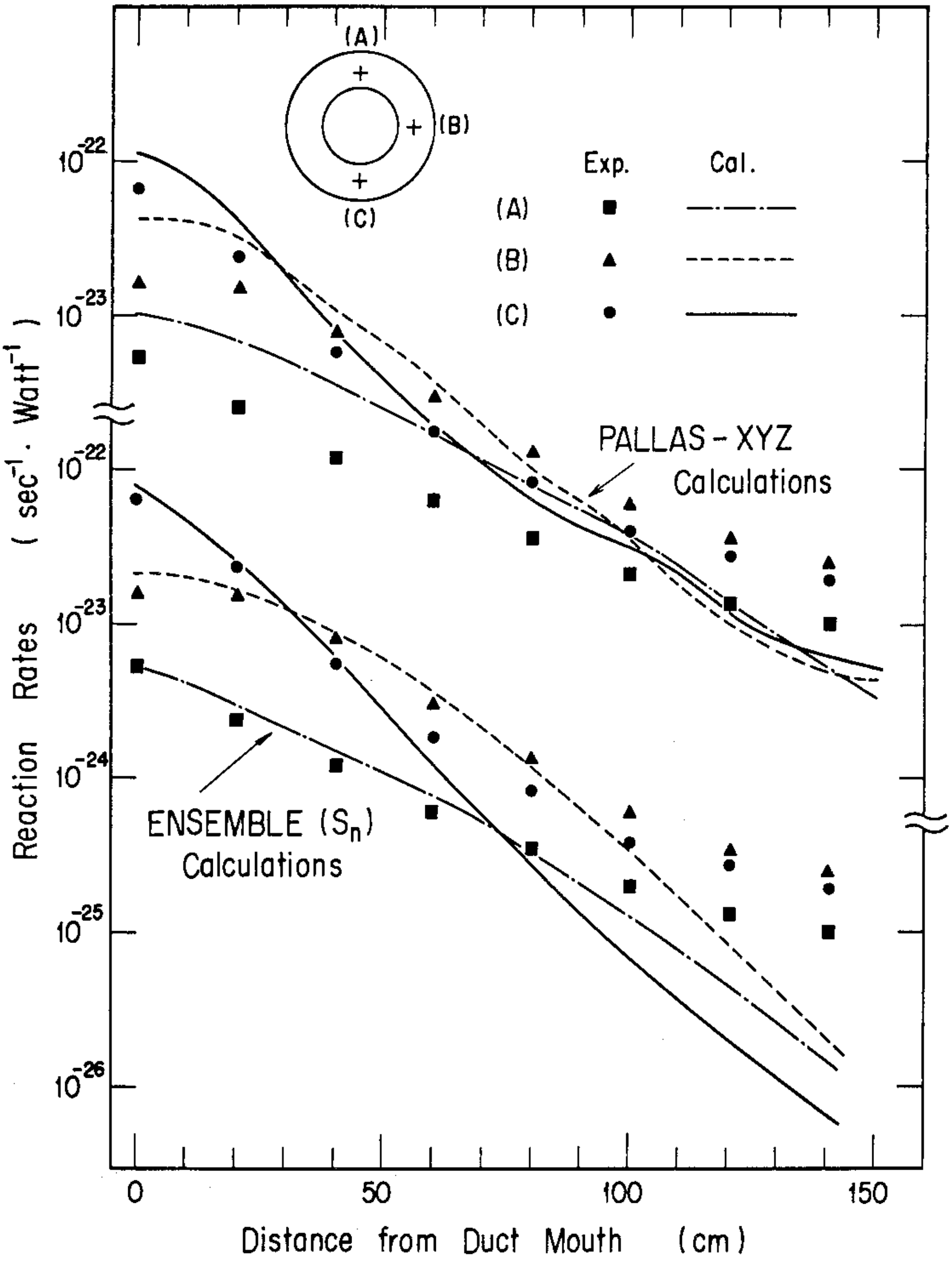

Fig.6.3 Comparison of both PALLAS-XYZ and ENSEMBLE codes calculated with experimental ^{58}Ni(n,p) reaction rates.

7. Analysis of Detailed Neutron Fluxes in PWR Pressure Vessel with Two- and Three-Dimensional PALLAS Transport Codes$^{69)}$

7.1 Introduction

An accurate estimation of detailed neutron fluences in the pressure vessel of light water reactors is indispensable for analyzing the extent of radiation embrittlement. In recent years there has been a growing interest in applying neutron transport calculation to the estimation. At present, however, the neutron transport analysis involves some errors due mainly to the modeling of the actual configuration of power reactors and choice of parameters as well as group constants used in transport calculations.

We presented a paper$^{70)}$ examining the effect of the modeling of a PWR on the prediction of the neutron field at the beltline of its pressure vessel. In this paper, we performed a three-dimensional (X,Y,Z) transport calculation using a PALLAS-XYZ code$^{40)}$ for accurate estimation of the neutron flux leaking from the rectangular PWR core, from which we obtained the boundary angular flux to successively perform a two-dimensional (R,θ) transport calculation using a PALLAS-2DRT for predicting neutron fluxes in the core barrel and pressure vessel. We also analyzed this problem in (R,θ) or (R,Z) geometry.

As a result, we found that the two-dimensional (R,θ) calculation could provide fairly accurate results on neutron flux, as well as on their azimuthal variations at the beltline of the pressure vessel judging from comparison with those of the combined calculation in (X,Y,Z) and (R,θ) geometries. We obtained, however, an unreasonable result in terms of absolute value: The neutron fluxes outside the core calculated in (R,θ) geometry only were underestimated as compared with those calculated in the

$(X,Y,Z) + (R,\theta)$ geometry. Examination of the cause indicated that the source normalization used in the (R,θ) transport calculation was not proper. The source normalization used was determined by dividing the total source neutrons by the total core axial length. Therefore, a more detailed analysis will be presented here, in which the source normalization for the (R,θ) transport calculation is determined using an effective core axial length. Validity for use of an effective core axial length in the (R,θ) model was certified through comparison with the calculations in the $(X,Y,Z) + (R,\theta)$ geometry.

7.2 PWR and Its Calculational Model

7.2.1 Description of PWR

The reactor chosen for consideration is a standard design of the 1000 MWe class PWR71) with a vessel inner radius of 220.28 cm. Figure 7.1 shows the plan configuration of the reactor with a core length of 360 cm. Although the actual core consists of the inner and outer cores with respective enrichments, it is assumed to be homogeneous for simplicity in our calculations. The material compositions are given in Table 7.1. The power distributions are provided in Figs.7.2 and 7.3 in terms of the relative power for the radial and axial distributions, respectively71). The axial distribution shown in Fig.7.3 is assumed to be symmetric about the core midplane in our calculations. Since the reactor power is 3425 MWt, the total source neutrons are obtained as follows:71)

$$3425(\mathrm{MWt}) \times 7.84 \times 10^{10}(\mathrm{n/W{\cdot}sec}) \times 10^{6}(\mathrm{W/MWt}) = 2.685 \times 10^{20}(\mathrm{n/sec}).$$

7.2.2 Three-Dimensional Model for PWR Core

Figure 7.4 depicts the three-dimensional (X,Y,Z) model for the core and its barrel, in which the upper and lower parts illustrate the elevation and plan configurations, respectively. As shown in the elevation model, the core is assumed to be symmetrical about its midplane, at which the reflection boundary condition is set in our calculation because of reduction of computer core storage. In addition, both the upper and lower structures of the core as well as the pressure vessel are omitted in the model due to the same reason. This omission has been found to yield a negligible effect ($< 0.18\%$) on neutron fluxes within the core barrel at its midplane. This was confirmed through check calculations using the (R,Z) model with and without these structures.

On the other hand, a 1/4 plan configuration of the core is taken into account due to the symmetry condition about a core center. The modeling of the barrel is rather rough because of the restricted number of material regions used in the present PALLAS-XYZ code. The solid line denoted as "Boundary" in the figure means that the neutron transport calculation in two-dimensional (R,θ) geometry starts at this boundary, with the angular flux predicted by the three-dimensional (X,Y,Z) calculation.

The radial power distribution in the outermost core region has a great influence upon the neutron flux outside the core, in particular in the PALLAS calculation, since the source distribution is given at each spatial mesh point. In the previous analysis, we had applied the constant distribution within each cell illustrated in Fig.7.2, except for the outermost spatial meshes, at which the source values were assumed to be zeros. This was unnatural, however, and in the present calculation we assume a smoothly varying distribution for the outer core region used in the (X,Y,Z) transport calculation, determined by interpolating smoothly the values within the cells given in Fig.7.2.

7.2.3 Two-Dimensional Model for PWR

Figure 7.5 illustrates the two-dimensional (R,θ) model outside the PWR core at the core midplane. The two-dimensional transport calculation starts at the solid line denoted as "Boundary" defined at 3.57 cm in the coolant inside the barrel. Another (R,θ) model is presented in Fig.7.6, in which the rectangular core is also modeled in (R,θ) geometry. The source distribution is assumed so as to simulate the rectangular core geometry plotted with black points in the outer core region in the figure.

We present the third model approximated in (R,Z) geometry with a radius of 168.3 cm, determined so as to make the core area to the actual one, and with a radius of 183.0 cm, the same as the distance measured from the core center to its corner. Axial power distribution drawn by the solid line in Fig.7.3 is utilized in the calculation.

Table 7.1 Material Atomic Densities
Used in Analyses of PWR
(10^{24} atoms/cm^3)

Zone	Nuclide	Density ($\times10^{24}$)
Core	H O Zr U-238	0.02924 0.02857 0.00562 0.00681
Coolant (Water)	H O	0.04980 0.02490
Baffle Barrel (SS-304)	Cr Fe	0.01690 0.06846
Pressure Vessel	Fe	0.08464
Concrete	H O Si	0.00548 0.04780 0.00950

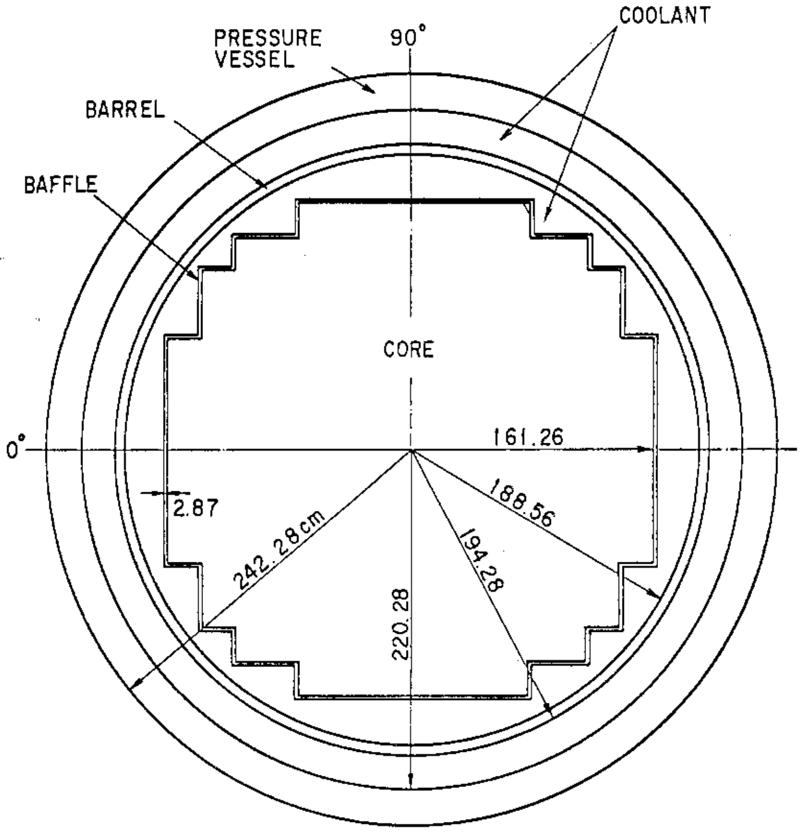

Fig.7.1 Plan configuration of PWR core and pressure vessel.

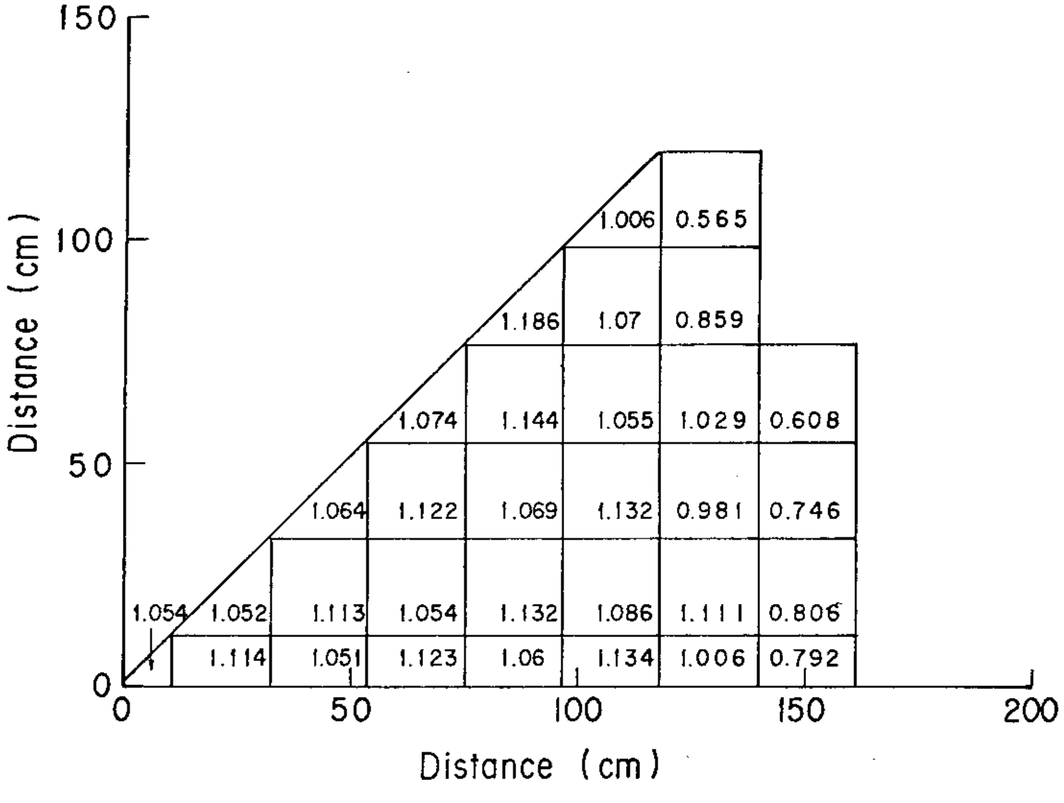

Fig.7.2 PWR fuel assembly relative power distribution.

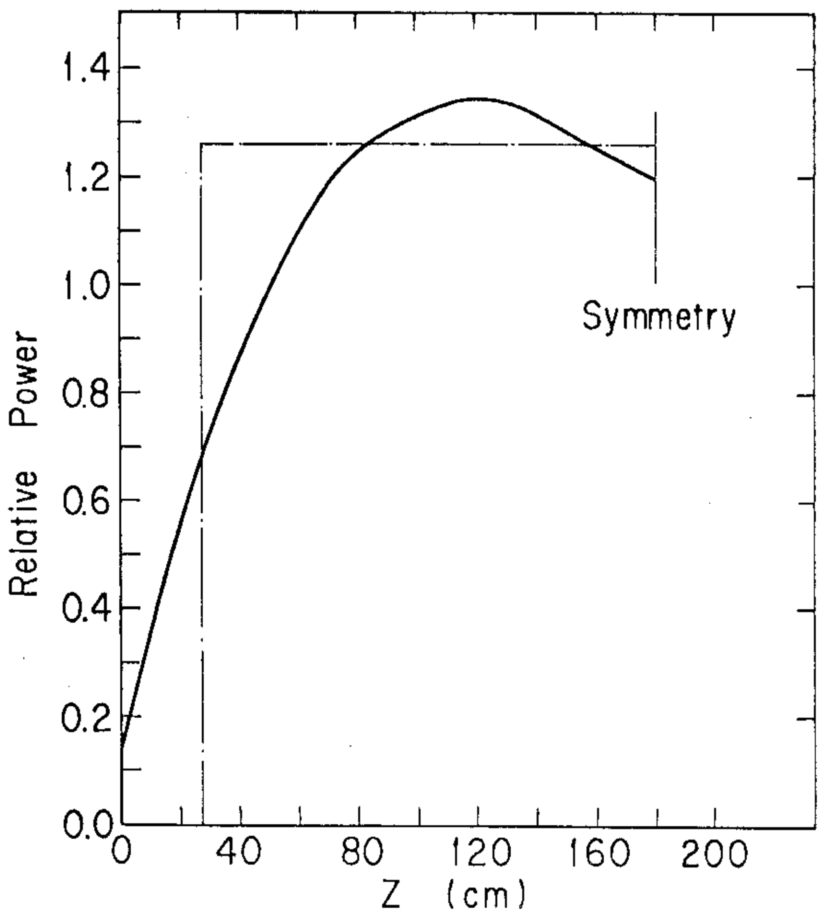

Fig.7.3 PWR axial power distribution.

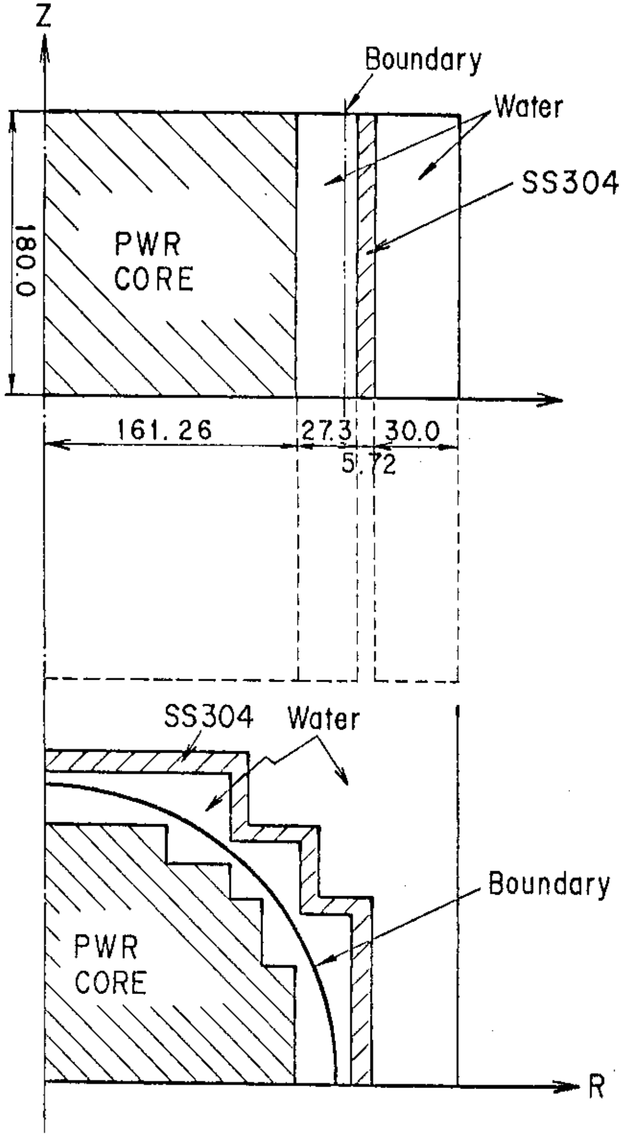

Fig.7.4 (X,Y,Z) calculational model of PWR core and its barrel.

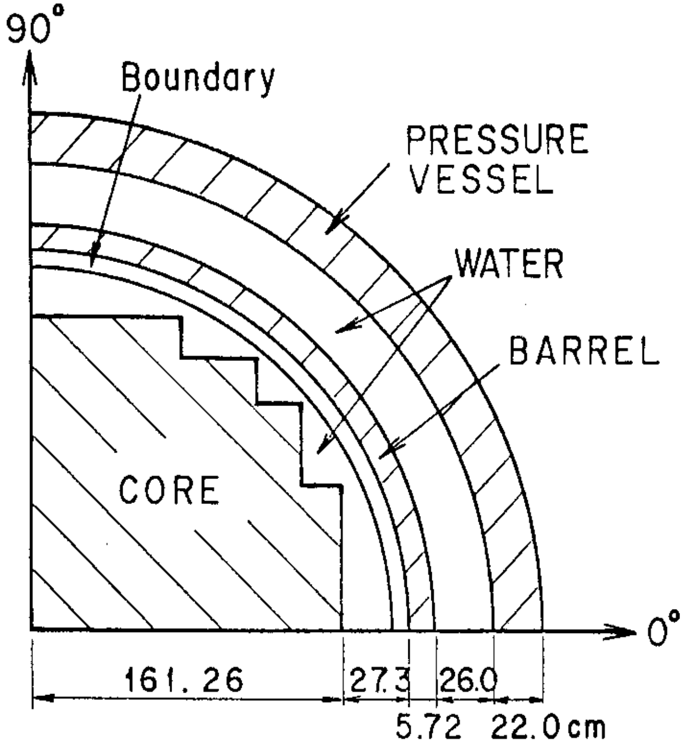

Fig.7.5 Plan configuration of (R,θ) outside the PWR core.

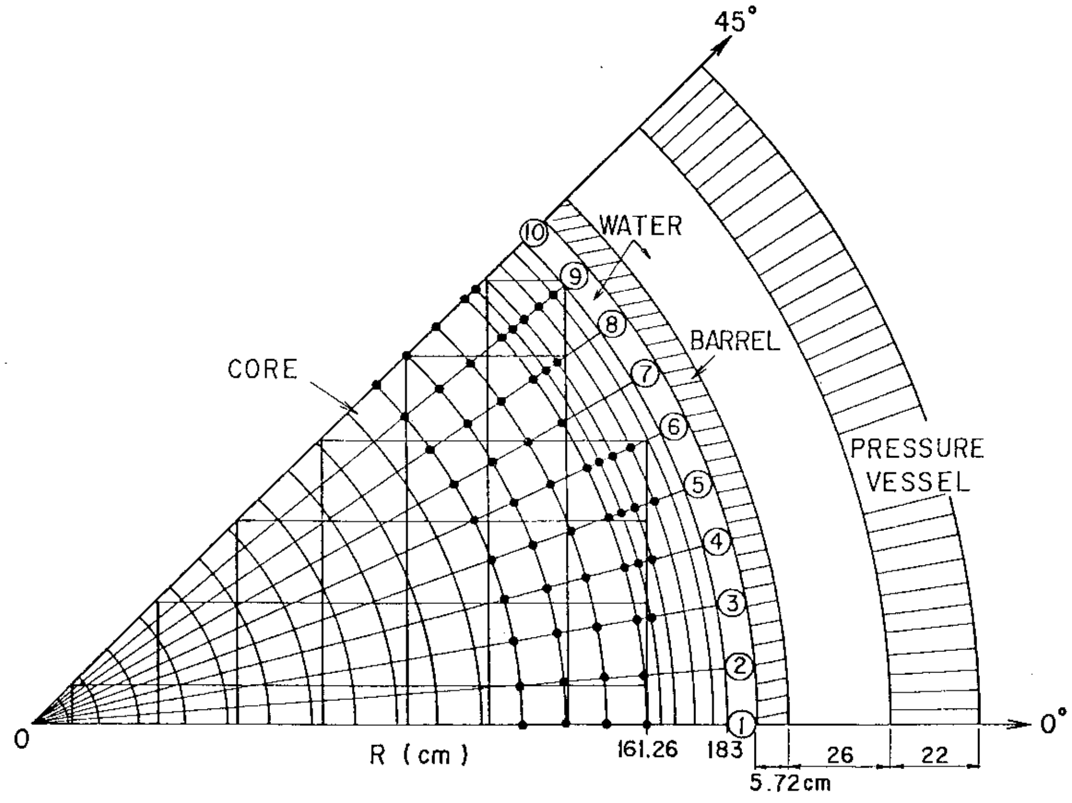

Fig.7.6 Plan configuration of another (R,θ) model of 1/4 core symmetry.

7.3 Neutron Transport Calculation for the PWR

The neutron transport calculations were performed using PALLAS-XYZ, PALLAS-2DRT and PALLAS-2DCY codes for the geometrical models in (X,Y,Z), (R,θ) and (R,Z) geometries, respectively. The nuclear data used were taken from the PALLAS library[58)], which was generated based on the original data from the ENDF/B-IV library. The energy and spatial meshes used in the calculations are given in Table 7.2. In order to take into account the reflected neutrons from shields outside the pressure vessel, we assumed a concrete layer of 20 cm thick outside the pressure vessel for all the calculations, while a reflected boundary condition was set at the left and bottom boundaries.

First, the three-dimensional transport calculation was made for the model shown in Fig.7.4 to determine the angular flux leaking from the core. Second, we obtained, on the basis of the thus evaluated angular flux, the boundary angular flux, with which the (R,θ) transport calculation was performed. The calculated scalar fluxes above 1.0 and 0.1 MeV are plotted with the black and white points as a function of the radial distance in Figs.7.7 and 7.8.

For the transport calculation performed in (R,θ) geometry only, the power normalization is the most important point. In the previous analysis[70)], it was determined based on the core length of 360 cm, which was not reasonable because of the abrupt decrease in relative power distribution toward the core end. We then assume in the present study an effective core length as drawn by the dot-solid line in Fig.7.3. Strictly speaking, this effective length should be determined by normalizing the (R,θ) result to that of the (X,Y,Z) + (R,θ) model. Unless such a standard result is available, the effective core length must be estimated intuitively. The power normalization is determined based on the effective length of 306 cm chosen intuitively, which yields the solution in (R,θ) geometry as shown by dotted lines in Figs.7.7 and 7.8.

For the transport calculation in (R,Z) geometry, the core radius assumed and radial power distribution in the outer core region are very important. In the previous analysis with the (R,Z) model[70)], we took a 168.3 cm radius which makes the modeled core horizontal area coincide with the actual one, resulting in rather small values as compared with the other geometrical calculations seen in Figs.7.7 and 7.8, drawn by the dot-solid lines marked with D. The gap of 20.26 cm (188.56 - 168.3) in the (R,Z) model between the core and its barrel is, however, too large for the average water gap resulting in fast neutron attenuation. In order to simulate the physical phenomenon more accurately, we took a 183.0 cm core radius for the second (R,Z) model. Here, the radial power distribution was assumed by averaging the one used in the (R,θ) model. The calculated results are plotted also in Figs.7.7 and 7.8 with the solid lines marked C.

A fairly good agreement is obtained between the results calculated in (X,Y,Z) + (R,θ) and only (R,θ) models as seen in Figs.7.7 and 7.8. Besides, the azimuthal peaking is conspicuous at 40°. More detailed azimuthal variations are depicted in Fig.7.9 for neutron fluxes above 1.0 and 0.1 MeV. Again, good agreement is seen between the results calculated in (X,Y,Z) + (R,θ) and (R,θ) models. The peaking factor is approximately 2.7, estimated on the basis of 0° fluxes for all the cases. For comparison, the results calculated in the (R,Z) model with 183.0 cm and 168.3 cm radii are drawn with solid and dot-solid lines, respectively. The azimuthal variations for the dpa also show the peaking factor of approximately 2.7.

The PALLAS-XYZ calculations required 4200 kbite main memory size and about 8 hr 20 min CPU time on the FACOM M200 for 41 energy mesh points ranging from 14.2 MeV to thermal neutron energy with 37 × 32 × 13 spatial mesh points and 56 angular quadrature points.

Finally, we provide in Fig.7.10 the calculated energy spectra in terms of lethargy units at three positions —— inner surface of the core barrel, inner surface of and 1/2 depth in the pressure vessel —— at 0° and 40° azimuthal directions.

Table 7.2 Energy and Spatial Meshes Used in PALLAS Calculations

Geometry	Energy range	Lethargy interval	Number of meshes
(R, θ) and (R, Z)	14.2-0.71 MeV 0.71 MeV-10.7 keV 10.6 keV-194 eV 194 eV-Thermal	0.1 0.2 0.4 0.8	31 21 10 8
	Total		70
(X, Y, Z)	14.2-1.29 MeV 1.29-0.11 MeV 0.11 MeV-Thermal	0.2 0.4 0.8	13 6 16
	Total		35

Geometry	Zone	Interval	Meshes
(R, θ) and (R, Z)	Inner core Outer core Baffle Coolant Barrel Pressure Vessel Concrete	10.8 cm 4.3 cm 2.87 cm 1.86∿3.25 cm 2.86 cm 2.75 cm 6.6 cm	15 6 2 13 3 9 4
(X, Y, Z)	Core Coolant Barrel	5.0∿8.0 cm 5.46 cm 5.72 cm	29 6 2

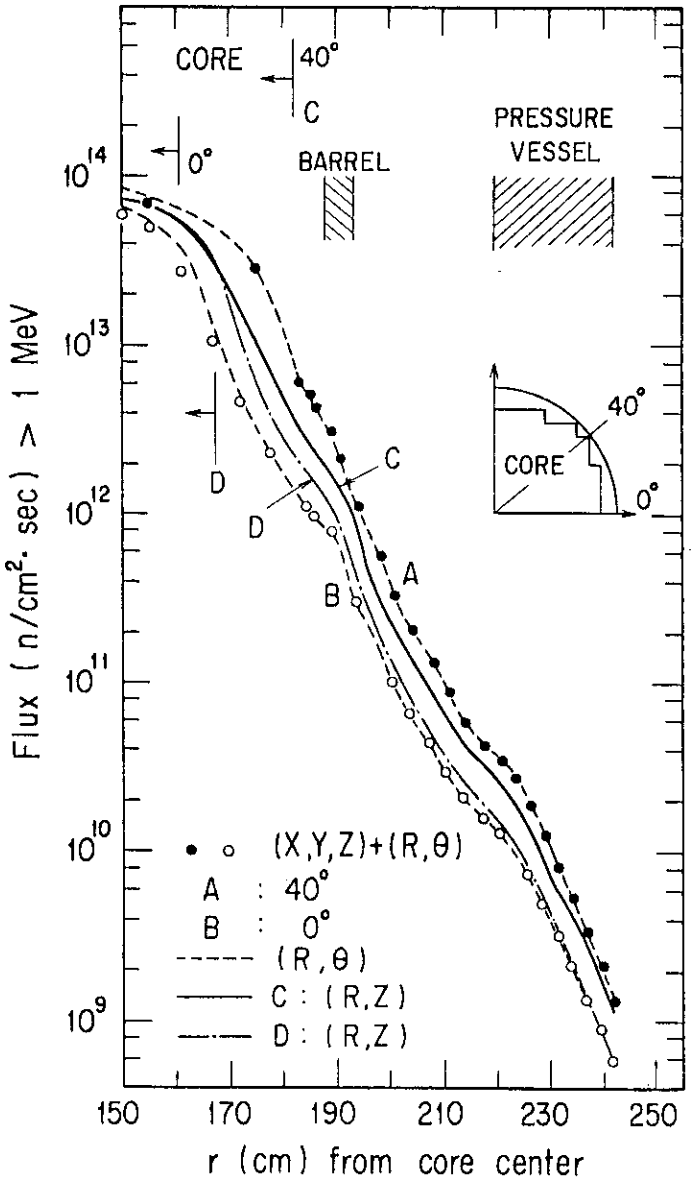

Fig.7.7 Neutron flux distributions (>1 MeV) as a function of distance measured from the core center at the core midplane.

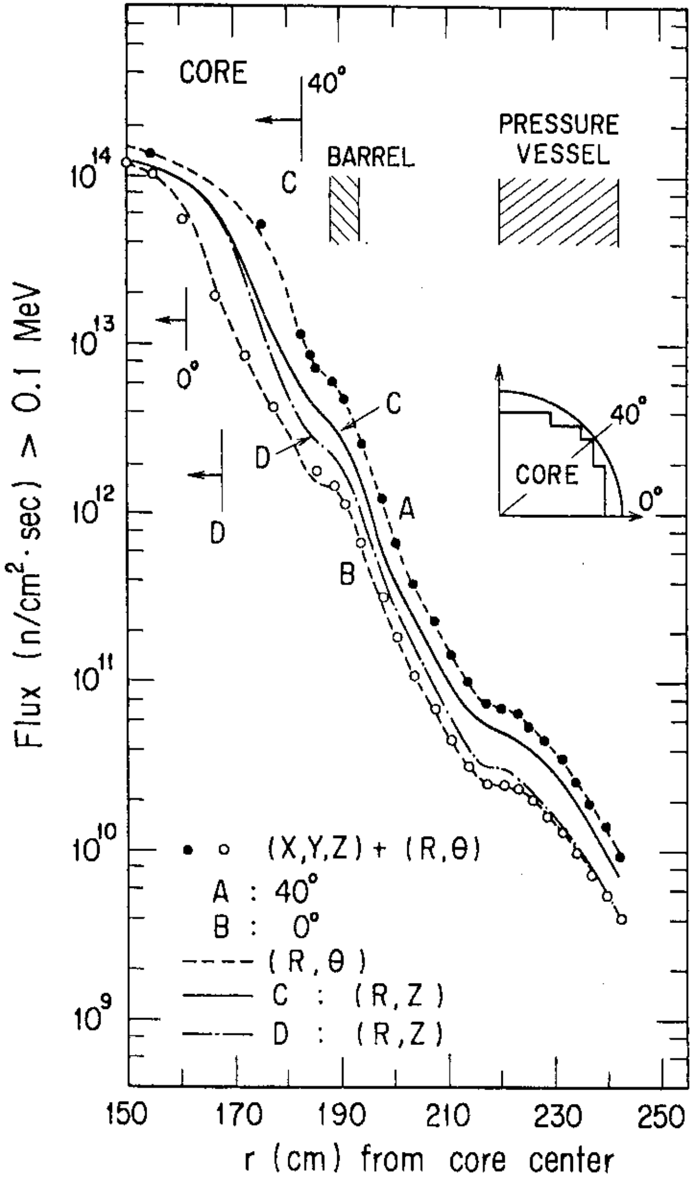

Fig.7.8 Neutron flux distributions (>0.1 MeV) as a function of distance measured from the core center at the core midplane.

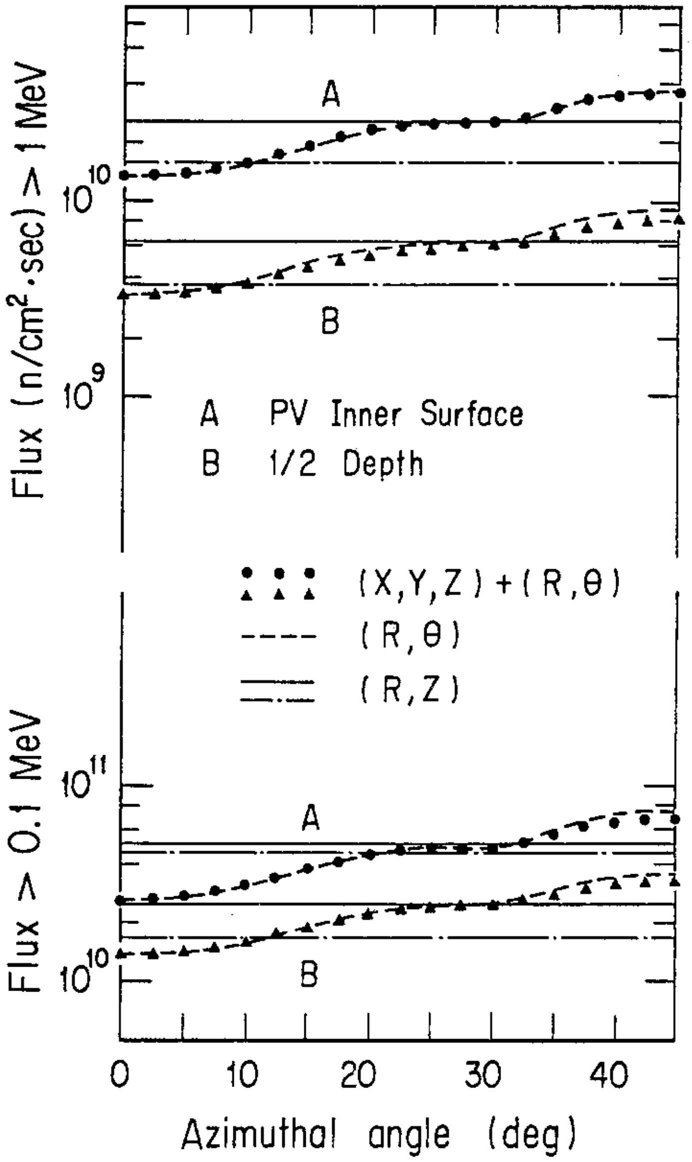

Fig.7.9 Azimuthal variations of neutron flux above 1.0 MeV and 0.1 MeV.

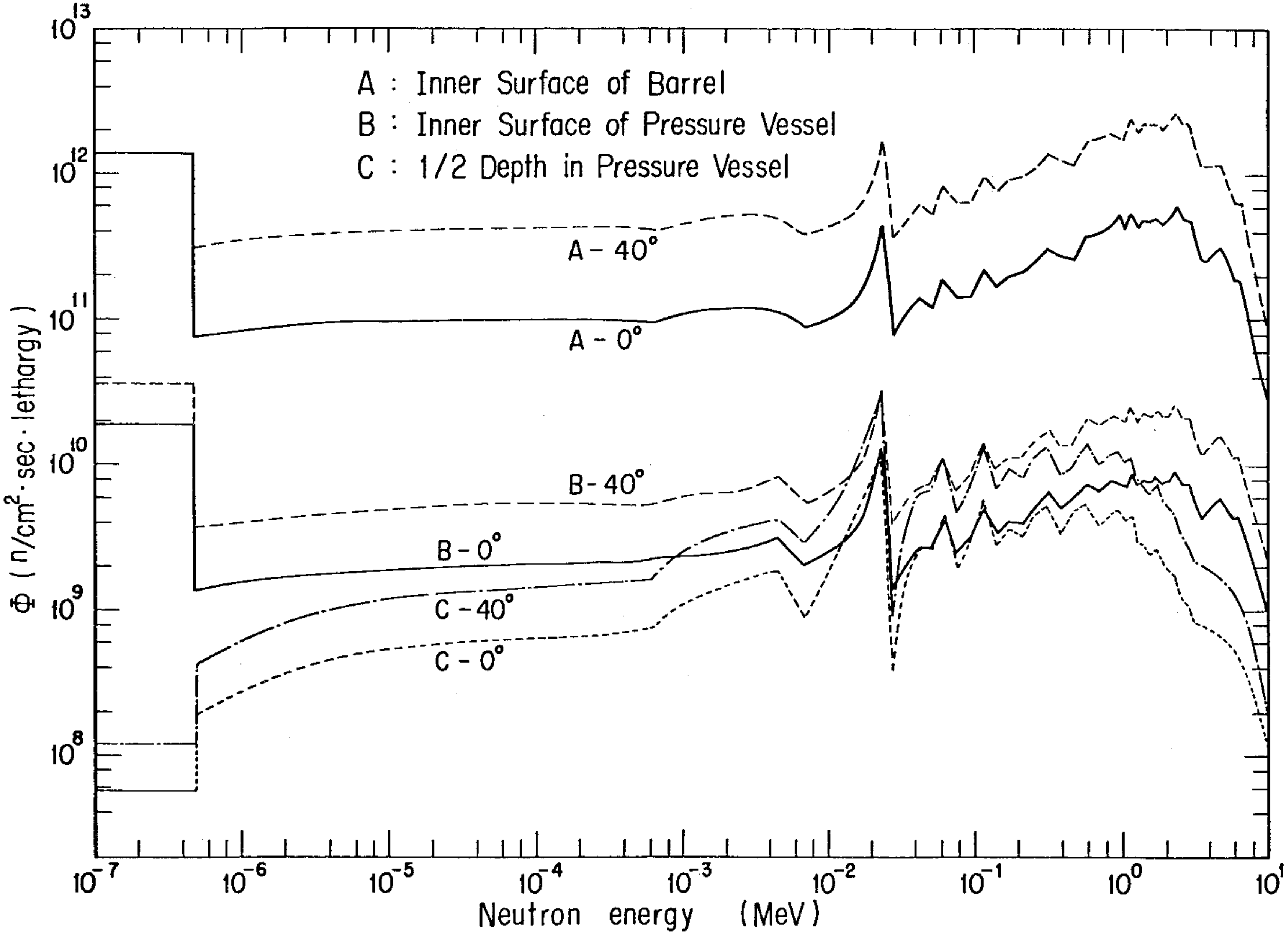

Fig.7.10 Energy spectra in units of neutron lethargy at the inner surface of the core barrel, inner surface of and 1/2 depth in the pressure vessel at 0° and 40°.

7.4 Discussion and Conclusion

For the purpose of finding a reliable calculation method for determining detailed neutron fluences in a pressure vessel, we have performed neutron transport calculations for various models of a 1000 MWe class PWR in three different geometries: (X,Y,Z) + (R,θ), (R,θ) and (R,Z) geometries.

We have assumed an effective core length to provide a proper source normalization in the (R,θ) calculation. This was intuitively determined as shown in Fig.7.3, to be 85% of the actual core length. Comparisons between the (R,θ) calculation and the (X,Y,Z) + (R,θ) calculation provide fairly good agreement, as seen in Figs.7.7 through 7.9, for both radial attenuation and azimuthal variation of the integral fluxes above 1.0 and 0.1 MeV. This fact indicates that the use of the effective core length may be reasonable for the source normalization in a (R,θ) model.

The PALLAS calculations indicate that the azimuthal peaking is a factor of approximately 2.7 at 40° compared with the results at 0° in both neutron fluxes and dpa for this type of PWR. The peaking values at the PV inner surface are 3.8×10^{10} and 7.4×10^{10} n/sec, for neutron fluxes above 1.0 and 0.1 MeV and 5.4×10^{-11} dpa/sec, respectively.

Finally, it may be concluded that the transport calculation in (X,Y,Z) geometry is a standard tool for evaluating the angular flux leaking from the (X,Y,Z) geometrical core, from which the neutron fluxes are determined in terms of absolute value at various positions outside the core. In addition, the comparison of the (R,θ) calculation with the standard calculation performed in combining (X,Y,Z) + (R,θ) geometries indicates that the (R,θ) calculation can yield fairly good results of neutron fluxes above 1.0 and 0.1 MeV and also for dps, if the proper source normalization is obtained by using the effective core length.

8. Summary and Conclusions

The main purposes of the present study have been 1) to establish a numerical method for solving the neutron integral transport equation in three-dimensional (x,y,z) geometry on the basis of the direct integration method, 2) to verify its validity by analyzing two benchmark problems based on shielding experiments and 3) to apply this method to a shielding calculation of 1000 MWe class PWR power plant.

The main results presented in each Chapter can be summarized as follows.

Chapter 1 was devoted to a brief presentation of the fundamental theory of the direct integration method for solving the integral transport equation in general geometry. The characteristic features are summarized as an exact treatment of anisotropic scattering, of applying the differential scattering cross section itself to scattering calculation; analytical integration of the flux term and also direct integration of the source term over the spatial variable in the radiation moving direction; absence of iterative calculation for obtaining the group angular flux, instead, application of the point-energy calculation.

In Chapter 2, the final expression of the solution was derived for solving the neutron integral transport equation in three-dimensional (x,y,z) geometry by direct integration over the spatial variable in the direction of radiation flight at each discrete ordinates mesh. Then, Lagrange's interpolation formula with bilinear or biquadratic form was introduced to the present method for accurate estimation of two-dimensional variation of both flux and source term.

The exponential method was then implemented to the present method. This approximates the source distribution by a combination of linear and exponential functions for evaluation of source term through integration over the spatial variable between any mesh intervals. For verifying the validity of the new technique, an extensive numerical evaluation of neutron and gamma-ray transport problems was made with the one-dimensional transport code PALLAS-PL, SP to compare them with the PALLAS calculations based on the linear function approximation and with the S_n code ANISN calculations. As a result, it was found that the use of this method yields a remarkable improvement in calculations with small numerical errors, irrespective of the spatial mesh size.

In addition, the peak shape estimation technique was introduced for estimation of the neutron energy spectrum between coarse energy mesh intervals in each subdivided material region. With this technique, region-wise weight functions for three-dimensional scattering calculations are obtained from a one-dimensional PALLAS calculation with 0.1 lethargy width energy structure. Validity of the technique was verified by analyzing the neutron deep penetration problem through iron. As a result, a significant improvement in the accuracy of the three-dimensional calculation based on coarse energy meshes was obtained with a negligibly small increase in CPU time for the addition of one-dimensional transport calculation.

In addition to the introduction of the exponential method (useful for reduction of the spatial mesh numbers required), introduction of the peak shape estimation technique (useful for saving energy meshes) greatly contributes to the establishment of a practical calculational method of neutron transport in three-dimensional geometry.

Next, theoretical error analysis of the direct integration was made for the first time on the basis of the method proposed by Lee and Vaidyanathan. Since the present method does not adopt the iterative-convergence scheme and the flux term is evaluated analytically, evaluation of the error was performed through spatial approximation of the source distribution. The evaluation revealed that the leading error of the order of Δ^3 ($\Delta \equiv$ spatial mesh interval) arose under the restraint of the source conservation at each spatial mesh point for both linear and exponential functional approximations of the source spatial distribution. Hence, the quadratic functional approximation was found to improve the mathematical error of the order of Δ^3 to Δ^4.

In Chapter 3, the PALLAS-XYZ, a neutron transport code was developed based on the direct integration method for solving the integral transport equation with general anisotropic scattering in three-dimensional (x,y,z) geometry. Several new techniques were added to the original method for establishing a reliable three-dimensional neutron transport code, applicable to practical shielding problems. PALLAS-XYZ, constructed under overlay structure, is divided mainly into two parts: a three-dimensional calculation routine and a one-dimensional one for spectral shape estimation technique.

Further, a reaction rate calculation code was devised as an auxiliary code to PALLAS-XYZ. With this code, reaction rate at each spatial mesh point can be obtained through integration over energy of the interpolated scalar flux multiplied by the response function in 620 group SAND-II form, where interpolation of the PALLAS-XYZ calculated scalar flux is performed with third order natural spline function. This method will solve the problem of poor reproducibility in reaction rate calculation.

Chapter 4 was devoted to preparation of the PALLAS library: the multigroup neutron cross section library for the PALLAS. The original version was generated in 1977 with the RADHEAT-V3 system based on the basic data from ENDF/B-IV. In 1981, however, an overall revision of the original version was made using the NJOY-PALLAS code system, newly prepared on the basis of the nuclear data processing system NJOY. The revised version of the library includes 27 nuclides and 4 mixtures (2 stainless steels and 2 concretes) for 5 equi-lethargy energy group structures of 0.05, 0.1, 0.2, 0.4 and 0.8 lethargies. The nuclear group constants considered are 1) microscopic smoothed cross sections (σ_t,σ_c,σ_s), 2) Legendre expansion coefficient for differential cross section of elastic scattering, 3) scattering matrix due to inelastic scattering and (n,2n') reactions and 4) secondary photon production matrix. Use of group constants on fixed group structure provides an advantage to certify reproducibility of the data, which is very important for shielding design calculation.

In Chapter 5, the PCA benchmark problem based on the experiment was calculated with PALLAS-XYZ using 48 angular meshes in a coupled 0.2 + 0.4 equi-lethargy energy structure. The fast neutron reaction rates, integral fluxes greater than 0.1 MeV and greater than 1.0 MeV, and displacement per atom (dpa) calculated with PALLAS-XYZ were compared with many two-dimensional S_n calculations and a Monte Carlo one, as well as with the experiment. As a result, the PALLAS-XYZ calculations were seen to agree with the experiment in reaction rates with a maximum deviation of 30%, and to agree well with the experiment in the integral fluxes and dpa, within the range of experimental error. Besides, from the comparison with other transport calculations, the PALLAS-XYZ calculation without any leakage correction was found to be as accurate as, or even more accurate than the Monte Carlo calculation and the two-dimensional S_n calculations with help of leakage correction.

In Chapter 6, the problem of neutron streaming through an annular void duct was calculated with the PALLAS-XYZ using 56 angular meshes in a coupled 0.2 + 0.4 equi-lethargy energy structure. Comparisons were made of the PALLAS-XYZ calculated reaction rate distribution of ^{58}Ni(n,p) threshold reaction along the annular duct with the experiment and with the ENSEMBLE calculation by an approximation of S_4/P_1. As a result, the PALLAS-XYZ calculation was found to somewhat overestimate the experiment at the duct mouth and underestimate in the vicinity of its exit, whereas the ENSEMBLE calculation shows a more rapid decrease within the annular duct than the PALLAS-XYZ one. Since both calculations with PALLAS-XYZ and ENSEMBLE are presented as an example of the first examination of their applicability to practical three-dimensional shielding problems, the cause of their error is not investigated in detail in the present study.

Chapter 7 is devoted to neutron transport calculations for various models of a 1000 MWe class PWR with PALLAS codes in combined $(X,Y,Z) + (R,\theta)$, (R,θ) and (R,Z) geometries, to obtain both radial attenuation and azimuthal variation for the integral fluxes above 1.0 and 0.1 MeV, and dpa. We obtained an azimuthal peaking factor of approximately 2.7 at 40° compared with the results at 0° in both integral fluxes above 1.0 and 0.1 MeV, and dpa at the inner surface of the pressure vessel. The peaking values obtained are respectively 3.8×10^{10} and 7.4×10^{10} $(n/cm^2 \cdot sec)$ for integral fluxes above 1.0 and 0.1 MeV, and 5.4×10^{-11} (dpa/sec). It is concluded that the transport calculation in (X,Y,Z) geometry is a standard tool for evaluating the angular flux leaking from the (X,Y,Z) geometrical core, from which the neutron fluxes are determined in terms of absolute value at various positions outside the core. Further, the $(X,Y,Z) + (R,\theta)$ calculation can provide accurate source normalization in a (R,θ) model.

The present method includes some weak points, one of which is the problem that, as pointed out in Ref.34 and 35, neutron ballance at each spatial mesh point is not certified in PALLAS calculations. As one of the possible solutions to this problem, a new numerical method is under investigation based on the idea that without using a bilinear or biquadratic interpolation technique, estimation of flux and source terms at the mesh point provious to the mesh $\bar{r}_i$ of interest, can be performed according to the projection area of each angular segment on rectangular spatial cell surfaces.

In addition, in order to establish a practical shielding calculation method, the PALLAS-XYZ code requires introduction of further numerical techniques already implemented successfully in the one-, and two-dimensional PALLAS codes, such as the analytical unscattered flux calculation method, the bootstrap method, the gamma-ray transport calculation routine, the mono-energetic radiation transport calculation routine, and others.

ACKNOWLEDGMENTS

There are several persons I would like to acknowledge and thank. First and foremost, I acknowledge my deep gratitude to Dr. Kiyoshi Takeuchi for the helpful discussions I benefited from during the course of the work presented here.

I would also like to express my appreciation to Dr. Tomoo Suzuki for his continuing concern and encouragement. I am indebted to Professor Tomonori Hyodo, Professor Keisuke Kobayashi and Mr. Kazuo Shin of Kyoto University for their valuable comments and discussions.

Finally, I am pleased to acknowledge Mrs. Sally Yanai for her careful correction of the English sentences in this thesis.

REFERENCES

1) Irving D.C., Freestone R.M., Jr., and Kam F.B.K.: "05R, A General-Purpose Monte Carlo Neutron Transport Code", ORNL-3622 (1965).

2) Straker E.A., Stevenes P.N., Irving D.C., and Cain V.R.: "MORSE Code: A Multigroup Neutron and Gamma-Ray Monte Carlo Transport Code", ORNL-4585 (1970).

3) Iida M.: "Application of Monte Carlo Transport Code to Neutronics Design of Tokamak Fusion Reactor", JAERI-M 9717 (1981) (in Japanese).

4) Ueki K.: Nucl. Sci. Eng., 79, 253, (1981).

5) Carlson B.G.: "Solution of the Transport Equation by the S_n Method", LA-1891 (1955).

6) Engle W.W., Jr.: "A User's Manual for ANISN, A One-dimensional Discrete Ordinates Transport Code with Anisotropic Scattering", K-1693 (1967).

7) Mynatt F.R., Muckenthaler F.J. and Stevens P.N.: "Development of Two-Dimensional Discrete Ordinates Transport Theory for Radiation for Shielding", CTC-INF-952 (AD-692168) (1969), and Rhoades W.A. and Mynatt F.R.: "The DOT-III Two-Dimensional Discrete Ordinates Transport Code", ORNL-TM-4280 (1973).

8) Lathrop K.D., et al.: "TWOTRAN-II: An Interfaced, Exportable Version of the TWOTRAN Code for Two-Dimensional Transport", LA-4848-MS (1973).

9) Takeuchi K. and Sasamoto N., Editors: "Two-Dimensional Shielding Benchmark Calculations by Discrete Ordinates and Monte Carlo Codes - No.1", JAERI-M 7799 (1978) (in Japanese).

10) Emmett M.B., Burgart C.E., and Hoffman T.J.: "A General Purpose Code for Coupling Discrete Ordinates and Monte Carlo Radiation

Transport Calculations", ORNL-4853 (1973).

11) Nishimura T., Tada K., Yokobori H., and Sugawara A.: J. Nucl. Sci. Technol., 17, 539 (1980).

12) Lathrop K.D.: "THREETRAN, A Program to Solve the Multigroup Discrete Ordinates Transport Equation in (x,y,z) Geometry", LA-6333-MS (1976).

13) Miller Jr., W.F., and Reed W.H.: Nucl. Sci. Eng., 62, 391 (1977).

14) Lathrop K.D.: Comput. Phys., 4, 475 (1969).

15) Takeuchi K.: J. Nucl. Sci. Technol., 8, 141 (1971).

16) Takeuchi K.: "User's Manual for the SELENE Code", Report of Ship Research Institute, 4, 3, 43 (1967).

17) Kataoka I. and Takeuchi K.: "Discrete Ordinates Numerical Integration Method for Bulk Shielding Calculation", Proc. Third Int. Conf. Reactor Shielding, Harwell, September 26-29, 1967, U.K. Atomic Energy Authority (1967).

18) Takeuchi K.: J. Nucl. Sci. Technol., 5, 342 (1968).

19) Takeuchi K.: J. Nucl. Sci. Technol., 6, 466 (1969).

20) Takeuchi K.: "PALLAS-PL, SP, A One-Dimensional Transport Code", Papers of Ship Research Institute No.42 (1973).

21) Takeuchi K.: "PALLAS-2DCY, A Two-Dimensional Transport Code", papers of Ship Research Institute, No.47 (1973).

22) Takeuchi K.: "Study on a Numerical Approach to the Boltzmann Transport Equation for the Purpose of Analyzing Neutron Shields", report of Ship Research Institute, 9, 6 (1972) (in Japanese).

23) Takeuchi K. and Yamaji A.: J. Nucl. Sci. Technol., 11, 49 (1974).

24) Miura T., Yamaji A., and Takeuchi K.: J. Nucl. Sci. Technol., 14, 878 (1977).

25) Takeuchi K. and Yamaji A.: "Discrete Ordinates Numerical Integration Method for Neutron Transport Equation in One- and Two-Dimensional

Geometries", Proc. Fourth Int. Conf. Reactor Shielding, Paris, October 9-13, 1972, CONF-721018, International Atomic Energy Agency (1972).

26) Miura T., Takeuchi K. and Yamano N.: J. Nucl. Sci. Technol., 16, 563 (1979).

27) Ando Y., Miyasaka S. and Takeuchi K.: "Radiation Leakage of Nuclear Ship MUTSU", J. Atomic Energy Soc. Japan, 17, 57 (1975) (in Japanese).

28) Miura T., Takeuchi K., and Fuse T.: "Measurement and Calculation of Radiation Streaming Through Annular Ducts", report of Ship Research Institute, 16, 6, 17 (1979) (in Janapese).

29) Sasamoto N. and Takeuchi K.: Nucl. Sci. Eng., 71, 330 (1979).

30) Sasamoto N. and Takeuchi K.: Nucl. Technol., 47, 189 (1980).

31) Kanai Y. and Takeuchi K.: To be submitted to J. Nucl. Sci. Technol.

32) Takeuchi K.: "PALLAS-2DCY-FC, A Calculation Method and Radiation Transport Code in Two-Dimensional (r,z) Geometry", papers of Ship Research Institute, No.57 (1979).

33) Takeuchi K. and Sasamoto N.: Nucl. Sci. Eng., 80, 536 (1982).

34) Alcouffe R.E. and Larsen E.W.: "A Review of Characteristic Methods Used to Solve the Linear Transport Equation", Proc. Int. Topl. Mtg. Advances in Mathematical Methods for the Solution of Nuclear Engineering Problems, Munich, Germany, April 27-29, 1981, Vol.1, p.3, Kernforschungszentrum Karlsruhe (1981).

35) Sanchez R. and McCormick N.J.: Nucl. Sci. Eng., 80, 481 (1982).

36) Wagner M.R., Sargis D.A. and Cohen S.C.: Nucl. Sci. Eng., 41, 14 (1970).

37) Askew J.R.: "A Characteristic Formulation of the Neutron Transport Equation in Complicated Geometries", AEEW-M 1108, U.K. Atomic Energy Authority, Winfrith (1972).

38) Filippone W.L., Woolf S. and Lavigne R.J.: Nucl. Sci. Eng., 77, 119 (1981).

39) Larsen E.W. and Alcouffe R.E.: "The Linear Characteristic Method for Spatially Discretizing the Discrete Ordinates Equations in (X,Y)-Geometry", Proc. Int. Topl. Mtg. Advances in Mathematical Methods for the Solution of Nuclear Engineering Problems, Munich, Germany, April 27-29, 1981, Vol.1, p.99, Kernforshungszentrum Karlsruhe (1981).

40) Sasamoto N. and Takeuchi K.: Nucl. Sci. Eng., 80, 554 (1982).

41) Lee S.M. and Vaidyanathan R.: Nucl. Sci. Eng., 76, 1 (1980).

42) Fujimura T., Japan Atomic Energy Research Institute, Private Communication.

43) McElroy W.N., et al.: "Development and Testing of Standardized Procedures and Reference Data for LWR Surveillance", Proc. IAEA Specialists' Mtg., Vienna, February 26 - March 1, 1979, HEDL-SA-1719, International Atomic Energy Authority (1979).

44) McElroy W.N., et al.: "LWR Pressure Vessel Surveillance Dosimetry Improvement Program: PCA Experiments and Blind Test", NUREG/CR-1861 (HEDL-TME 80-87, R5), Hanford Engineering Development Laboratory (1981).

45) Bendall D.E. and Brissended R.H.: "McBEND Programme User's Guide", CRSD/147, AERE Winfrith, UK (1980).

46) Gritzner M.L., Simmons G.L., Albert T.E., and Straker E.A.: "PWR and BWR Radiation Environments for Radiation Damage Studies", EPRI NP-152 (Research Project 304-1), Science Applications (1977).

47) Read W.H.: Nucl. Sci. Eng., 48, 309 (1971).

48) Madsen N.K.: Nucl. Sci. Eng., 54, 376 (1974).

49) Rhoades W.A. and Engle Jr., W.W.: Trans. Am. Nucl. Soc., 27, 776 (1977).

50) Barbucci P. and Di Pasquantonio F.: Nucl. Sci. Eng., 63, 179 (1977).

51) Takeuchi K. and Sasamoto N.: "A Code for Direct Integration of Transport Equation in Two-Dimensional (R,Z) geometry", JAERI-M 9014 (1980).

52) Watt B.E.: Phys. Rev., 87, 1037 (1952).

53) Koyama K., et al.: "RADHEAT-V3, A Code System for Generating Coupled Neutron and Gamma-Ray Group Constants and Analyzing Radiation Transport", JAERI-M 7155 (1977).

54) Schaeffer N.M., Editor: "Reactor Shielding for Nuclear Engineers", p.49, U.S. ATOMIC ENERGY COMMISSION Office of Information Service (1973).

55) Carter M.D. and Packwood A.: "The Winfrith Benchmark Experiments in Iron", NEACRP-U-73, Nuclear Energy Agency, Committee on Reactor Physics (1976).

56) Nakagawa M. and Katsuragi M., Japan Atomic Energy Research Institute, Private Communication.

57) Tanaka S., Sasamoto N., et al.: "Shielding Benchmark Problems", JAERI-M 7843 (1978) (in Japanese).

58) Sasamoto N., Tanaka S., and Takeuchi K.: "Multi-Group Neutron Cross Section Libraries for Code PALLAS", JAERI-M 7445 (1977) (in Japanese).

59) Sasamoto N. and Takeuchi K.: "Revision of Multi-Group Neutron Cross Section Libraries for PALLAS", JAERI-M 9527 (1981) (in Japanese).

60) Simons R.L. and McElroy W.N.: "Evaluated Reference Cross Section Library", BNWL-1312 (1970).

61) Cullen D.E., Kocherov N. and McLaughlin P.M.: "The International Reactor Dosimetry File (IRDF-82)", IAEA-NDS-41/R, IAEA Nuclear Data Section (1982).

62) Greville T.N.E.: Math. Comp. 24, 179 (1979).

63) Takeuchi K. and Tanaka S.: J. Nucl. Sci. Technol., 18, 581 (1981).

64) MacFarlene R.F., et al.: "The NJOY Nuclear Data Processing System: User's Manual", LA-7584-M (1978).

65) Ford III. W.E.: "The POPOP4 Library of Neutron Induced Secondary Gamma-Ray Yield and Cross Section Data", CTC-42, RSIC Data Library Collection Designation DLC-12, (1970).

66) Koyama K., et al.: "Multi-Group Cross Section Sets for Shield Materials —— 100 Neutron Groups and 20 Gamma-Ray Groups in P_5 Approximation —— ", JAERI-M 6928 (1977) (in Japanese).

67) Maerker R.E. and Wagschal J.J.: "ORNL PCA Calculations for the 8/7 and 12/13 Configurations", Presented in the PCA Blind Test Workshop, May 22-23 (1980).

68) "Standard Practice for Characterizing Neutron Exposures in Ferritic Steels in Terms of Displacements per Atom (dpa)", 1979 Annual Book of ASTM Standards, ASTM E693-79, Part 45 (1979).

69) Takeuchi K. and Sasamoto N.: to be submitted to Nuclear Technology.

70) Takeuchi K. and Sasamoto N.: "Three-Dimensional Discrete-Ordinates Calculation for Accurate Determination of Neutron Fluence in Reactor Pressure Vessel", Fourth ASTM-EURATOM Symposium on Reactor Dosimetry, A.1-4, March 22-26 (1982) NBS, Washington D.C.

71) Gritner M.M., et al.: "PWR and BWR Radiation Environments for Radiation Damage Studies", EPRI NP-152 (1977).